Polymer Nanoparticle Characterization and Applications for Drug Delivery

Rose Angela Roberts

Dissertation submitted to the faculty of the Virginia Polytechnic Institute and State University in partial fulfillment of the requirements for the degree of

Doctor of Philosophy
In
Materials Science and Engineering

E. Johan Foster
Abby R. Whittington
Robert G. Gourdie
Kevin J. Edgar

December 10, 2018
Blacksburg, VA

Keywords: poly(lactic-co-glycolic acid), cellulose nanocrystals, drug delivery

Polymer Nanoparticle Characterization and Applications for Drug Delivery

Rose Angela Roberts

ABSTRACT

Nanoparticle usage continues to increase in everyday products, from cosmetics to food preservation coatings, drug delivery to polymer fillers. Their characterization and synthesis is of utmost importance to ensure safety and improved product quality. Nanoparticles can be sourced naturally or synthetically fabricated. Cellulose nanocrystals (CNCs) are rod-like nanoparticles that can be isolated from nature. Reliable methods of characterization are necessary to ensure quality control. However, their physical characteristics cause challenges for imaging under transmission electron microscopy (TEM) with a high enough resolution for dimensional analysis. Heavy metal staining such as radioactive uranyl acetate is often used to increase contrast and TEM sample substrate preparation techniques often use expensive equipment such as glow discharge in order to prevent CNC agglomeration. A method to reliably produce TEM images of CNCs without using radioactive stains or expensive glow discharge equipment was developed, using a vanadium-based stain branded NanoVan® and bovine serum albumin to keep CNCs dispersed while drying on the TEM substrate. Due to their aspect ratio, there is also concern of toxicity to the lungs. The concentration of CNCs in air in production facilities must be monitored, but there is currently no method tailored to CNCs. A method using UV-vis spectroscopy, dynamic light scattering, TEM, and scanning mobility particle sizer in conjunction with impinger collectors was developed for monitoring aerosolized CNC concentration. Synthetic nanoparticles are often used for controlled drug delivery systems. A new peptide drug termed αCT1 has been shown to interact with cell communication in a way that promotes wound healing, reduces inflammation and scarring, and aids in cancer

therapy. However, the peptide's half-life in the body is estimated to be less than a day, which is not conducive to long-term treatments. Controlling its release into the body over several weeks can decrease the number of doses required, which is especially useful for glioblastoma treatment. Poly(lactic-co-glycolic acid) (PLGA) is often used for drug encapsulation since it hydrolyzes in the body and is biocompatible. Two methods of αCT1 encapsulation in PLGA were explored. It was found that flash nanoprecipitation increased loading of αCT1 in the particles by 1-2 orders of magnitude compared with the double emulsion method. Particles released αCT1 over three weeks and were non-cytotoxic.

Polymer Nanoparticle Characterization and Applications for Drug Delivery

Rose Angela Roberts

GENERAL AUDIENCE ABSTRACT

Nanoparticle usage continues to increase in everyday products, from cosmetics to food preservation coatings, drug delivery to polymer fillers. Understanding the nature of nanoparticles is important to ensure safety and quality of commercial products, and production of particles allows for tailoring for specific applications. In this work, a technique to more easily create samples of cellulose nanocrystals (CNCs) for electron microscopy is developed. Electron microscopy can then be used to measure the size of these rod-like particles. Then, the technique is used to help develop a method to measure the concentration of CNCs in air. CNCs may irritate the lungs, so development of a way to measure their concentration in air is important to ensure safety of plant workers and consumers of CNCs. Characterization techniques of CNCs were used for synthesized particles used for brain cancer treatment. Synthesized particles contain the drug αCT1, which has been shown to reduce glioblastoma, or brain cancer, from becoming resistant to chemotherapy. These particles were made using poly(lactic-co-glycolic acid) (PLGA), a polymer that degrades in the body into lactic acid and glycolic acid. PLGA particles released αCT1 over three weeks and are of a size that is compatible with the brain. However, loading of the drug was low when using the first synthesis method. By switching particle synthesis methods, drug loading in the particles was increased by 1-2 orders of magnitude.

Dedication

To my family, whose love and support have carried me through my degree. To my husband, who keeps me lighthearted and grounded. To my mom, whose love I can always feel, even from far away. To my sisters, who have brought joy to my life since I can remember. To my dad, who inspired me to walk the less traveled path and do more than I could imagine.

Technical Acknowledgements

The work in this dissertation would not be possible without the help from many different groups of people. First, my advisor Johan Foster, who has guided my research and helped me grow into the researcher I am today. Second, my committee members Abby Whittington, Robert Gourdie, and Kevin Edgar, who have supported me through my degree. I would also like to thank the people in the Foster Advanced Materials Group who have helped me along the way, especially Kelly Stinson-Bagby, Priya Venkatraman, Keith Hendren, Payton Roberts, Garrison Ferrell, and Sara McBride. For all of the hours spent imaging under electron microscopy, I would like to thank Chris Winkler and Steve McCartney at the Nanoscale Characterization and Fabrication Laboratory. For work on projects concerning aerosolized cellulose nanocrystals, I would like to thank Kevin Gettz, Larissa Stebounova, Thomas Peters, and Jo Anne Shatkin for their contributions and hard work. For work surrounding the drug aCT1, I would like to thank Samy Lamouille for his help with cellular work and characterization of drug content. I would like to thank Zhi Sheng and Kevin Pridham for their work with mice and John Rossmeisl for his work with dogs (work not presented in this dissertation). I would also like to thank Christina Grek and Gautam Ghatnekar for their input into design parameters necessary for practical nanoparticles. For improving drug loading in the particles, I would like to thank Richey Davis and Ami Jo for providing access to flash nanoprecipitation mixers and input into parameters used for particle synthesis. For access to sterile environments to synthesize sterile particles, I would like to thank Michelle Theus, Xia Wang, Robert Gourdie, and Jane Jourdan. For irradiation of particles (work not presented in this dissertation), I would like to thank Michelle Theus and Amanda Hazy for equipment use. I would like to thank Abby Whittington, Shelley Cooke, Andre Stevenson, Jewel Cary, and Austin Ferguson for help with lyophilization and Richey Davis and Ami Jo for help with dynamic light scattering equipment. Additional thanks to Dr. Chip Frazier for allowing use of the autotitrator in his laboratory, used for data on cellulose nanocrystal work not presented in this thesis. Finally, I would like to thank all of the professors and staff who have supported my work over the past several years, including Thomas Staley, Carlos Suchicital, Christine Burgoyne, Diane Folz, Hesham Elmkharram, and Ibrahim Khalfallah.

Funding Acknowledgements

Research cannot exist without funding, so I would like to thank all of the groups who have supported this work financially. First, with much gratitude, I would like to thank the Materials Science and Engineering Department at Virginia Tech, who have supported me through teaching assistantships. Thanks to P3Nano for supporting three years of my research funding and FirstString Research for supporting all of my work with drug delivery. Additional thanks to National Institutes of Health and Macromolecular Innovations Institute, who have also providing funding in support of my research.

Table of Contents

Chapter 1

Introduction

1.1. Nanomaterials

Nanomaterials are slowly infiltrating consumer products, from wax nanodroplets on vegetables to metal oxide nanoparticles in sunscreen and cosmetics[1] and carbon nanotubes in airplane parts.[2] Polymeric nanoparticles have been found more useful in medical applications,[3] paints, coatings and adhesives,[4] and vitamins.[5] The scope of their importance and applications has only begun to surface, and more uses for polymeric nanoparticles are expected to arise.

Nanomaterials can be sourced naturally or synthesized. When isolated from nature, nanomaterials are more sustainable and generally biocompatible and biodegradable. However, because the source material may not always be the same due to environmental or other factors, the quality of the source material can change. Synthetic nanomaterials can be made using synthetic or natural sources, and may or may not be biodegradable. They are generally made using polymers, but ceramic, metal, or composite materials (using organics and inorganics), have also been used for nanomaterial production. The work presented here consists of two different nanoparticulate systems, the first surrounding the characterization of cellulose nanocrystals derived from nature and second involving the production of nanoparticles for drug delivery using synthetic polymers.

1.2. Polymeric Nanoparticles from Nature

Nanoparticles derived from natural sources can be found in plants, microbes, and animals. Peptides, proteins, peptidoglycans, and polysaccharides are examples of organic nanoparticles that can be isolated from nature.[6] Cellulose is an example of a polysaccharide from which nanoparticles, such as cellulose nanocrystals, can be isolated.

1.2.1. Cellulose

Cellulose is a polymer that can be found in trees, cotton, other plants, bacteria, and even tunicates. It has been used extensively in the paper industry,[7] textiles, and composites for use in medicine, construction, and automotive applications.[8-9]

Cellulose is a polysaccharide chain made of two anhydroglucose rings with a 1→4 linkage to form a β 1-4 glucosidic bond. Hydrogen bonding between inter- and intra-chain O3-H and O5

bonds provides the high axial chain stiffness distinctive of cellulose and creates the crystalline regions that increase the stiffness. Hydrogen bonds can form in different geometries, which produce different polymorphs of cellulose. There are at least four different polymorphs, in which polymorphs II, III and IV have slight structural differences in the cellulose crystal structure compared with cellulose I. Cellulose I is the native form found in the natural source, which can then be isolated and transformed into subsequent polymorphs. Cellulose I itself has two polymorphs, Iα and Iβ, which can be present simultaneously in varying ratios depending on the source material. Polymorph Iα has a triclinic structure in which the crystal-forming hydrogen bonds all meet at different angles. Polymorph Iβ is monoclinic, where two of the three angles between hydrogen meet at right angles.[10]

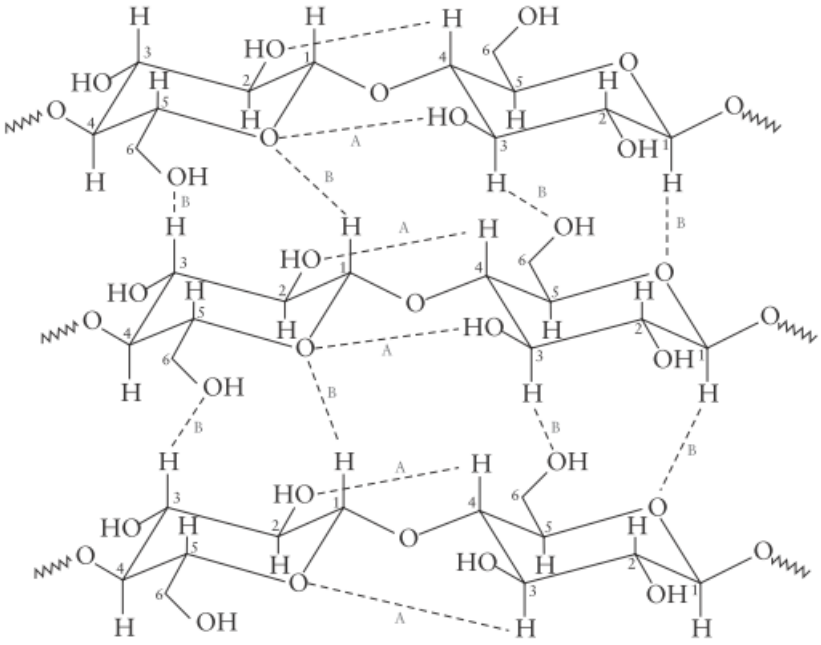

Figure 1.1. Structure of cellulose with intra- (A) and interchain (B) bonding.[8]

Like most polymers, cellulose has crystalline and amorphous regions. The crystalline regions, however, are unique in that they have a consistent size and aspect ratio. These crystalline regions are what gives plants and animals their structure, so trees can remain upright and bacterial cells can maintain their shape. Isolation of crystalline regions produces cellulose nanocrystals.

1.2.2. Cellulose Nanocrystals

Cellulose nanocrystals (CNCs) are the crystalline regions in cellulose, mostly containing Iβ (68-94%) crystalline regions.[11] They have a high aspect ratio (between 15-50) with diameters ranging from 5-20 nm and lengths between 50-1000 nm, depending on source. Generally, plant-derived CNCs are shorter and animal- and bacteria-derived CNCs are longer. Crystallinity of CNCs also changes depending on source and isolation method. The isolation method most commonly used is acid hydrolysis of a cellulose-rich pulp, wherein the acid dissolves the amorphous regions of cellulose. The crystalline regions remain behind due to strong hydrogen bonds resisting attack by the acid.[11]

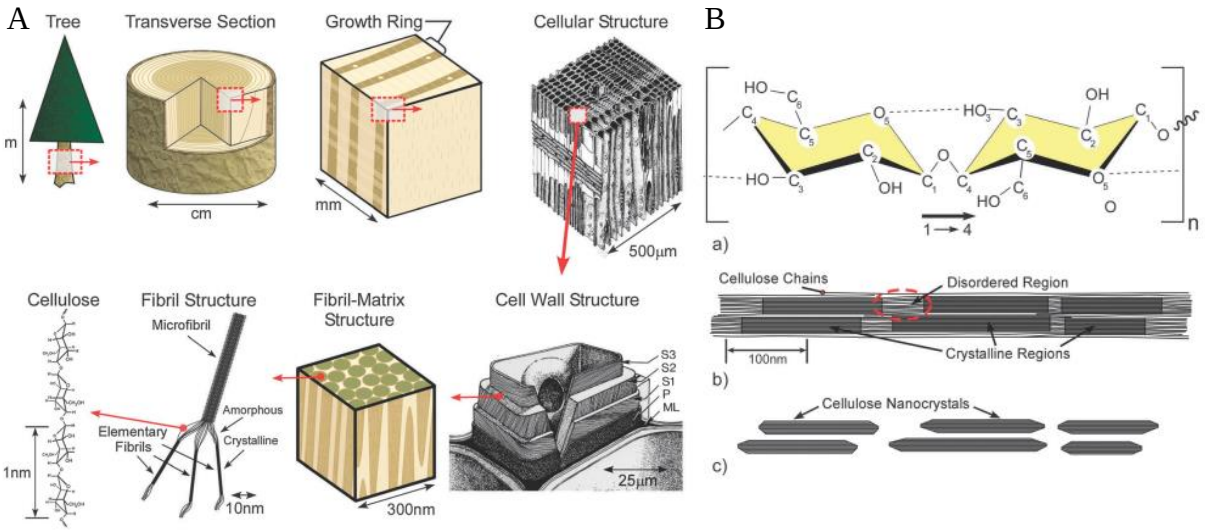

Figure 1.2. Isolation of cellulose nanocrystals from source material. "Republished with permission of Royal Society of Chemistry from Ref 11; permission conveyed through Copyright Clearance Center, Inc.[11]

Types of acid used for hydrolysis include sulfuric, hydrochloric, and phosphoric. The acid used can be important for application of CNCs, as the can acid functionalize the surface and give the CNCs a surface charge. The surface charge is advantageous because it helps the CNCs electrostatically disperse in solution. However, more functionalization of the surface lowers the thermal stability of the CNCs. For example, hydrochloric acid does not functionalize the surface of CNCs but sulfuric acid will leave sulfate groups. Hydrochloric acid isolated CNCs (H-CNCs) do not disperse easily in water while sulfuric acid derived CNCs (S-CNCs) disperse readily with

a few hours of bath sonication. S-CNCs, however, begin to degrade at 150 °C while H-CNCs degrade at a higher temperature of 220 °C.[12] Thus, choice of acid used for hydrolysis should be considered carefully depending on desired application.

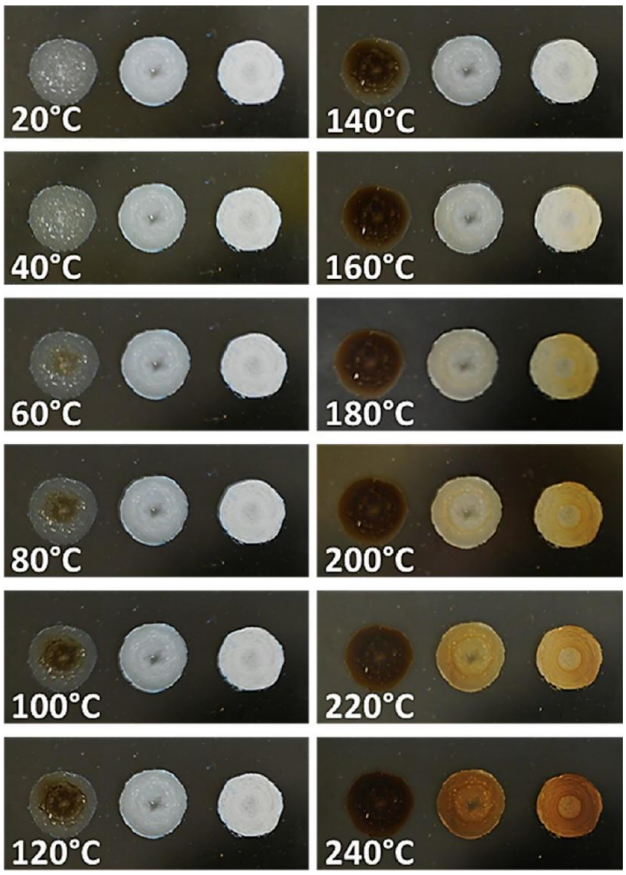

Figure 1.3. Pictures of solution-cast samples of CNCs from acid hydrolysis using sulfuric acid (left), phosphoric acid (middle), and hydrochloric acid (right). Reprinted (adapted) with permission from Ref 12. Copyright (2013) American Chemical Society.[12]

1.2.2.1. Applications of CNCs

CNCs are useful for a wide variety of applications, including liquid crystals, rheological modifiers, and polymer matrix reinforcement fillers to increase mechanical properties. Cellulose nanocrystals have been shown to exhibit chiral nematic and lyotropic liquid crystal domains (Liu 2014).[13] Nematic phases contain longitudinally-aligned CNCs while lyotropic regions are more fluid in nature.[11] Lyotropic liquid crystals contain more solvent than nematic phases which allows CNCs to form smaller areas of alignment dispersed throughout the solvent. Like other liquid

crystal systems, different shapes of orientation can occur based on CNC concentration.[14] Liquid crystal behavior is due to the longitudinal chiral twist that occurs in the CNCs, causing a packing arrangement that gives the highest packing density when the CNCs stack on each other at an angle. Size, concentration, electrolyte, external stimuli, and surface charge can affect the pitch angle and ordering of the CNCs.[11]

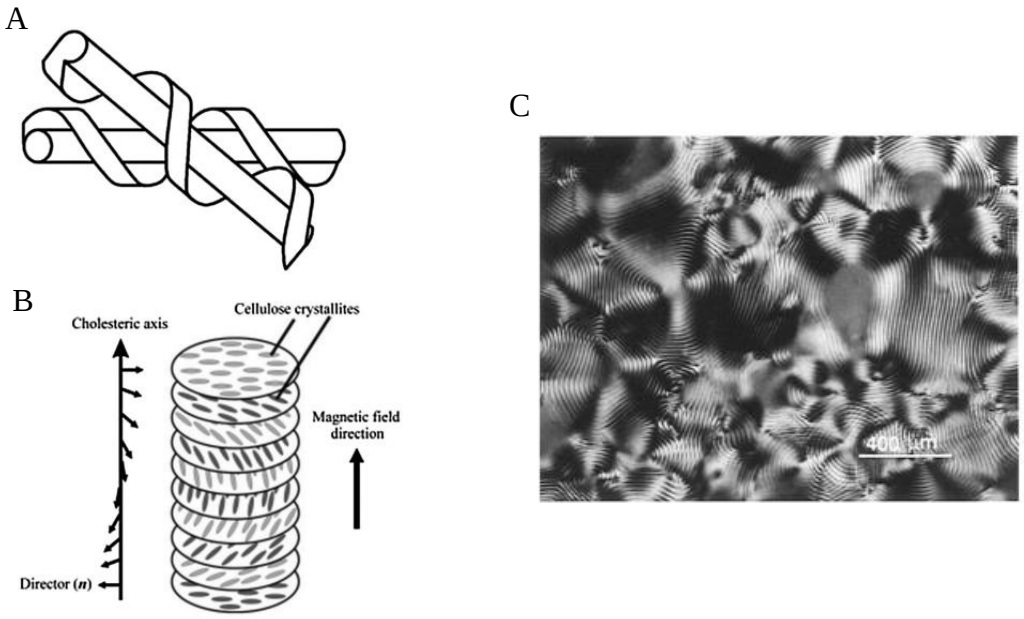

Figure 1.4. (a and b) Chirality of CNCs providing liquid crystalline behavior and self-assembly. Reprinted (adapted) with permission from Ref 15. Copyright (2001) John Wiley and Sons[15] and (c) Optical microscopy showing fingerprint texture of chiral nematic structure viewed through crossed polarizers. Reprinted (adapted) with permission from Ref 16. Copyright (1996) American Chemical Society.[16]

Size, concentration, and surface charge have also been shown to have effects upon the rheology of CNCs in solutions.[11] At low concentrations, CNCs show shear thinning behavior. Higher concentrations of CNCs show varying behavior that depends on shear rate, from shear-thinning behavior at low shear rates, a less-pronounced shear-thinning region at higher rates, and finally a drop in viscosity at a critical shear rate. At this critical shear rate, it is believed that the CNCs align, allowing the fluid to flow more easily.[11, 17]

CNCs can increase mechanical properties using a low weight percentage of CNCs in bulk material. This is due to the low percolation threshold provided by the high aspect ratio. The

percolation threshold is the concentration of CNCs or other particle required to begin to have an effect on the bulk material, and is largely independent of the matrix in which the CNCs are interacting. High aspect ratio particles often have low percolation thresholds, meaning only a small percentage of CNCs needs to be added in order to see reinforcement effects, such as increased stiffness, in a polymer or other matrix.[18] The CNCs reinforce the polymer via CNC-CNC hydrogen bonding.[19]

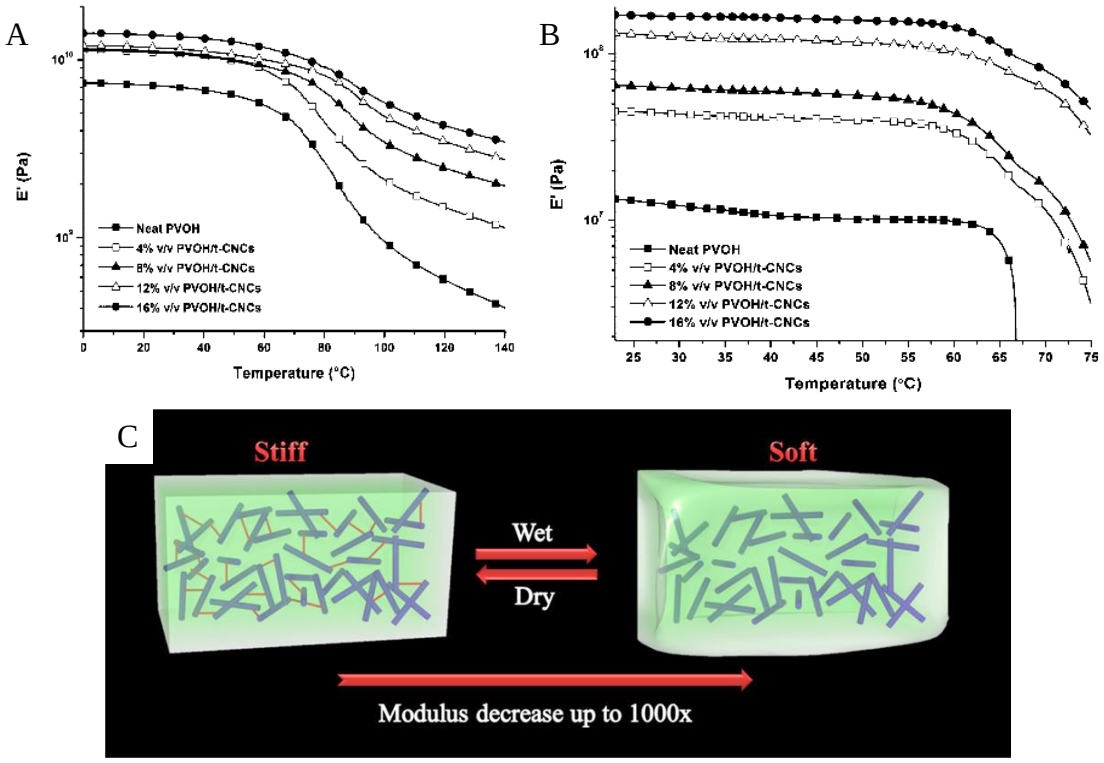

Figure 1.5. Dynamic mechanical analysis (DMA) of CNC-polyvinyl alcohol (PVOH) composites (a) dry and (b) soaked in artificial cerebralspinal fluid and (c) diagram of hydrogen bonds between CNCs breaking when water is present. Reprinted (adapted) with permission from Ref 20. Copyright (2013) American Chemical Society.[20]

This CNC-CNC hydrogen bonding can also be useful when developing stimuli-responsive materials, or smart materials. CNCs have been used to increase the stiffness of materials when dry, then decrease the stiffness upon contact with water.[21] One example is of a cortical electrode in which surgeons require a stiff material for implantation in the brain, but the brain cells interact best with materials of similar stiffness. Jorfi et al. created one such electrode, showing much less

scarring and increased activity of the electrode over time compared with stiffer silicon-based electrodes that are currently in use.[20]

1.2.2.2. Characterization of CNCs

In order to more fully understand and make use of CNCs, various characterization techniques are used. The main characteristics of CNCs that require characterization include particle dimensions (length and width, to calculate aspect ratio) and surface charge density. If CNCs are added to a polymer or liquid, additional characterization techniques should be used to characterize how the CNCs affect the bulk material. This could include rheology, dynamic mechanical analysis, and thermogravimetric analysis, in addition to atomic force microscopy (AFM) or transmission electron microscopy (TEM) to confirm dispersion of CNCs in the matrix. Here, characterization of CNCs alone is briefly described.

As the aspect ratio is one of the most useful characteristics for matrix reinforcement, as it affects the percolating network characteristics as described above, CNC dimensions can be measured via AFM, SEM, or more commonly TEM. Sample preparation often involves suspending CNCs in water or other dispersant, dropping the suspension on a sample substrate, and allowing the droplet to dry fully before imaging. However, obtaining accurate dimensions is challenging. Dispersion of the CNCs can be difficult and is often dependent on the dispersing solution and substrate being used, along with the surface chemistry of the CNCs. Substrate treatment, such as plasma treatment or glow discharge, before CNC deposition is often necessary in order to promote dispersion during drying of the CNC suspension. This requires specialized equipment. For imaging under electron microscopy, contrast between the substrate and sample is low due to similar atomic weights between them. High atomic weight stains are often used during sample preparation to increase contrast so the CNCs can be visualized. Stains can be negative or positive. Negative stains form a shadow around the particles, giving a dark background on which the lighter atomic weight CNCs can be visualized. Positive stains covalently bind to the surface of particles, so the particles themselves will appear dark against a bright background. The most common stain used for CNCs is uranyl acetate, a radioactive negative stain. Specialized equipment for substrate treatment and laboratory handling of radioactive stains can be difficult to put into place. This makes it difficult for some laboratories to achieve proper sample preparation in order to obtain clear images of CNCs. Dynamic light scattering (DLS) is another tool that can also be

used to estimate the hydrodynamic diameter of CNCs, but this is less accurate because the calculations assume a spherical particle, and because the aspect ratio cannot be measured using DLS.

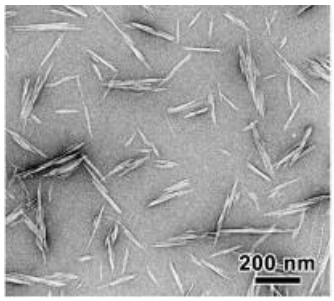

Figure 1.6. Transmission electron microscopy of CNCs with a negative stain. Reprinted (adapted) with permission from Ref 22. Copyright (2015) The Authors.[22]

Surface chemistry of CNCs is another key factor in behavior of CNCs in solution. Several methods of characterization should be used together in order to confirm functionalization. Surface charge density, used to measure charged functions on the surface of CNCs, is measured via conductometric titration. This becomes important to help determine how much the surface chemistry is affecting interactions with surrounding materials. Zeta potential of CNCs can indicate overall charge of the particle but, as the analysis is based on spherical particles, is not an accurate quantitative method for determining CNC surface charge. Fourier transform-infrared spectroscopy (FTIR) is used to help identify the surface chemistry of functional groups on the CNCs, often after functionalization has been performed in order to confirm the expected modification has been made. X-ray diffraction (XRD) is used to measure crystallinity, which can indicate how well the crystalline regions were isolated from the amorphous regions. This in turn can indicate how well the CNCs may reinforce a bulk polymeric material.[11] Crystallinity can be affected during functionalization, and so it is best to examine crystallinity of CNCs before and after functionalization in order to determine whether any change has occurred.

1.2.2.3. Potential Toxicity of CNCs

Use of CNMs is increasing, pushing companies to construct larger production plants in order to keep up with demand. Along with this push, safety of workers becomes a top priority, however the effect of CNCs on the body is not yet fully understood. Studies must consider long-

and short-term effects of oral, dermal, and respiratory exposure. Carcinogenicity and mutagenic effects, specific organ toxicity, and ecological effects also must be evaluated. In a 2016 evaluation of data gaps in health hazard classifications of CNCs, Shatkin et al. show that there is still insufficient data concerning the acute dermal and inhalation toxicity, eye damage or irritation, respiratory and skin sensitization, reproductive toxicity, and specific target organ toxicity.[23] In fact, the Safety Data Sheets (SDSs) of CNCs from the University of Maine use "estimated" and "expected" when listing toxicological effects.[24] While it is not expected that CNCs will differ greatly compared with cellulose based on the minimal chemical interactions with the body,[23-24] it is necessary to confirm in order to give consumers confidence in products containing CNCs.[25]

Of all potential sources of toxicity from CNCs, inhalation is the most likely source of danger.[26] Comparing the chemistry and aspect ratio of CNCs to other known materials raises some concerns about the potential for CNCs to be a lung irritant. Cellulose itself is a known irritant, and the aspect ratio of CNCs is similar to that of asbestos, a known carcinogen. High aspect ratio particles are difficult for cells to remove from the body.[17] Some studies show mixed results surrounding CNC-lung interaction, and more studies are needed to better understand long-term exposure responses in the body[27-28]. In the meantime, methods to quantify the concentration of CNCs in air at production facilities is needed so that safety standards can be put in place quickly as soon as cell studies have conclusive results.[29]

1.2.2.4. Aerosolized Nanoparticle Sampling Methods

Methods currently used in industry to quantify aerosolized particles include filter cassettes, nanoparticle respiratory deposition (NRD) samplers and impingers. Filter cassettes are standard for asbestos sampling, in which a canister contains a filter, diffuser, and support pad. The standard filter pore size ranges from 0.45-1.2 μm while the support pad pore size is 5 μm. The canister must be conductive in order to minimize effects from static charging (EPA standard).

NRDs are canisters similar to filter cassettes with several collection stages that mimic the deposition of particles in the human respiratory tract. The first stage of a NRD is the respirable cylone inlet, which removes 50% of particles that are larger than 4-5 μm. Then air moves through the impactor stage, which collects 50% of particles that are 300 nm or greater.[30] Finally, particulates flow through a diffusion phase in which a series of nylon meshes or granular beads are arranged to capture 50% of particles 40 nm or greater. Aerosolized particles are cycled through

the NRD for several hours, and then the collection stages are analyzed for quantity of particles. NRDs and impingers have been previously used to collect nanoparticulate salts and metals.[2, 30] Impingers are run in a similar manner, however instead of the particulates being captured by a filter, they are captured in a liquid. Liquid can be chosen to optimize collection efficiency.[29]

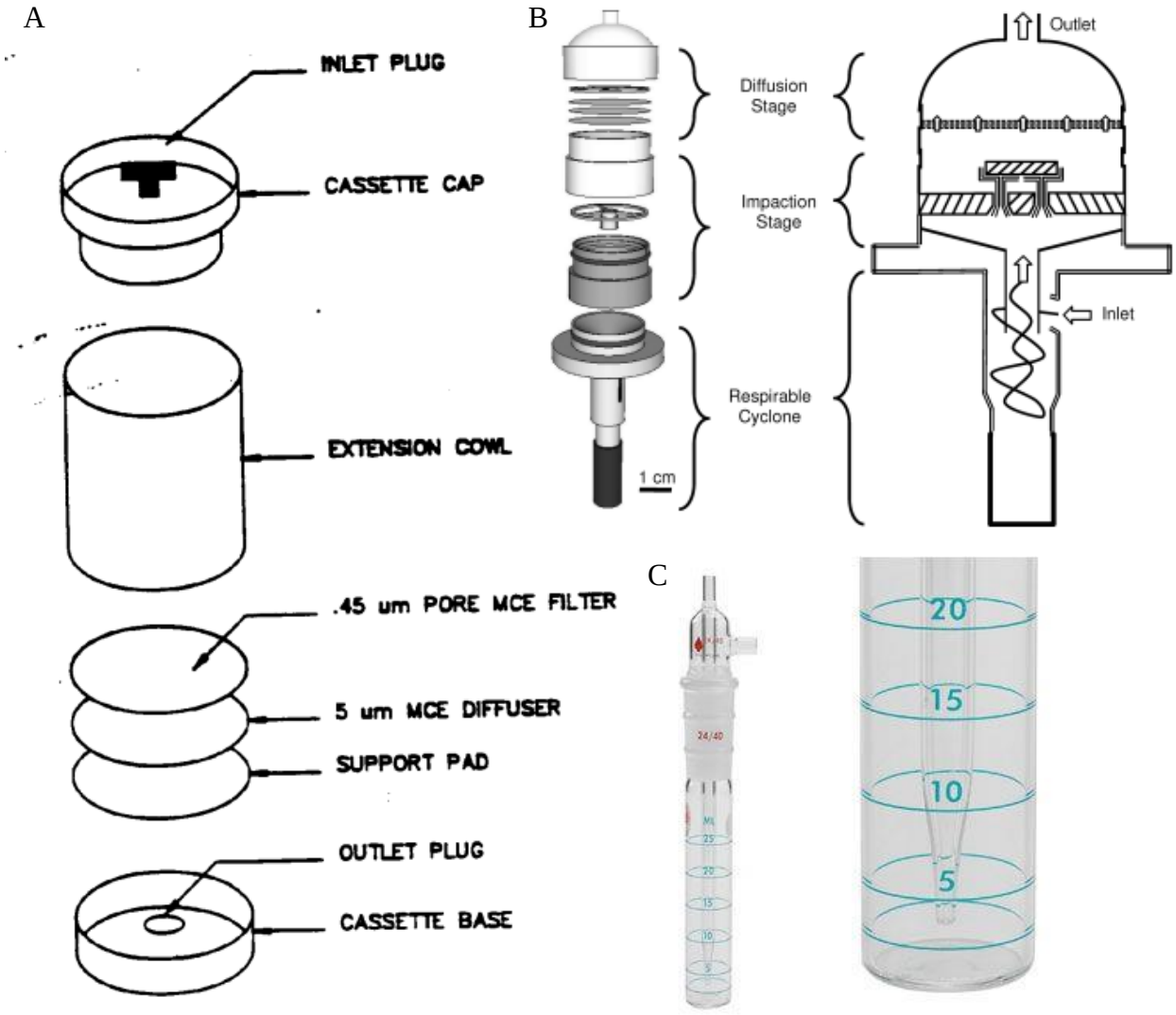

Figure 1.7. Types of samplers for collecting aerosolized particles. (a) filter cassette from Environmental Protection Agency asbestos sampler;[31] (b) NRD sampler, reprinted (adapted) with permission from Ref 32. Copyright (2011) American Chemical Society;[32] and (c) impinger, reprinted with permission from Zefon International.[33]

1.3. Man-made Polymeric Nanoparticles

Synthetic polymeric nanoparticles can use synthetic or natural polymers, which may or may not degrade. Synthetic polymers used include polyesters, polyanhydrides, polyurethanes, and polyamides, among others. Some polymers, such as the polyester poly(lactic acid), will degrade hydrolytically while others may only degrade enzymatically, such as the vinyl polymer polystyrene, or not at all, such as the methacrylate ester poly(methyl methacrylate).[34]

Nanoparticles made using naturally sourced polymers are generally more biocompatible than synthetic and are often degradable. Chitosan, derived from the shells of crustaceans, is widely used for antimicrobial applications and drug delivery. Alginate, sourced from algae, have also been used for drug delivery as well as hydrogels. Degradation of natural polymers often occurs due to hydrolysis or enzymatic means.

1.3.1. Advantages and Applications of Synthetic Nanoparticles

Nanoparticles from synthetic materials are generally used for drug delivery, imaging, and diagnostic applications.[35] Nanoparticles can improve the bioavailability of poorly water-soluble drugs, sustain the release of drugs over long periods of time, and reduce negative side effects of drugs.[36] Biodegradable particles also have the advantage that they do not need to be surgically removed after implantation.[36] This is especially advantageous for locations where surgery is unfeasible that may need targeted drug delivery.[35] One example of applications of polymeric nanoparticles is that they can be designed for antimicrobial applications, either by the polymer itself or materials added to the particle. For example, chitosan inherently has antimicrobial properties.[37] Polymers can be functionalized to be antimicrobial, such as using quaternary ammonium salts.[38] Antimicrobial metals, such as silver, can also be incorporated into particles for antimicrobial effects, such as with Janus particles.[39] Janus particles are any polymer that has different properties on one side of the particle compared with the other, such as hydrophobic on one side and hydrophilic on the other side.[40] Another advantage to polymeric nanoparticles is that they can be functionalized with relative ease, not just for antimicrobial purposes but also for targeted drug delivery such as for cancer treatment,[41] improving mucoadhesion for applications around mucous membranes,[42] and creating stimuli-responsive particles.[43]

1.3.2. Nanoparticulate Controlled Drug Delivery Systems

1.3.2.1. Polymer degradation and erosion

Polymers used for encapsulation can include natural or synthetic polymers, and most often degrade in some way over time. Natural polymers include polymers derived from a natural, renewable source, such as alginate, chitosan, or cellulose, derived from algae, crustacean shells, or plant matter (such as trees), respectively. Synthetic polymers used are generally polyesters or polyanhydrides, or some variation therein. Synthetic polymers can use molecules that are currently in the body, such as poly(lactic acid), in which the monomeric unit is lactic acid. Lactic acid is produced in the body and regional build-up causes soreness in muscles after a work-out. When polymerized and implanted in the body, lactic acid units break apart slowly and can be metabolized through the Krebb's cycle, which is the same route by which lactic acid produced by the body is metabolized.

Polymers engineered to degrade in the body may degrade by one or multiple routes. Hydrolysis is the most common route, but enzymatic degradation may also be likely, depending on the polymer used. For the purposes of drug encapsulation, polymer erosion from the encapsulating particle is as important as the degradation mechanism. Polymer erosion is how the degraded polymer pieces are removed from the bulk material. There are two main polymer erosion mechanisms, bulk and surface erosion. In bulk erosion, the entire bulk of the particle degrades at the same time. Then, channels in the bulk are usually formed that allow degraded polymer pieces to leave the bulk material. In this case, the bulk material has limited volume change, and could be described as the bulk dissolving at the same time. Polyesters, such as poly(lactic-co-glycolic acid) (PLGA), generally degrade via the bulk erosion mechanism. More information on the degradation of PLGA can be found in the Section 1.4. During surface erosion, only the surface of the material degrades. Here, the bulk material size decreases over time as the surface erodes away. The hydrophobicity of the polymer prevents water from absorbing fully into the particle, so only the surface in contact with water can degrade. Polyanhydrides degrade mostly using the surface erosion mechanism.

1.4. Poly(lactic-co-glycolic acid)

Poly(lactic-co-glycolic acid) (PLGA) is a well-studied polymer that has been used for a wide range of biomaterial applications. PLGA is a polyester made of lactic and glycolic acids,

which are metabolized by the body through the Kreb's cycle, which eventually excretes the degraded products through the lungs;[44-45] glycolic acid can also be secreted through the kidneys.[44] The glass transition temperature (Tg) of PLGA is above 37 °C, giving it a rigid chain structure and high mechanical strength.[44] It is polymerized using a random ring-opening copolymerization of the cyclic dimers of glycolic acid and lactic acid, generally in the presence of tin- or aluminum-based catalysts.[45] PLGA can also be polymerized by direct polycondensation of lactic acid and glycolic acid, preferably in the melt state, and tin can be used as a catalyst.[46] High molecular weights can be achieved using Lewis acids, organometallic compounds, or zinc catalyst.[46]

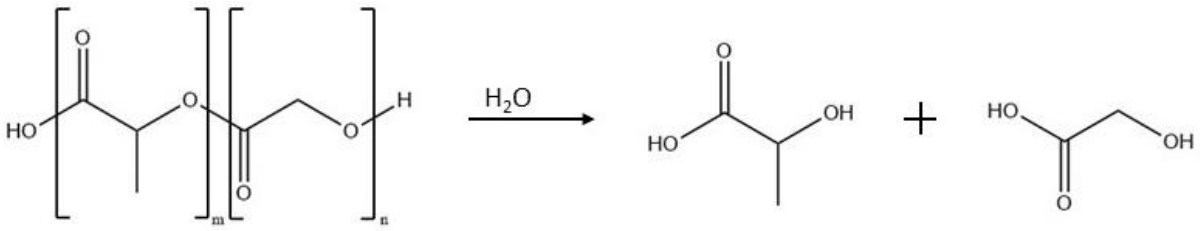

Figure 1.8. Chemical structure of poly(lactic-co-glycolic acid) and its degradation.

PLGA is most known for its ability to degrade via hydrolysis, which is useful when being used for tissue scaffolding or drug release. When used as a tissue scaffold, the degradation rate of the polymer can be tuned to the rate of growth of tissue, so that as the tissue grows the PLGA will be removed at approximately the same rate. For controlling drug release, the degradation rate of PLGA tunes the rate at which any encapsulated drug may be released, which is useful for long-term applications requiring drug elution for up to several weeks. PLGA is regarded by the Food and Drug Administration (FDA) as safe for several applications in the body (Jain 2000 for drug delivery),[44, 47] and its use in nanoparticles for drug delivery purposes is especially well-studied.

1.4.1. PLGA Degradation

The degradation of PLGA can be used to medicine's advantage. Tissue scaffolds made with PLGA can degrade at rates similar to the growth rate of tissue, so that the tissue can easily grow in to the space the PLGA scaffold has been protecting. Degradation is also advantageous when drugs are encapsulated, because the drug will be released as the PLGA degrades. PLGA

degradation can be tuned by changing its molecular weight, crystallinity, and size of the material being implanted.

PLGA undergoes chain scission reactions via hydrolysis, where water attacks the ester bond linkages to create a carboxylic acid end group and an alcohol end group.[44] During the degradation process, a decrease in polymer molecular weight occurs first, following first-order kinetics.[46] As the number of carboxylic acid end groups increases, the reaction can begin to autocatalyze if the degraded segments cannot be cleared from the bulk polymer[44] Once the chain segments are small enough to diffuse through the bulk system, the polymer begins to erode away. Large or bulk materials essentially degrade from the inside out, in which the core degrades more quickly than the surface, likely due to autocatalysis in the center of the material.[46]

1.4.1.1. Effect of Molecular Weight

Molecular weight is an important attribute for tuning PLGA degradation rate. Various molecular weights of PLGA can be easily purchased, ranging from 4,000-240,000 kDa.[48] With this large range of molecular weights, a large range of degradation rates is also available. In general, lower molecular weights degrade more quickly since low molecular weight polymers have a high elastic modulus, increasing deformability and ability for pores to expand during water uptake in the particles.[35, 49]

1.4.1.2. Effect of Crystallinity

Crystallinity is another way to tune degradation rate of PLGA, due to the additional presence of intermolecular bonds that must be cleaved for degradation to progress. Only amorphous regions are permeable and can take up water, and thus are accessible.[35] Crystallinity may be modified through several routes, including the ratio of lactic acid to glycolic acid and the ratio of D:L forms of the poly(lactic acid) groups. Poly(glycolic acid) (PGA) is highly crystalline while poly(lactic acid) (PLA) crystallinity is dependent on the ratio of D (PDLA) and L (PLLA) forms present. Lactic acid has an asymmetric α-carbon, typically denoted as having a D or L form rather than the traditional naming of R and S form, respectively. The L form is most used, however a mix of D and L forms is also prevalent. PLLA and PDLA are each semi-crystalline, but become amorphous when both are present in a polymer (PDLLA) due to the opposing chirality present.

The ratio of PGA to PLA also changes crystallinity. With a 50:50 ratio of the monomeric components and when D and L forms of PLA are present in equal proportions, polymer

crystallinity of poly(D,L-lactic acid-co-glycolic acid) is minimized, increasing degradation rate.[49-50] If either the PGA or PLA proportion is increased or only one PLA stereoisomer is present, crystallinity increases, causing a longer degradation time.[46] PLA is also more hydrophobic than PGA, and so an increase in the relative amount of PLA in the polymer decreases the rate of water absorption and thus also degradation. Length of degradation time is between 1-2, 4-5, and 5-6 months for 50:50, 75:25, and 85:15 L:G ratios[35, 46] while L-PLA degrades in >24 months, D,L-PLA in 12-16 months, and PGA in 6-12 months.[46]

1.4.1.3. Effect of Implant Size

PLGA degrades in a bulk erosion process. This is partly affected by the size of the PLGA inuse, such as nanoparticles, microparticles, or bulk/macro material. As water is absorbed by the polymer, mono- and oligomeric units are cleaved from the polymer. If the cleaved units are on the surface, they can escape into the surrounding medium, providing space for further cleaved units to escape. However, in the bulk material, the cleaved molecules do not have a route to exit the material. The additional carboxylic acid end groups begin decreasing the pH, catalyzing the degradation of surrounding material in an autocatalyzing event. It is postulated that a burst release of monomers from inside the bulk material is caused either by an increase in osmotic pressure by the reduction of pH or because the outer layer in which the surface groups can escape finally becomes thin enough to reach the now-porous interior of the material.[51] This mechanism of burst release has sometimes been shown to be quicker for smaller particles while others have shown degradation is quicker with larger particles. Surfactants, the drug loaded in the particles, and amount of drug loaded can also play a role in how water uptake and then PLGA degradation occurs.[51]

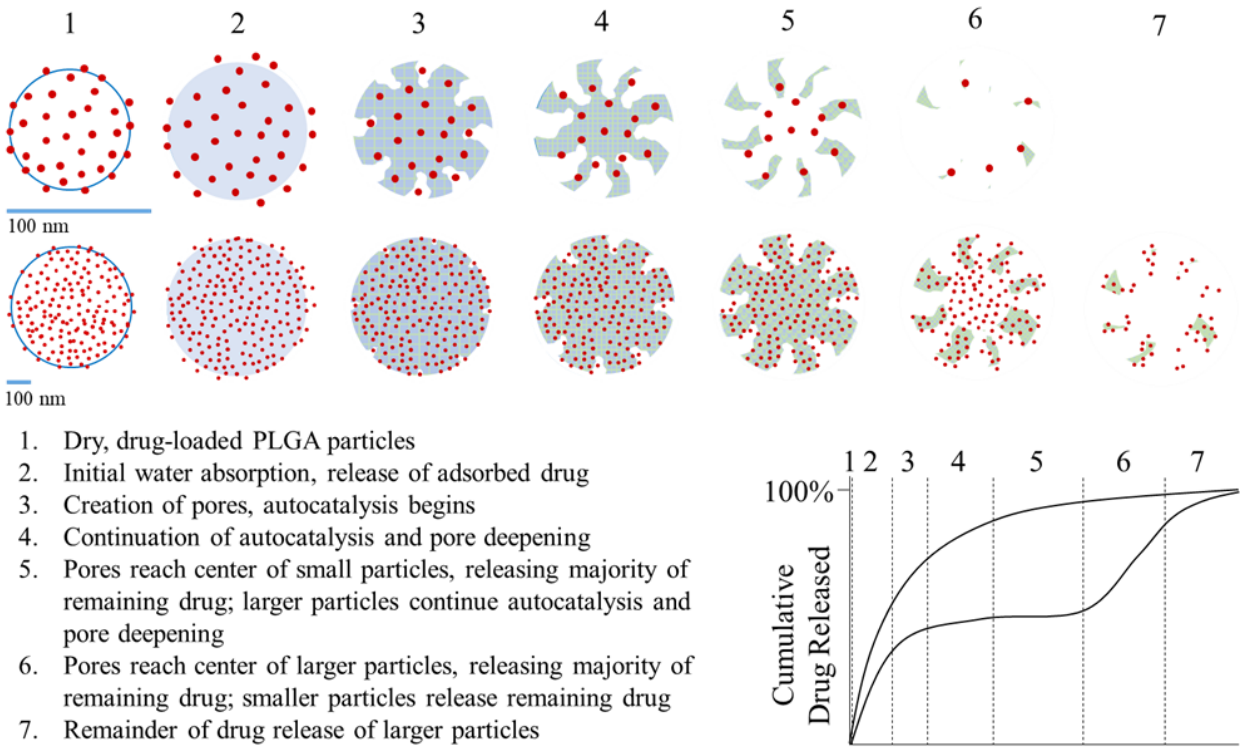

Figure 1.9. Degradation of PLGA particles that are nanoparticles (top row) and microparticles (bottom row). Progression from shows how the scale of the particles can effect the release profile.

1.4.1.4. Additional factors affecting degradation rates

Degradation of PLGA is a complicated process that is affected by many factors. Besides molecular weight, bulk material size, and crystallinity, several other factors can affect degradation rate. These include hydrophobicity and chemical, enzymatic or biological means of degradation. When hydrophobicity is increased, by either an increase in PLA content or functionalization, water diffusion through the polymer decreases, which decreases the rate of degradation via hydrolysis.[35, 49] Enzymatic degradation is another method of polymer degradation and erosion. In this case, an enzyme or protein can begin to break the ester linkages rather than water alone.[52] Additionally, as the polymer becomes porous and erodes, it becomes easier for enzymes to infiltrate the device and increase the rate of degradation.[46]

1.4.2. Current PLGA Drug-Dosing Devices in Use

PLGA has long been FDA-approved for several applications, most often in the forms of microspheres, in situ forming gels, or implants. The L:G ratios are reported from 50:50 to 85:15, although not all sources have ratio listed. The amount of PLGA present per dose ranges from 3.75

mg PLGA per dose up to 567 mg PLGA per dose of drug (Wang 2016 – FDA). FDA approval of PLGA in these applications will make it easier for materials made in the laboratory to make it as a product on the market more quickly, due to the 510(k) Premarket Notification process. This process helps the FDA identify whether a new device is equivalent to an already-approved device or if there are significant enough changes that have been made to the device compared with already approved devices that would require additional safety and effectiveness testing before approval.[53]

Table 1.1. FDA-Approved PLGA Devices.[47]

Drug Product	Active Ingredient	Dosage Form, Route of Administration	Strength,	Approval Date(s), Indication(s)	Characteristics of PLA/PLGA (described in product labeling)
Vivitrol	Naltrexone	Microsphere, Intramuscular	380 mg every 4-weeks	1984, Indicated for the treatment of alcohol dependence	PLGA, L/G: 75/25
Zoladex	Goserelin acetate	Implant, Subcutaneous	3.6 mg or 10.8 mg every 28 days	1989 (3.6 mg), 1996 (10.8 mg), Indicated for use in combination with flutamide for the management of locally confined Stage T2b-T4 carcinoma of the prostate	PLGA (13.3-14.3 mg/dose) No characterization information
Lupron Depot	Leuprolide acetate	Microsphere, Intramuscular	7.5 mg, every month 22.5 mg, every 3-months 30 mg, every 4-months 45 mg, every 6-months	1989, Indicated for palliative treatment of advanced prostatic cancer	7.5 mg: PLGA (66.2 mg/dose) 22.5 mg: PLA (198.6 mg/dose) 30 mg: PLA (264.8 mg/dose) 45 mg: PLA (169.9 mg/dose) No characterization information
Lupron Depot-PED	Leuprolide acetate	Microsphere, Intramuscular	7.5 mg, 11.25 mg, or 15 mg every month 11.25 mg or 30 mg every 3-months	1993, Indicated for the treatment of children with central precocious puberty (CPP)	7.5 mg, 11.25 mg, and 15 mg: PLGA (66.2/99.3/132.4 mg/dose) 11.25 mg and 30 mg: PLA (99.3/264.8 mg/dose) No characterization information
Lupron	Leuprolide acetate	Microsphere, Intramuscular	3.75 mg, every month	1995, Indicated for management of endometriosis	PLGA (33.1 mg/dose) No characterization information
Sandostatin LAR	Octreotide	Microsphere, Subcutaneous	10 mg, 20 mg, or 30 mg every 4-weeks	1998, Indicated for acromegaly, severe diarrhea/flushing episodes associated with metastatic carcinoid tumors, profuse watery diarrhea associated with VIP-secreting tumors	10 mg, 20 mg, and 30 mg: glucose star polymer, PLGA (188.8/377.6/566.4 mg/dose)
Atridox	Doxycycline hyclate	In situ forming gel Periodontal	50 mg	1998, Indicated for the treatment of chronic adult periodontitis for a gain in clinical attachment, reduction in probing depth, and reduction in bleeding on probing	PLA (36.7%/dose) No characterization data
Trelstar	Triptorelin pamoate	Microsphere, Intramuscular	3.75 mg every 4-weeks 11.25 mg every 12-weeks 22.5 mg every 24-weeks	2000 (3.75 mg), 2001 (11.25 mg), 2010 (22.5 mg), Indicated for the palliative treatment of advanced prostate cancer	3.75 mg, 11.25 mg, and 22.5 mg: PLGA (136/118/182 mg/dose) No characterization information
Arestin	Minocycline HCl	Microsphere, Periodontal	1 mg, variable dosing frequency	2001, Indicated as an adjunct to scaling and root planning procedures in patients with adult periodontitis	PLGA No characterization information
Eligard	Leuprolide acetate	In situ forming gel, Subcutaneous	7.5 mg every month 22.5 mg every 3-months 30 mg every 4-months 45 mg every 6-months	2002 (7.5 mg and 22.5 mg), 2003 (30 mg), and 2004 (45 mg), Indicated for the palliative treatment of advanced prostate cancer	7.5 mg: PLGA (82.5 mg/dose), carboxyl endgroups, L/G: 50/50 22.5 mg and 30 mg: PLGA (158.6/211.5 mg/dose), copolymer with hexanediol, L/G: 75/25 45 mg: PLGA (165 mg/dose), copolymer with hexanediol, L/G: 85/15
Risperdal Consta	Risperidone	Microsphere, Intramuscular	12.5 mg, 25 mg, 37.5 mg, or 50 mg every 2-weeks	2003, Indicated for the treatment of schizophrenia and bipolar I disorder	12.5 mg, 25 mg, 37,5 mg, and 50 mg: PLGA, L/G: 72/25
Ozurdex	Dexamethasone	Microsphere, Subcutaneous	0.7 mg, variable dosing frequency	2009, Indicated for the treatment of macular edema, non-infectious uveitis, and diabetic macular edema	PLGA No characterization information
Bydureon	Exenatide	Microsphere; Tablet	2 mg, every 7-days	2012, Indicated as an adjunct to diet and exercise to improve glycemic control in adults with type 2 diabetes	PLGA (37.2 mg/dose), L/G: 50/50
Lupaneta Pack	Leuprolide acetate; Norethindrone acetate	Intramuscular; Oral	3.75 mg every month; 5 mg daily	2012, Indicated for initial management of the painful symptoms of endometriosis and management of recurrence of symptoms	DL-lactic and glycolic acids copolymer (33.1 mg), no characterization data
Signifor LAR	Pasireotide pamoate	Microsphere, Intramuscular	20 mg, 40 mg, or 60 mg every 28-days	2014, Indicated for the treatment of patients with acromegaly	20 mg, 40 mg, and 60 mg: a mixture of two PLGAs per dose PLGA I (26.29/52.58/78.87 mg/dose), L/G: 50-60/40-50 PLGA II (26.29/52.58/78.87 mg/dose), L/G: 50/50

1.4.3. PLGA Nanoparticles

The usefulness of PLGA nanoparticles has quickly become apparent in the medical field for a large variety of applications. For many peptides, proteins, and nucleic acids, encapsulation

in PLGA nanoparticles can increase the half-life of these drugs in the body, protecting them from enzymatic or hydrolytic degradation as they reach their target location (Danhier 2012, Komaly 2016, Jain 2000).[35, 44, 54] It is also useful for encapsulation of antigens for the delivery of vaccines.[44, 54-55] Encapsulation of certain drugs, such as antibiotics and hydrophobic drugs, can also increase the drug bioavailability.[35, 54, 56] Surfaces of nanoparticles can also be coated or functionalized in order to target specific locations in the body, such as inflammatory and cerebral diseases, or specific organs such as the liver, brain, or ocular tissues.[54, 57] Nanoparticles themselves have an advantage over larger particles and implants in order to have suitable biodegradation kinetics.[44] These small particles also have the ability to penetrate deeper into tissue than larger particles via transport through small capillaries. They can also travel across fenestration in epithelial lining and have efficient cellular uptake.[45] PLGA nanoparticles specifically are useful because their degradation prevents the need for a second surgery to remove the implant, and no long-term toxicity issues have been reported.[58]

1.4.3.1. Nanoparticle synthesis methods

There are several methods that can be used to synthesize particles. Each has its own advantage, and there is not one method that is universal. Each method must be tailored to the drug, polymer, solvent, stabilizer, and other factors required by the system. However, the most common methods include emulsion-based methods and precipitation-based methods.

1.4.3.1.1. Emulsion Methods

Emulsion methods can be modified for either hydrophilic or hydrophobic drugs by using a single or double emulsion. When using emulsion methods, particle synthesis takes advantage of the oil-water interface to create nanodroplets of solvent containing polymer dispersed in an outer phase immiscible with the solvent. These are usually described as oil-in-water (o/w), water-in-oil-in-water (w/o/w), or the inverses of these (w/o, o/w/o). Solid-in-oil-in-water (s/o/w) methods are another modification of emulsion methods. High-energy sonication is used to decrease droplet sizes to the nanoscale. Surfactant is typically used to stabilize the particles while the polymer-containing phase evaporates. The high energy required to form droplets can damage sensitive drugs such as proteins and peptides and the oil-water interface has also been found to denature some proteins.[52]

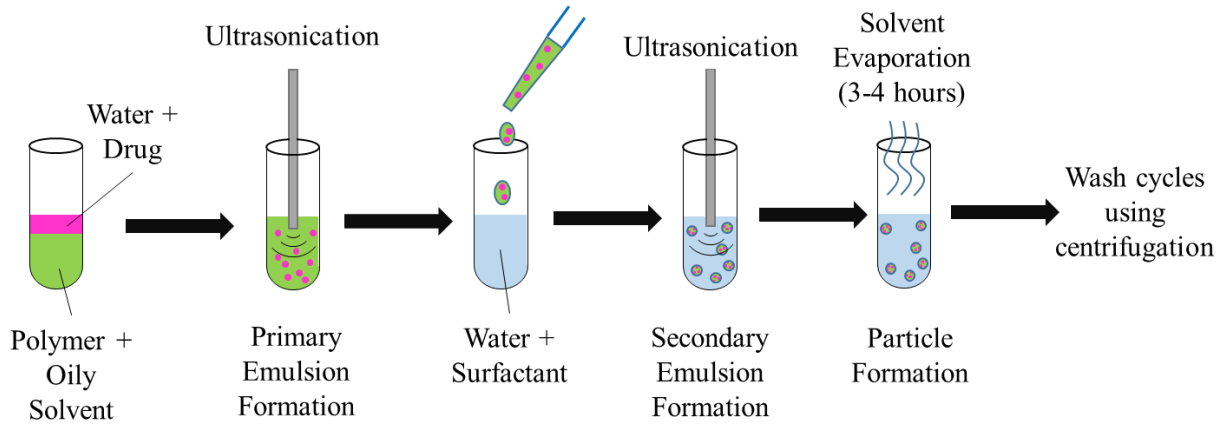

Figure 1.10. Double emulsion-solvent encapsulation method.

1.4.3.1.2. Precipitation Methods

Precipitation-based methods (also called solvent displacement or interfacial deposition) for particle encapsulation include precipitation, nanoprecipitation, and flash nanoprecipitation. Precipitation methods make use of two different solvents similar to emulsion systems, but differ in that the two solvents should be miscible with each other. One solvent should dissolve the polymer and the other should not (termed the non- or anti-solvent). When the two solutions are mixed together, the polymer precipitates out due to the presence of anti-solvent, forming particles. If the mixing is performed on a small enough time scale, via nano- or flash nanoprecipitation, then smaller particles can be achieved, down to the nanoscale. This process can be advantageous for encapsulating hydrophilic molecules, such as peptides, if solvent-antisolvent mixing times are on a small enough scale.[59]

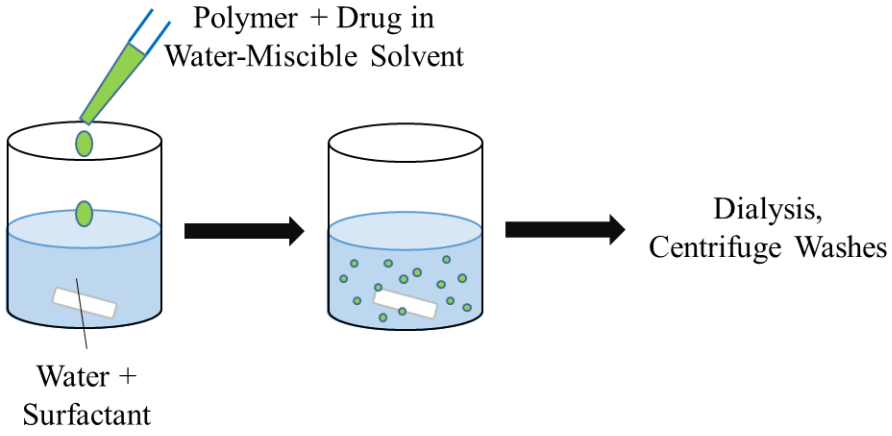

Figure 1.11. Nanoprecipitation method for nanoparticle synthesis.

1.4.3.1.3. Other Methods

Several other methods to make PLGA-NPs exist, including spray-drying, coacervation,[44] and salting out.[36, 60] Some variations on these methods include spray-freeze-drying, electrospraying, and a ProLease cold encapsulation method used for bioactive polymers.[35, 61-62] Particles can also be made in a bottom-up fashion, where PLGA is polymerized into a particle form, using direct polymerization techniques. [4]

Emulsification and precipitation techniques can also be modified and combined, such as the emulsification-diffusion method.[36, 60] In another modification, Murakami et al. used two solvents in the solvent phase of the precipitation method, having different affinities to PLGA and the stabilizer poly(vinyl alcohol).[63] Microfluidic channels have also been used to make particles with the concepts of emulsion or nanoprecipitation methods, in which the streams of fluid either take advantage of the oil-water interfaces or high-shear mixing helps form small precipitated particles for encapsulation of drugs.[35, 57, 64]

Table 1.2. Advantages and disadvantages of various particle synthesis methods for drug encapsulation.

Method [abbreviation]	Drug Type Best Used For	Advantages	Disadvantages	Refs
Single Emulsion [SE]	hydrophobic, lipophilic	Generally higher loading and encapsulation efficiency compared with NPr	Poor encapsulation efficiency for water-soluble drugs; detrimental to macromolecular drugs such as proteins; larger particles compared with NPr; adequate removal of surfactant	35-36, 44 65
Double Emulsion [DE]	hydrophilic, proteins, peptides	Moderate drug loading and encapsulation efficiency	Process variables significantly affect formation of particles; large number of steps; temperature and viscosity must be controlled; detrimental to macromolecular drugs such as proteins; larger particles compared with NPr; adequate removal of surfactant	35, 44, 65
Nanoprecipitation [NPr]/Flash Nanoprecipitation [FNPr]	hydrophobic, hydrophilic, proteins, peptides, lipophilic, inorganic colloids	Simplicity; ease of scalability; good reproducibility; small amounts of solvent used; narrow size distribution; no high-energy input required; high loading capacity; multiple drug encapsulation in the same particle; potential continuous synthesis for FNPr	Sometimes requires dialysis; FNPr requires a mixer; choice of drug/polymer/solvent/nonsolvent system to ensusre high loading and encapsulation; residual solvent in particles	36, 57
Coacervation	hydrophobic and hydrophilic	Solvent does not need to be immiscible with water, boiling point of solvent can be higher than water	Slow process; agglomeration issues; kinetically-controlled and highly affected by process variables	44
Spray-dry	hydrophobic, some hydrophilic	Rapid; easy scale-up	Significant loss of product due to wall adhesion; agglomeration	44
Microfluidics	hydrophobic and hydrophilic	In-line characterization; feedback control; continuous synthesis; higher drug loading	Requires microfluidic device, usually involving soft lithography	35

1.4.3.2. Drug Encapsulation and Release from PLGA-NPs

1.4.3.2.4. Drug Encapsulation and Loading

Many different sizes of drugs with varying affinities can be encapsulated through several different routes. Encapsulation method of choice is largely dependent on the type of drug to be encapsulated. Drug loading and encapsulation efficiency, described in

Equation 1 and Equation 2, are usually maximized by adjusting several processing parameters. These parameters normally include shear rate, surfactant type and concentration, polymer concentration, and type of solvent used.[41, 66-68] Other additives, such as ion pairing, and processing steps, such as multiple emulsion or nanoprecipitation steps, can also be used to increase drug loading.[69-71]

Equation 1

$$Drug\ Loading = \frac{Mass\ of\ Drug\ in\ Particles}{Mass\ of\ Recovered\ Particles} \times 100\%$$

Equation 2

$$Loading\ Efficiency = \frac{Mass\ of\ Drug\ in\ Particles}{Mass\ of\ Drug\ Used\ in\ Synthesis} \times 100\%$$

1.4.3.2.5. Drug Release

Drug release is dependent on polymer type used (molecular weight, crystallinity, L:G ratio, etc.), but is also dependent on the drug itself and its ability to move through the particle during the release.[49] Soppimath et al. describe drug release as being dependent on the following factors:[72]

1. Desorption of surface-bound or adsorbed drug
2. Diffusion of drugs through the bulk particle matrix
3. Diffusion of drugs through the particle wall/surface
4. Particle matrix erosion
5. Combined erosion and diffusion process

A similar description of drug release explanations is described by Komaly et al.:[35]

1. Drug diffusion through water-filled pores
2. Diffusion through polymer matrix
3. Osmotic pumping
4. Erosion

Soppimath and Komaly agree on drug diffusion, but differ in that one is bulk diffusion through the matrix or surface and the other through either the matrix or pores in the particles. Erosion is another common factor described, although Komaly goes into further description on how erosion can be either surface or bulk rather erosion. Komaly also differs from Soppimath in that osmotic pumping could be a potential reason why drug is eluting from the polymer. In this case, as the polymer begins to swell from water uptake, the osmotic pressure within the particle increases, driving the drug out to the surrounding lower-pressure media. The final difference is that Soppimath mentions desorption of drug from the surface of the particle, which Komaly does not mention. This is often the case when polymer-drug solubility is low, so little drug gets incorporated in the center of the particle, and instead lies near the surface of the particle or is simply adsorbed to the outside surface.[35, 72-73]

These factors combine to produce different types of release profiles. Figure 1.12 describes several common types of profiles. Most commonly, burst release profiles will be observed if the drug is near the surface, or the drug is small enough to diffuse through the particle easily. In this case, the polymer does not need to fully degrade in order for drug to be released. A linear, or first-order, release profile is ideal for applications when a constant drug concentration in plasma is desired, and is achieved when a steady rate of drug is eluted from the particle. Triphasic profiles are often observed with macromolecular drug delivery. Large molecules adsorbed to the surface desorb during the initial burst release phase. In the second phase, limited drug is released because it is too large to diffuse through the particle while the matrix is still intact. In the third phase, the polymer matrix begins to erode away, forming channels that allow the macromolecules diffuse out of the polymer.[35, 72] The preferred profile is highly dependent on the needs of the application, and additional *in vivo* testing is usually required to optimize the desired therapeutic effect.

Table 1.3Table 1.3 gives examples of several types of drugs encapsulated and their release profiles.

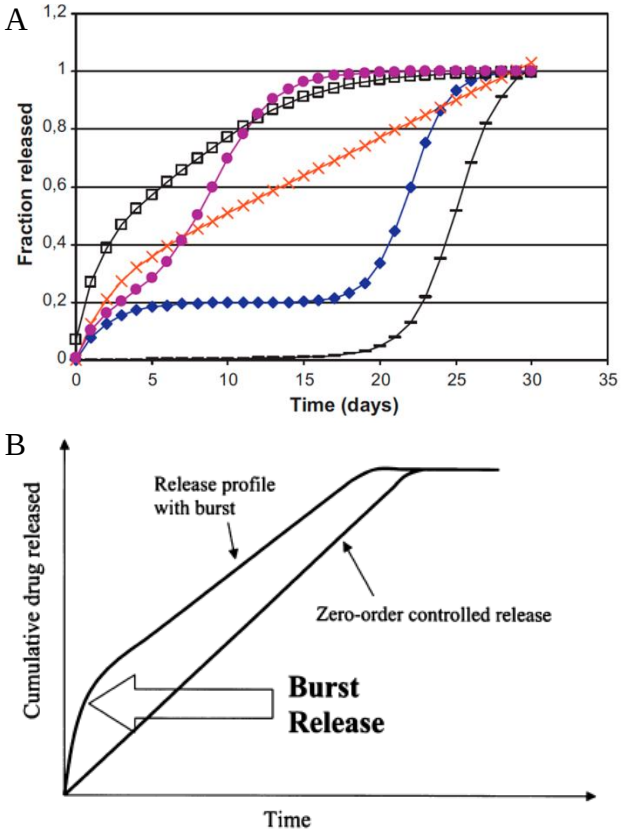

Figure 1.12. Example drug release profiles. A) open squares: burst and rapid phase II; filled circles: triphasic release with short phase II; crosses: burst and zero-order release; filled diamonds: triphasic release; dashes: biphasic release without burst release. Reprinted with permissions from Elsevier © 2011.[74] B) Description of burst release and zero-order release of drug. Reprinted with permissions from Elsevier © 2001.[75]

Table 1.3. Release profiles of various drugs from PLGA.

Drug Encapsulated (ion pairing complex)	Drug Affinity, Size*	Encapsulation Method	Release Profile, time studied	Ref.
Benzocaine	Hydrophobic, Small	Nanoprecipitation	Burst, 8 hrs	[76]
Curcumin	Hydrophobic, Small	Single emulsion-solvent evaporation	Burst followed by linear, 19 days	[77]
Paclitaxel	Hydrophobic, Small	Single emulsion	Triphasic and burst release (surfactant dependant), 40 days	[68]
Gemcitabine hydrochloride	Hydrophilic, Small	Double emulsion-solvent evaporation	Burst followed by linear, 12 hrs	[67]
Fluorescein	Hydrophilic, Small	Microfluidic via emulsion and precipitation methods	Burst, 30 hrs	[64]
Loperamide HCl (dextran sulphate)	Lipophilic, Small	Coacervation for ion pairing, s/o/w for encapsulation	Burst followed by linear, 6 days	[78]
Palmitic acid-modified exendin-4 and exendin-4	Hydrophilic peptide, Intermediate	Emulsification, in steps to encapsulate in PLGA then coat with chitosan	Burst followed by linear or triphasic, 3 days	[71]
Insulin (various zinc salts)	Hydrophilic protein, Large	Double emulsion-solvent evaporation	Burst followed by linear, 21 days	[79]
Human serum albumin	Hydrophilic, Large	Emulsion-diffusion	Burst or triphasic, up to 30 days	[80]
Endostar	Hydrophilic protein, Large	Double emulsion-solvent evaporation	Burst, 5 weeks	[81]
Lysozyme and α-chymotrypsin	Hydrophilic protein, Large	Two-step nanoprecipitation	Triphasic, 100 days	[82]

*Drug sizes: Small < 1 kDa, 1 kDa < Intermediate < 5 kDa, 5 kDa < Large

1.4.3.3. Toxicity and Bioaccumulation of PLGA-NPs

One advantage of nanoparticles is that the material used can have different properties when on the nano-scale compared with macro-scale. However, this can also mean that nano-scale materials have different toxicities when nano-sized. Nanomaterials can interact with areas of the body that larger particles cannot, such as entering cells through phagocytosis rather than

interacting with only the surface of cells.[83] Bulk PLGA implants show little to no inflammatory response. If there is a small amount of inflammation that occurs, it diminishes over time, and no toxicity or allergic responses have been observed.[46] However, some foreign body responses have been observed, which is most often attributed to PLGA's hydrophobicity.[46, 54] While biological responses to bulk PLGA are limited, responses to nanoparticles should be observed.

1.4.3.3.6. Cytotoxicity

For PLGA nanoparticles, it is most often reported that little cytotoxicity is present when cells are exposed,[84-85] which is expected of a system similar to that which has been previously approved by the FDA. When some toxicity has been reported, the cause is most often linked to an increase in inflammation or reactive oxygen species (ROS),[86-87] but this has also been linked to the degradation products of PLGA not being cleared away from the cells at the site of administration.[88] It has been shown, however, that the shape of NPs can have an effect on cytotoxicity. In a study using PLGA-PEG (poly(ethylene glycol)), spherical- and needle-shaped particles were tested in HepG2 cells, or human hepatocellular carcinoma (liver cancer) cells. It was found that needle-shaped particles lysed the lysosome during the endocytosis process, causing damage to the cell's DNA and eventually causing cell death while spherical particles showed no toxicity.[89] Surface functionalization may also play a role in biological responses. In a study by Platel et al., positively charged nanoparticles were shown to be cytotoxic by increasing ROS induction and high endocytosis due to induction of chromosomal aberrations. Neutral and negatively charged NPs in contrast were found to be relatively inert.[90]

1.4.3.3.7. Bioaccumulation

Bioaccumulation, or where the material tends to accumulate in the body, must also be considered with nanoparticles. Accumulation areas must be taken into account when designing particles for appropriate target delivery and duration in the body to be a match for therapeutic goals. It has been found that PLGA-NPs often accumulate in the liver, spleen, lymph nodes, bone marrow, and peritoneal macrophages.[49] For example, when administered orally in rats over seven days, an insignificant amount of PLGA-NPs were found to accumulate in the spleen (0.6% total dose/g), followed by intestines (0.28%) and kidney (0.3%), then liver, lung, heart, and brain (each less than 0.2%).[91] In another study, PLGA-NPs were administered to rats intravenously. After two hours, 18.8% of the dose accumulated in the liver, 5.0% in the intestine, 4.3% in the kidneys, and

2.3% in the blood.[92] The differences in accumulation are likely due to the administration route of the NPs. It has also been shown that functionalized or coated PLGA-NPs may accumulate in the body at higher rates compared with non-functionalized PLGA-NPs.[85-87] Additionally, the liver and spleen are common locations for hydrophobic particles to accumulate since the reticulo-endothelial system (RES) views them as foreign bodies, which is commonly addressed by coating the particles with a hydrophilic surface layer[54] or other molecules, such as peptides, in order to allow the particles to pass through various tissues.[93]

1.4.3.3.8. Role of PLGA-NPs Reduction of Drug Toxicity

In other studies, PLGA has been shown to reduce or eliminate the toxicity of drugs and other particles by limiting tissue exposure to the encapsulated drug until particles are at the target location.[57, 94] For example, thioridazine is a toxic drug that can be used in conjunction with rifampicin in order to treat *Mycobacterium tuberculosis* and *Mycobacterium bovis*. However, because of its toxicity, thioridazine in not widely used. In a study by Vibe et al., encapsulating thioridazine in PLGA reduces or eliminates its toxicity in zebrafish embryos, and when used with rifampicin significantly increases the survival rate of the fish that have been infected with *M. tuberculosis* and *M. bovis*.[94] Hung et al. also showed a reduction in cytotoxicity of photosensitizers when encapsulated in PLGA. Photosensitizers are drugs that react when triggered by UV light, but can be cytotoxic without light when used at high concentration. It was found that the PLGA coating protects the photosensitizer from reactions with tissue until embedded in the target location, at which point the light source can be activated and the drug can remain localized.[95]

1.5. Connexin43 Mimetic Peptide Drug αCT1

αCT1, or alpha-connexin carboxyl-terminal peptide 1, is a synthetic peptide drug shown to decrease chronic wound healing time, decrease scar tissue formation on the skin and internally such as heart tissue, and reduce glioblastoma resistance to chemotherapeutics.[96-97] The drug is currently in Phase III trials for FDA approval (last stage of human trials before approval) for topical wound healing applications. The broad range of applications of the drug is hypothesized to be due to the effect it has on cell-to-cell interactions and communication.

1.5.1. Properties of αCT1

αCT1 is a peptide containing 25 amino acid groups. Its sequence is RQPKIWFPNRRKPWKKRPRPDDLEI and has a molecular weight of 3484. It hydrophilic, has a

pI of 11.95, and a net negative charge below its pI. During studies, a randomized sequence of the same amino acid groups can be used a negative control; the antennaepedia end can also be used as a negative control. Biotin is used as a marker on the αCT1 in order to facilitate the use of ELISA assay for quantitation.

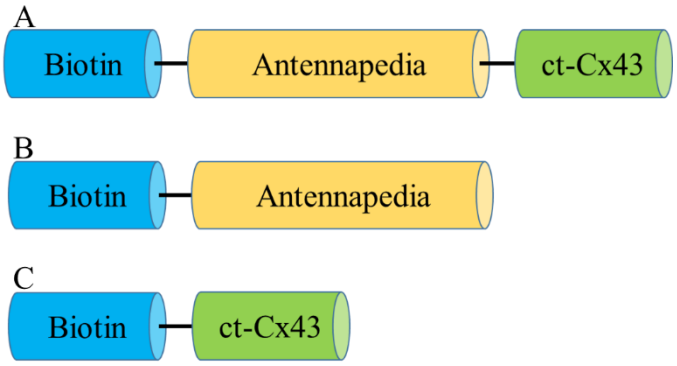

Figure 1.13. Configuration of A) αCT1, B) antennapedia only, and C) Cx43 mimic only.

1.5.2. Cellular Communication: Connexins, Gap Junctions, and αCT1 Interactions

When multicellular organisms began to form, one necessity for cells to coordinate was the ability to communicate. Cells can communicate by indirect means, especially if cells are distanced from each other, by excreting small molecules and hormones into the extracellular space that will eventually reach the target cell. Cells also communicate directly by forming connections with each other through which small molecules and hormones can be transferred.[98] These connections are called gap junctions, which are made of integral proteins. Integral proteins have some portion of their structure embedded in the cell membrane, and most often completely span the phospholipid bilayer.[99] The integral proteins that form gap junctions are called connexins. When six connexins oligomerize in a circular structure, they form a connexon, or hemichannel. Hemichannels allow the movement of small molecules across the cell membrane, especially ATP and glutamate, in the extracellular space.[100] When connexons on adjacent cells couple, a gap junction is formed for direct transfer of molecules and ions (<1-2 kDa) from one cell to another, usually based on osmotic pressure differences.[98, 101]

Many connexins (Cx) have been found so far, each affecting different diseases. Cx26 has been found to affect deafness while Cx50 is linked with cataracts. Cx43 has been linked to oculodentodigital dysplasia, heart defects, and ventricular disease.[98] Cx43 is also critical for

neurodevelopment, as Cx43 is expressed in oligodendrocytes, astrocytes, and microglia.[100] Endothelial cells also express Cx43, likely in part because endothelial cells are regulated by adjacent astocytes.[100] Cx43 plays an important role in tissue development and homeostasis, such that one study demonstrated that Cx43 knockout mice expressed heart malformations and could not survive after birth.[102]

αCT1 mimics Cx43, which in turn modifies how Cx43 is expressed in a cell. A binding partner of Cx43 is the protein zonula occludens (ZO-1), with which αCT1 competitively binds. Cx43 interactions with ZO-1 have been shown to change the gap junction remodeling and cellular communication. By preventing Cx43 binding to ZO-1, intracellular gap junction communication is increased while Cx43 hemichannel activity is decreased. This mechanism could explain why αCT1 reduces the resistance of glioma cells from becoming resistant to the chemotherapeutic temozolomide, among other therapeutic activity such as reducing inflammation, reducing scar tissue formation, and healing chronic wounds.[96-97]

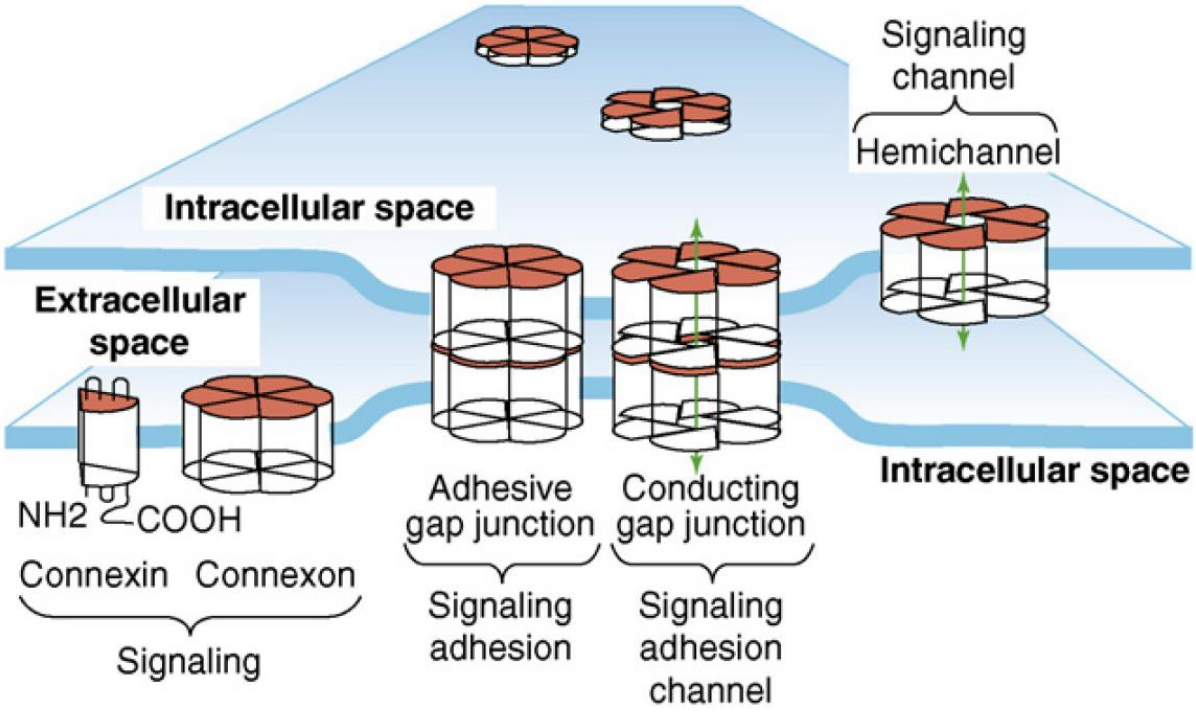

Figure 1.14. Schematic of connexons, gap junctions, and hemichannels. Left: Connexin proteins that form into connexons. Right: Connexons create hemichannels when opened, allowing flow of small molecules and ions between the cell and extracellular space. Middle: Gap junctions formed when hemichannels from two adjoining cells come together. Reprinted from Ref 103, with permission from Elsevier.[103]

1.5.3. Limitations and Side Effects of αCT1

The main limitation to αCT1 is that it is a relatively small molecule, only 25 amino acids in length (MW 3485), and the body can metabolize it quickly, in an estimated 24 hours or less. For long-term treatments such as chronic wounds and cancer, price of treatment increases and patient compliance decreases. The other limitation for αCT1 is the side effects, which have so far been found to include decreased activity, breathing abnormalities, piloerection, prostration, and wobbly gait when administered intraveneously at concentrations of 10 mg/kg or greater, which resolved after 24 hours.[96]

1.5.4. Glioblastoma

1.5.4.1. Glioblastoma and Treatment Resistance

Glioblastoma multiform is a deadly brain cancer that contributes to 15% of all brain tumors.[104] The survival rate of patients two years after diagnosis is 27%[105] and less than 5% five years after diagnosis.[97] Glioblastoma is difficult to treat for two main reasons. The first is that cancer cell tendrils infiltrate into sensitive areas of the brain, making full surgical removal impossible.[105-106] The second is they become resistant to chemotherapeutics quickly.[101]

Cancer cell resistance to therapy arises for a variety of reasons. First, intra- and inter-tumor heterogeneity makes treatment difficult, partly due to the presence of glioblastoma stem cells (GSCs). GSCs contribute to treatment resistance due to their refraction of radiation and chemotherapy. Glioblastoma tumors also have large regions with reduced oxygen levels, which also limit the amount of DNA-damaging free radicals produced during ionizing radiation.[106] The tumor also exhibits high hydrostatic pressure due to abnormal and leaky vasculature, which limits the ability of drugs to reach the tumor.[106]

Current treatment methods include surgical resection of the tumor followed by radiation and chemotherapeutic treatment, mainly using temozolomide (TMZ). However, treatment methods only prolong life an average of 2.5 months.[97]

1.5.4.2. Current Standard of Care

Glioblastoma is currently treated by surgical resection, chemotherapy, and ionizing radiation. Chemotherapeutic drugs are limited in impact due to inability to cross the blood brain barrier (BBB). The current standard therapeutic is temozolomide (TMZ), which is a hydrophobic small molecule that readily passes through the BBB. TMZ causes DNA lesions in cancer cells due

to its DNA-alkylating ability.[97] Other therapeutics include carmustine, lomustine, gleostine, carboplatin, etoposide, ironitecan, and Gliadel®, a biodegradable wafer encapsulating carmustine, however all of these except carmustine, lomustine, and Gliadel have been approved for cancers other than glioblastoma, so if used must be prescribed "off label" for use in brain tumors.[105-106]

1.5.4.3. Other Treatment Methods

There are a few treatment methods that go beyond the standard of care. Convection-enhanced delivery (CED) is a treatment method that slowly infuses chemotherapeutics directly to the tumor site to replace other routes of administration.[105] Two approved routes of glioblastoma treatment do not make use of radiation or chemotherapy. The first is called Nanotherm™, which is approved for use in the European Union. This therapy injects magnetic particles directly into the tumor and then alternates magnetic fields to selectively heat cancer cells, leading to cancer cell death.[107] The second is Optune, a wearable, portable FDA-approved therapeutic device that uses electric fields to interrupt cancer cell division.[108] Cells undergo apoptosis, or cell death, after attempting to divide. Electric fields disrupt formation of tubulin into spindle structures, which are required to separate chromosomes into daughter cells during mitosis.[108-109] Since the cell cannot finish division, it undergoes cell death.[108]

1.5.4.4. Role of αCT1 and Cellular Communication in Glioblastoma

Glioblastoma cells contain the protein connexin 43 (Cx43), a tumor-suppressing gene that forms hemichannels in cell membranes for cellular communication.[102] Expression of Cx43 in glioblastoma is unsurprising due to the prevalence of Cx43 present in a variety of neuronal tissue.[100] It has been found that gap junctions also play an important role in glioblastoma chemoresistance due to intercellular communication.[101] Specifically, cells in which expression of Cx43 was high showed a higher incidence of chemoresistance,[97, 101] although other studies found conflicting results, where Cx43 expression was tied to increased cytotoxicity to chemotherapeutics.[110] The contradiction has been attributed to differences in experimentation methods, however it is clear that Cx43 effects chemoresistance.[111]

In a study by Gielen et al., cells expressing a modified Cx43 gene that precluded the carboxyl terminus decreased glioblastoma resistance to TMZ.[112] Similarly, Murphy et al. used a Cx43 peptide mimic, αCT1, to study effects on chemoresistance. It was found that glioblastoma stem cells remained sensitive to TMZ. Murphy postulated that αCT1 induces cell death by

inhibiting the AKT/AMPK/MTOR signaling pathway, sensitizing cancer cells to TMZ.[97] This set of pathways are a response to metabolic stress in order to return to homeostasis when reactive oxygen species are overproduced.[113] Thus when the pathway is blocked, toxic reactive oxygen species build excessively and cause cell death. The mechanism of αCT1 on Cx43 is not yet fully realized, however it has been discovered that αCT1 will bind preferentially to ZO-1, which simultaneously reduce hemichannel activity and encourage gap junction binding, as described in Section 1.5.2.[96-97]

1.5.5. Current Methods of Administering Patients with αCT1

Route of administration has an effect on bioavailability of the drug. For topical applications, especially for diabetic and venous leg ulcers, αCT1 is most often applied by dispersing in Granexin gel, which can be applied directly on the wound.[111, 114] When studying effect of αCT1 on prevention of cardiac scar tissue, a methyl cellulose patch containing αCT1 has previously been used in mice.[115] Glioblastoma applications so far have injected αCT1 directly into the tumor site, however this has only been used for animal studies (work not yet published).

Limited encapsulation of αCT1 for controlled release has been conducted. One study encapsulated αCT1 in microparticles in sodium alginate, alginate-poly-l lysine (A-PLL), or alginate-poly-l-ornithine (A-PLO) using an electrospray method. Particles were studied with and without UV crosslinking. However, drug was only released over 48 hours and no cellular or animal studies were conducted.[116] Thus, effectiveness of the particles against glioblastoma applications is unknown. Additionally, for certain long-term applications such as glioblastoma, two days may not be sufficient length of time to be effective for treatment. Therefore a longer-release system is needed for improved delivery of αCT1 over time.

1.6. Statement of Work

This dissertation describes four main projects. First, a CNC sample preparation method was developed in order to avoid use of radioactive stain and glow discharge. Second, a method of quantifying aerosolized rhodamine b-tagged CNCs was developed for eventual monitoring concentrations in CNC production facilities. Third, αCT1 was encapsulated using the double emulsion-solvent evaporation method in order to control the release the drug over several weeks. Finally, in order to increase loading of αCT1 in particles, a flash nanoprecipitation method was used for encapsulation.

References

1. Kessler, R., Engineered Nanoparticles in Consumer Products: Understanding a New Ingredient. *Environmental Health Perspectives* **2011,** *119* (3).
2. Park, J. H.; Mudunkotuwa, I. A.; Mines, L. W.; Anthony, T. R.; Grassian, V. H.; Peters, T. M., A Granular Bed for Use in a Nanoparticle Respiratory Deposition Sampler. *Aerosol Science and Technology* **2015,** *49* (3), 179-187.
3. Moreno-Vega, A.-I.; Gómez-Quintero, T.; Nuñez-Anita, R.-E.; Acosta-Torres, L.-S.; Castaño, V., Polymeric and Ceramic Nanoparticles in Biomedical Applications. *Journal of Nanotechnology* **2012,** *2012*, 1-10.
4. Mallakpour, S.; Behranvand, V., Polymeric nanoparticles: Recent development in synthesis and application. *Express Polymer Letters* **2016,** *10* (11), 895-913.
5. Zhang, Y.; Leu, Y. R.; Aitken, R. J.; Riediker, M., Inventory of Engineered Nanoparticle-Containing Consumer Products Available in the Singapore Retail Market and Likelihood of Release into the Aquatic Environment. *International Journal of Environmental Research and Public Health* **2015,** *12* (8), 8717-43.
6. Hartland, A.; Lead, J. R.; Slaveykova, V. I.; O'Carroll, D.; Valsami-Jones, E., The Environmental Significance of Natural Nanoparticles. *Nature Education Knowledge* **2013,** *4* (8).
7. Muratore, F.; Goñi, M. L.; Serrano, L.; Labidi, J.; Barbosa, S.; Martini, R., Development of Bioactive Paper by Capsaicin Derivative Grafting Onto Cellulose. In *Biopolymer Grafting: Synthesis and Properties*, 2018; pp 199-233.
8. Baptista, A.; Ferreira, I.; Borges, J. P., Cellulose-based Composite Systems for Biomedical Applications. In *Biomass-based Biocomposites*, Thakur, V. K.; Singha, A. S., Eds. Smithers Rapra Technology Ltd: United Kingdom, 2013; pp 47-60.
9. Shanks, R. A., Chemistry and structure of cellulosic fibres as reinforcements in natural fibre composites. In *Natural Fibre Composites*, 2014; pp 66-83.
10. William D. Callister, J., The Structure of Crystalline Solids. In *Material Science and Engineering: An Introduction*, 7 ed.; John Wiley and Sons, Inc.: New York, NY, USA, 2007; pp 38-79.
11. Moon, R. J.; Martini, A.; Nairn, J.; Simonsen, J.; Youngblood, J., Cellulose nanomaterials review: structure, properties and nanocomposites. *Chemical Society Reviews* **2011,** *40* (7), 3941-94.
12. Camarero Espinosa, S.; Kuhnt, T.; Foster, E. J.; Weder, C., Isolation of thermally stable cellulose nanocrystals by phosphoric acid hydrolysis. *Biomacromolecules* **2013,** *14* (4), 1223-30.
13. Habibi, Y.; Chanzy, H.; Vignon, M. R., TEMPO-mediated surface oxidation of cellulose whiskers. *Cellulose* **2006,** *13* (6), 679-687.
14. Dierking, I.; Al-Zangana, S., Lyotropic Liquid Crystal Phases from Anisotropic Nanomaterials. *Nanomaterials* **2017,** *7* (10).
15. Fleming, K.; Gray, D. G.; Matthews, S., Cellulose Crystallites. *Chemistry: A European Journal* **2001,** *7* (9), 1831-1835.
16. Dong, X. M.; Kimura, T.; Revol, J.-F. o.; Gray, D. G., Effects of Ionic Strength on the Isotropic-Chiral Nematic Phase Transition of Suspensions of Cellulose Crystallites. *Langmuir* **1996,** *12*, 2076-2082.
17. Foster, E. J.; Moon, R. J.; Agarwal, U. P.; Bortner, M. J.; Bras, J.; Camarero-Espinosa, S.; Chan, K. J.; Clift, M. J. D.; Cranston, E. D.; Eichhorn, S. J.; Fox, D. M.; Hamad, W. Y.; Heux, L.; Jean, B.; Korey, M.; Nieh, W.; Ong, K. J.; Reid, M. S.; Renneckar, S.; Roberts, R.; Shatkin, J. A.;

Simonsen, J.; Stinson-Bagby, K.; Wanasekara, N.; Youngblood, J., Current characterization methods for cellulose nanomaterials. *Chemical Society Reviews* **2018,** *47* (8), 2609-2679.
18. Salas, C.; Carrillo, C., Dynamic Mechanical Characterization of Cellulose Nanofibril CNF- and Cellulose Nanocrystal CNC-Based Nanocomposites. In *Handbook of Nanocellulose and Cellulose Nanocomposites*, 1st ed.; Kargarzadeh, H.; Ahmad, I.; Thomas, S.; Dufresne, A., Eds. John Wiley & Sons, Incorporated. : 2017; pp 445-479.
19. Dufresne, A., Nanocellulose: a new ageless bionanomaterial. *Materials Today* **2013,** *16* (6), 220-227.
20. Jorfi, M.; Roberts, M. N.; Foster, E. J.; Weder, C., Physiologically responsive, mechanically adaptive bio-nanocomposites for biomedical applications. *ACS Applied Materials & Interfaces* **2013,** *5* (4), 1517-26.
21. Mendez, J.; Annamalai, P. K.; Eichhorn, S. J.; Rusli, R.; Rowan, S. J.; Foster, E. J.; Weder, C., Bioinspired Mechanically Adaptive Polymer Nanocomposites with Water-Activated Shape-Memory Effect. *Macromolecules* **2011,** *44* (17), 6827-6835.
22. Kaushik, M.; Fraschini, C.; Chauve, G.; Putaux, J.-L.; Moores, A., Transmission Electron Microscopy for the Characterization of Cellulose Nanocrystals. In *The Transmission Electron Microscope – Theory and Applications*, Maaz, K., Ed. Intech: 2015.
23. Shatkin, J. A.; Ong, K. J.; Ede, J. D.; Wegner, T. H.; Goergen, M., Toward cellulose nanomaterial commercialization: Knowledge gap analysis for Safety Data Sheets acccording to the globally Harmonized System. *TAPPI Journal* **2016,** *15* (6), 425-437.
24. Materials Safety Data Sheet: Cellulose Nanocrystals. Maine, T. U. o., Ed. USDA FS Forest Products Laboratory.
25. Ong, K. J.; Shatkin, J. A.; Nelson, K.; Ede, J. D.; Retsina, T., Establishing the safety of novel bio-based cellulose nanomaterials for commercialization. *NanoImpact* **2017,** *6*, 19-29.
26. Shatkin, J. A.; Ong, K.; Ede, J., Minimizing Risk: An Overview of Risk Assessment and Risk Management of Nanomaterials. In *Metrology and Standardization for Nanotechnology*, Mansfield, E.; Kaiser, D. L.; Fujita, D.; Voorde, M. V. d., Eds. Wiley-VCH: Weinheim, Germany, 2017.
27. Catalan, J.; Ilves, M.; Jarventaus, H.; Hannukainen, K. S.; Kontturi, E.; Vanhala, E.; Alenius, H.; Savolainen, K. M.; Norppa, H., Genotoxic and immunotoxic effects of cellulose nanocrystals in vitro. *Environmental and Molecular Mutagenesis* **2015,** *56* (2), 171-82.
28. Shatkin, J. A.; Kim, B., Cellulose nanomaterials: life cycle risk assessment, and environmental health and safety roadmap. *Environmental Science: Nano* **2015,** *2* (5), 477-499.
29. Roberts, R.; Gettz, K.; Stebounova, L. V.; Shatkin, J. A.; Peters, T.; Foster, E. J., Collection of airborne ultrafine cellulose nanocrystals by impinger with an efficiency mimicking deposition in the human respiratory system. *Journal of Occupational and Environmental Hygiene* **2019**.
30. Cena, L. G.; Anthony, T. R.; Peters, T. M., A personal nanoparticle respiratory deposition (NRD) sampler. *Environmental Science & Technology* **2011,** *45* (15), 6483-90.
31. Asbestos Sampling. Environmental Protectional Agency: 1994.
32. Cena, L. G.; Anthony, R.; Peters, T. M., A Personal Nanoparticle Respiratory Deposition (NRD) Sampler. *Environmental Science & Technology* **2011,** *45*, 6483-6490.
33. Zefon International Standard Midget Impinger. (accessed November 14).
34. Jessy, R. S.; Ibrahim, M. H., Biodegradability and Biocompatibility of Polymers with Emphasis on Bone Scaffolding: a Brief Review. *International Journal of Scientific and Research Publications* **2014,** *4* (7), 1-3.

35. Kamaly, N.; Yameen, B.; Wu, J.; Farokhzad, O. C., Degradable Controlled-Release Polymers and Polymeric Nanoparticles: Mechanisms of Controlling Drug Release. *Chemical Reviews* **2016,** *116* (4), 2602-63.
36. Bala, I.; Sarita Hariharan; Kumar, M. R., PLGA Nanoparticles in Drug Delivery: The State of the Art. *Critical Reviews™ in Therapeutic Drug Carrier Systems* **2004,** *21* (5), 387-422.
37. Divya, K.; Vijayan, S.; George, T. K.; Jisha, M. S., Antimicrobial properties of chitosan nanoparticles: Mode of action and factors affecting activity. *Fibers and Polymers* **2017,** *18* (2), 221-230.
38. Hassan, M. M., Binding of a quaternary ammonium polymer-grafted-chitosan onto a chemically modified wool fabric surface: assessment of mechanical, antibacterial and antifungal properties. *RSC Advances* **2015,** *5* (45), 35497-35505.
39. Jia, R.; Jiang, H.; Jin, M.; Wang, X.; Huang, J., Silver/chitosan-based Janus particles: Synthesis, characterization, and assessment of antimicrobial activity in vivo and vitro. *Food Research International* **2015,** *78*, 433-441.
40. Park, B. J.; Brugarolas, T.; Lee, D., Janus particles at an oil–water interface. *Soft Matter* **2011,** *7* (14).
41. Cheng, J.; Teply, B. A.; Sherifi, I.; Sung, J.; Luther, G.; Gu, F. X.; Levy-Nissenbaum, E.; Radovic-Moreno, A. F.; Langer, R.; Farokhzad, O. C., Formulation of functionalized PLGA-PEG nanoparticles for in vivo targeted drug delivery. *Biomaterials* **2007,** *28* (5), 869-76.
42. Jain, G. K.; Pathan, S. A.; Akhter, S.; Jayabalan, N.; Talegaonkar, S.; Khar, R. K.; Ahmad, F. J., Microscopic and spectroscopic evaluation of novel PLGA-chitosan Nanoplexes as an ocular delivery system. *Colloids and Surfaces B: Biointerfaces* **2011,** *82* (2), 397-403.
43. Chen, X.; Liu, L.; Jiang, C., Charge-reversal nanoparticles: novel targeted drug delivery carriers. *Acta Pharmaceutica Sinica B* **2016,** *6* (4), 261-7.
44. Jain, R. A., The manufacturing techniques of various drug loaded biodegradable poly(lactide-co-glycolide) (PLGA) devices. *Biomaterials* **2000,** *21*, 16.
45. Lu, J. M.; Wang, X.; Marin-Muller, C.; Wang, H.; Lin, P. H.; Yao, Q.; Chen, C., Current advances in research and clinical applications of PLGA-based nanotechnology. *Expert Review of Molecular Diagnostics* **2009,** *9* (4), 325-41.
46. Avgoustakis, K., Polylactic-Co-Glycolic Acid (PLGA). In *Encyclopedia of Biomaterials and Biomedical Engineering*, Taylor & Francis: 2005; pp 1-11.
47. Wang, Y.; Qu, W.; Choi, S. H. FDA's Regulatory Science Program for Generic PLA/PLGA-Based Drug Products. https://www.americanpharmaceuticalreview.com/Featured-Articles/188841-FDA-s-Regulatory-Science-Program-for-Generic-PLA-PLGA-Based-Drug-Products/ (accessed September 9).
48. Poly(D,L-lactide-co-glycolide). www.sigmaaldrich.com (accessed November 15).
49. Makadia, H. K.; Siegel, S. J., Poly Lactic-co-Glycolic Acid (PLGA) as Biodegradable Controlled Drug Delivery Carrier. *Polymers* **2011,** *3* (3), 1377-1397.
50. Ribeiro, C.; Sencadas, V.; Costa, C. M.; Gómez Ribelles, J. L.; Lanceros-Méndez, S., Tailoring the morphology and crystallinity of poly(L-lactide acid) electrospun membranes. *Science and Technology of Advanced Materials* **2011,** *12* (1).
51. Phua, K. K. L.; Roberts, E. R. H.; Leong, K. W., Degradable Polymers. *Comprehensive Biomaterials* **2011,** *1*, 381-415.
52. O'Donnell, P. B.; McGinity, J. W., Preparation of microspheres by the solvent evaporation technique. *Advanced Drug Delivery Reviews* **1997,** *28*, 25-42.

53. 510(k) Clearances. https://www.fda.gov/medicaldevices/productsandmedicalprocedures/deviceapprovalsandclearances/510kclearances/). (accessed 11/2/18).
54. Danhier, F.; Ansorena, E.; Silva, J. M.; Coco, R.; Le Breton, A.; Preat, V., PLGA-based nanoparticles: an overview of biomedical applications. *Journal of Controlled Release* **2012,** *161* (2), 505-22.
55. Paolicelli, P.; Prego, C.; Sanchez, A.; Alonso, M. J., Surfacemodified PLGAbased Nanoparticles that can Efficiently Associate and Deliver Viruslike Particles. *Nanomedicine* **2010**.
56. Xiong, M. H.; Bao, Y.; Yang, X. Z.; Zhu, Y. H.; Wang, J., Delivery of antibiotics with polymeric particles. *Advanced Drug Delivery Reviews* **2014,** *78*, 63-76.
57. Miladi, K.; Sfar, S.; Fessi, H.; Elaissari, A., Nanoprecipitation Process: From Particle Preparation to In Vivo Applications. In *Polymer Nanoparticles for Nanomedicines*, 2016; pp 17-53.
58. Joshi, J. R.; Patel, R. P., Role of Biodegradable Polymers in Drug Delivery. *International Journal of Current Pharmaceutical Research* **2012,** *4* (4), 74-81.
59. Bilati, U.; Allemann, E.; Doelker, E., Development of a nanoprecipitation method intended for the entrapment of hydrophilic drugs into nanoparticles. *European Journal of Pharmaceutical Science* **2005,** *24* (1), 67-75.
60. Astete, C. E.; Sabliov, C., Synthesis and characterization of PLGA nanoparticles. *Journal of Biomaterials Science, Polymer Edition* **2006,** *17* (3), 44.
61. Carrasquillo, K. G.; Stanley, A. M.; Aponte-Carro, J. C.; Jesus, P. D.; Costantino, H. R.; Bosques, C. J.; Griebenow, K., Non-aqueous encapsulation of excipient-stabilized spray-freeze dried BSA into poly(lactide-co-glycolide) microspheres results in release of native protein. *Journal of Controlled Release* **2001,** *76*, 199–208.
62. Wang, Y.; Zhang, Y.; Wang, B.; Cao, Y.; Yu, Q.; Yin, T., Fabrication of core–shell micro/nanoparticles for programmable dual drug release by emulsion electrospraying. *Journal of Nanoparticle Research* **2013,** *15* (6).
63. Murakami, H.; Kobayashi, M.; Takeuchi, H.; Kawashima, Y., Preparation of poly(DL-lactide-co-glycolide) nanoparticles by modified spontaneous emulsification solvent diffusion method. *International Journal of Pharmaceutics* **1999,** *187*, 10.
64. Hung, L. H.; Teh, S. Y.; Jester, J.; Lee, A. P., PLGA micro/nanosphere synthesis by droplet microfluidic solvent evaporation and extraction approaches. *Lab Chip* **2010,** *10* (14), 1820-5.
65. Akagi, T.; Baba, M.; Akashi, M., Biodegradable Nanoparticles as Vaccine Adjuvants and Delivery Systems: Regulation of Immune Responses by Nanoparticle-Based Vaccine. **2011,** *247*, 31-64.
66. Budhian, A.; Siegel, S. J.; Winey, K. I., Haloperidol-loaded PLGA nanoparticles: systematic study of particle size and drug content. *International Journal of Pharmaceutics* **2007,** *336* (2), 367-75.
67. Chitkara, D.; Kumar, N., BSA-PLGA-based core-shell nanoparticles as carrier system for water-soluble drugs. *Pharmaceutical Research* **2013,** *30* (9), 2396-409.
68. Mu, L.; Feng, S.-S., PLGA/TPGS Nanoparticles for Controlled Release of Paclitaxel: Effects of the Emulsifier and Drug Loading Ratio. *Pharmaceutical Research* **2003,** *20* (11), 9.
69. Chen, Y.; Wang, F.; Benson, H. A., Effect of formulation factors on incorporation of the hydrophilic peptide dalargin into PLGA and mPEG-PLGA nanoparticles. *Biopolymers* **2008,** *90* (5), 644-50.

70. Govender, T.; Stolnik, S.; Garnett, M. C.; Illum, L.; Davis, S. S., PLGA nanoparticles prepared by nanoprecipitation: drug loading and release studies of a water soluble drug. *Journal of Controlled Release* **1999,** *57*, 171-185.
71. Lee, C.; Choi, J. S.; Kim, I.; Oh, K. T.; Lee, E. S.; Park, E. S.; Lee, K. C.; Youn, Y. S., Long-acting inhalable chitosan-coated poly(lactic-co-glycolic acid) nanoparticles containing hydrophobically modified exendin-4 for treating type 2 diabetes. *International Journal of Nanomedicine* **2013,** *8*, 2975-83.
72. Soppimath, K. S.; Aminabhavi, T. M.; Kulkarni, A. R.; Rudzinski, W. E., Biodegradable polymeric nanoparticles as drug delivery devices. *Journal of Controlled Release* **2001,** *70*, 20.
73. Panyam, J.; Williams, D.; Dash, A.; Leslie-Pelecky, D.; Labhasetwar, V., Solid-state solubility influences encapsulation and release of hydrophobic drugs from PLGA/PLA nanoparticles. *Journal of Pharmaceutical Sciences* **2004,** *93* (7), 1804-14.
74. Fredenberg, S.; Wahlgren, M.; Reslow, M.; Axelsson, A., The mechanisms of drug release in poly(lactic-co-glycolic acid)-based drug delivery systems--a review. *Int J Pharm* **2011,** *415* (1-2), 34-52.
75. Huang, X.; Brazel, C. S., On the importance and mechanisms of burst release in matrix-controlled drug delivery systems. *Journal of Controlled Release* **2001,** *73*, 121-136.
76. De Melo, N. F.; De Araujo, D. R.; Grillo, R.; Moraes, C. M.; De Matos, A. P.; de Paula, E.; Rosa, A. H.; Fraceto, L. F., Benzocaine-loaded polymeric nanocapsules: study of the anesthetic activities. *Journal of Pharmaceutical Sciences* **2012,** *101* (3), 1157-65.
77. Cartiera, M. S.; Ferreira, E. C.; Caputo, C.; Egan, M. E.; Caplan, M. J.; Saltzman, W. M., Partial correction of cystic fibrosis defects with PLGA nanoparticles encapsulating curcumin. *Molecular Pharmacology* **2010,** *7* (1), 86-93.
78. Dalwadi, G.; Sunderland, B., An ion pairing approach to increase the loading of hydrophilic and lipophilic drugs into PEGylated PLGA nanoparticles. *European Journal of Pharmaceutics and Biopharmaceutics* **2009,** *71* (2), 231-42.
79. Manoharan, C.; Singh, J., Insulin loaded PLGA microspheres: effect of zinc salts on encapsulation, release, and stability. *Journal of Pharmaceutical Sciences* **2009,** *98* (2), 529-42.
80. Shakeri, S.; Roghanian, R.; Emtiazi, G.; Errico, C.; Chiellini, F.; Chiellini, E., Preparation of protein-loaded PLGA-PVP blend nanoparticles by nanoprecipitation method: entrapment, Initial burst and drug release kinetic studies. *Nanomedicine Journal* **2015,** *2* (3), 12.
81. Hu, S.; Zhang, Y., Endostar-loaded PEG-PLGA nanoparticles: in vitro and in vivo evaluation. *International Journal of Nanomedicine* **2010,** *5*, 1039-48.
82. Morales-Cruz, M.; Flores-Fernandez, G. M.; Morales-Cruz, M.; Orellano, E. A.; Rodriguez-Martinez, J. A.; Ruiz, M.; Griebenow, K., Two-step nanoprecipitation for the production of protein-loaded PLGA nanospheres. *Results in Pharma Sciences* **2012,** *2*, 79-85.
83. Dinda, S. C., Bioaccumulation and Toxic Profiling of Nanostructured Particles and Materials. In *Unraveling the Safety Profile of Nanoscale Particles and Materials - From Biomedical to Environmental Applications*, 2018.
84. Mura, S.; Hillaireau, H.; Nicolas, J.; Le Droumaguet, B.; Gueutin, C.; Zanna, S.; Tsapis, N.; Fattal, E., Influence of surface charge on the potential toxicity of PLGA nanoparticles towards Calu-3 cells. *International Journal of Nanomedicine* **2011,** *6*, 2591-605.
85. Frohlich, E., The role of surface charge in cellular uptake and cytotoxicity of medical nanoparticles. *Int J Nanomedicine* **2012,** *7*, 5577-91.

86. Grabowski, N.; Hillaireau, H.; Vergnaud, J.; Santiago, L. A.; Kerdine-Romer, S.; Pallardy, M.; Tsapis, N.; Fattal, E., Toxicity of surface-modified PLGA nanoparticles toward lung alveolar epithelial cells. *Int J Pharm* **2013,** *454* (2), 686-94.
87. Grabowski, N.; Hillaireau, H.; Vergnaud, J.; Tsapis, N.; Pallardy, M.; Kerdine-Romer, S.; Fattal, E., Surface coating mediates the toxicity of polymeric nanoparticles towards human-like macrophages. *International Journal of Pharmaceutics* **2015,** *482* (1-2), 75-83.
88. Singh, R. P.; Ramarao, P., Accumulated polymer degradation products as effector molecules in cytotoxicity of polymeric nanoparticles. *Toxicological Sciences* **2013,** *136* (1), 131-43.
89. Zhang, B.; Sai Lung, P.; Zhao, S.; Chu, Z.; Chrzanowski, W.; Li, Q., Shape dependent cytotoxicity of PLGA-PEG nanoparticles on human cells. *Scientific Reports* **2017,** *7* (1), 7315.
90. Platel, A.; Carpentier, R.; Becart, E.; Mordacq, G.; Betbeder, D.; Nesslany, F., Influence of the surface charge of PLGA nanoparticles on their in vitro genotoxicity, cytotoxicity, ROS production and endocytosis. *Journal of Applied Toxicology* **2016,** *36* (3), 434-44.
91. Navarro, S. M.; Darensbourg, C.; Cross, L.; Stout, R.; Coulon, D.; Astete, C. E.; Morgan, T.; Sabliov, C. M., Biodistribution of PLGA and PLGA/chitosan nanoparticles after repeat-dose oral delivery in F344 rats for 7 days. *Therapeutic Delivery* **2014,** *5* (11), 1191-201.
92. Stevanovic, M.; Maksin, T.; Petkovic, J.; Filipic, M.; Uskokovic, D., An innovative, quick and convenient labeling method for the investigation of pharmacological behavior and the metabolism of poly(DL-lactide-co-glycolide) nanospheres. *Nanotechnology* **2009,** *20* (33), 335102.
93. Mathew, A.; Fukuda, T.; Nagaoka, Y.; Hasumura, T.; Morimoto, H.; Yoshida, Y.; Maekawa, T.; Venugopal, K.; Kumar, D. S., Curcumin loaded-PLGA nanoparticles conjugated with Tet-1 peptide for potential use in Alzheimer's disease. *PLoS One* **2012,** *7* (3), e32616.
94. Vibe, C. B.; Fenaroli, F.; Pires, D.; Wilson, S. R.; Bogoeva, V.; Kalluru, R.; Speth, M.; Anes, E.; Griffiths, G.; Hildahl, J., Thioridazine in PLGA nanoparticles reduces toxicity and improves rifampicin therapy against mycobacterial infection in zebrafish. *Nanotoxicology* **2016,** *10* (6), 680-8.
95. Hung, H. I.; Klein, O. J.; Peterson, S. W.; Rokosh, S. R.; Osseiran, S.; Nowell, N. H.; Evans, C. L., PLGA nanoparticle encapsulation reduces toxicity while retaining the therapeutic efficacy of EtNBS-PDT in vitro. *Scientific Reports* **2016,** *6*, 33234.
96. Grek, C. L.; Rhett, J. M.; Ghatnekar, G. S., Cardiac to cancer: connecting connexins to clinical opportunity. *FEBS Letters* **2014,** *588* (8), 1349-64.
97. Murphy, S. F.; Varghese, R. T.; Lamouille, S.; Guo, S.; Pridham, K. J.; Kanabur, P.; Osimani, A. M.; Sharma, S.; Jourdan, J.; Rodgers, C. M.; Simonds, G. R.; Gourdie, R. G.; Sheng, Z., Connexin 43 Inhibition Sensitizes Chemoresistant Glioblastoma Cells to Temozolomide. *Cancer Research* **2016,** *76* (1), 139-49.
98. Bosco, D.; Haefliger, J. A.; Meda, P., Connexins: key mediators of endocrine function. *Physiological Reviews* **2011,** *91* (4), 1393-445.
99. Lodish, H.; Berk, A.; Zipursky, S. L.; Matsudaira, P.; Baltimore, D.; Darnell., J., Membrane Proteins. In *Molecular Cell Biology*, 4th ed.; W. H. Freeman and Company: New York, 2000.
100. Belousov, A. B.; Fontes, J. D.; Freitas-Andrade, M.; Naus, C. C., Gap junctions and hemichannels: communicating cell death in neurodevelopment and disease. *BMC Cell Biology* **2017,** *18* (Suppl 1), 4.

101. Munoz, J. L.; Rodriguez-Cruz, V.; Greco, S. J.; Ramkissoon, S. H.; Ligon, K. L.; Rameshwar, P., Temozolomide resistance in glioblastoma cells occurs partly through epidermal growth factor receptor-mediated induction of connexin 43. *Cell Death & Disease* **2014,** *5*, e1145.
102. Huang, R.-P.; Hossain, M. Z.; Huang, R.; Gano, J.; Fan, Y.; Boynton, A. L., Connexin 43 (Cx43) Enhances Chemotherapy-Induced Apoptosis in Human Glioblastoma Cells. *International Journal of Cancer* **2001,** *92*, 130-138.
103. Elias, L. A.; Kriegstein, A. R., Gap junctions: multifaceted regulators of embryonic cortical development. *Trends Neurosci* **2008,** *31* (5), 243-50.
104. Glioblastoma (GBM). https://www.abta.org/tumor_types/glioblastoma-gbm/ (accessed 10/29/2018).
105. Glioblastoma and Malignant Astrocytoma. Association, A. B. T., Ed. American Brain Tumor Association: 2017; Vol. FGS0517.
106. Ramirez, Y. P.; Weatherbee, J. L.; Wheelhouse, R. T.; Ross, A. H., Glioblastoma multiforme therapy and mechanisms of resistance. *Pharmaceuticals* **2013,** *6* (12), 1475-506.
107. Bobo, D.; Robinson, K. J.; Islam, J.; Thurecht, K. J.; Corrie, S. R., Nanoparticle-Based Medicines: A Review of FDA-Approved Materials and Clinical Trials to Date. *Pharmaceutical Research* **2016,** *33* (10), 2373-87.
108. How Optune works. https://www.optune.com/discover-optune/how-optune-works (accessed 10/29/18).
109. Walczak, C. E.; Heald, R., Chapter Three - Mechanisms of Mitotic Spindle Assembly and Function. In *International Review of Cytology*, Jeon, K. W., Ed. Academic Press: 2008; Vol. 265, pp 111-158.
110. Huang, N. F.; Lee, R. J.; Li, S., Engineering of aligned skeletal muscle by micropatterning. *American Journal of Translational Research* **2010,** *2* (1), 12.
111. Grek, C. L.; Prasad, G. M.; Viswanathan, V.; Armstrong, D. G.; Gourdie, R. G.; Ghatnekar, G. S., Topical administration of a connexin43-based peptide augments healing of chronic neuropathic diabetic foot ulcers: A multicenter, randomized trial. *Wound Repair and Regeneration* **2015,** *23* (2), 203-12.
112. Gielen, P. R.; Aftab, Q.; Ma, N.; Chen, V. C.; Hong, X.; Lozinsky, S.; Naus, C. C.; Sin, W. C., Connexin43 confers Temozolomide resistance in human glioma cells by modulating the mitochondrial apoptosis pathway. *Neuropharmacology* **2013,** *75*, 539-48.
113. Zhao, Y.; Hu, X.; Liu, Y.; Dong, S.; Wen, Z.; He, W.; Zhang, S.; Huang, Q.; Shi, M., ROS signaling under metabolic stress: cross-talk between AMPK and AKT pathway. *Molecular Cancer* **2017,** *16* (1), 79.
114. Ghatnekar, G. S. A Study of Granexin Gel to Treat Diabetic Foot Ulcer. clinicaltrials.gov (accessed 5/20/2018).
115. O'Quinn, M. P.; Palatinus, J. A.; Harris, B. S.; Hewett, K. W.; Gourdie, R. G., A peptide mimetic of the connexin43 carboxyl terminus reduces gap junction remodeling and induced arrhythmia following ventricular injury. *Circulation Research* **2011,** *108* (6), 704-15.
116. Moore, K.; Amos, J.; Davis, J.; Gourdie, R.; Potts, J. D., Characterization of polymeric microcapsules containing a low molecular weight peptide for controlled release. *Microscopy and Microanalysis* **2013,** *19* (1), 213-26.

Chapter 2

Objectives and Outline

2.1. Objectives

Nanoparticles have the potential for widespread improvements in everyday products in a variety of disciplines. With increased prevalence of polymeric nanoparticles in our everyday lives, characterization of isolated and synthesized particles becomes more important to ensure quality and safety and commercial products. The overall objective of this dissertation is to develop methods of nanoparticle characterization that may be accessible to a broader audience, then use those techniques on synthesized nanoparticles that encapsulate a peptide for glioblastoma applications. Specifically, the goals of the dissertation are:

1. **Develop an electron microscopy sample preparation method** for CNCs that avoids use of a radioactive stain and a glow discharge device. This will allow laboratories without the facilities to handle radioactive material or without the specialized equipment to be able to prepare TEM samples for characterization of CNCs. The ability to accurately characterize these nanoparticles will increase the reproducibility of any work involving CNCs.
2. **Develop a quantification method for monitoring concentration of CNCs in air** for health and safety precautions in production facilities. Toxicity of CNCs is not yet fully understood, and the ability to track CNC concentration in production facilities will help ensure the safety of plant workers.
3. **Control the release of a peptide drug from PLGA nanoparticles** in order to facilitate long-term delivery for treatment of glioblastoma. This will be essential for the continual treatment of this deadly brain cancer.
4. **Improve drug loading of αCT1 in PLGA nanoparticles** in order to improve efficacy and longevity in the body. Higher drug loading increases the practicality of using nanoparticles for drug delivery, and may lead to product realization.

2.2. Dissertation Outline

This dissertation is composed of two peer-reviewed publications, one manuscript currently in review for publication, and one manuscript to be submitted for publication, constituting four research chapters.

Chapter 1: *Introduction*. This chapter introduces the topics of discussion and provides background information for the following research chapters.

Chapter 2: *Objectives and Outline*. The objectives and outline give a brief overview of the contents of the thesis and its goals.

Chapter 3: *Effective Cellulose Nanocrystal Imaging using Transmission Electron Microscopy.* This chapter developed a reliable way to image CNCs in TEM using the dispersant bovine serum albumin and non-radioactive stain (vanadium-based Nanovan®). Dispersion and visibility of CNCs under TEM is explored. This work was published in *Carbohydrate Polymers.*

Chapter 4: *Collection of airborne ultrafine cellulose nanocrystals by impinger with an efficiency mimicking deposition in the human respiratory system*. In this chapter, CNCs labeled with rhodamine B (RhB) were aerosolized and collected in an impinger in order to develop a method to quantify CNCs in air. This was recently accepted in *Journal of Environmental and Occupational Hygiene* and is expected to be published in February 2019.

Chapter 5: *Development of PLGA nanoparticles for sustained release of a Connexin43 mimetic peptide to target glioblastoma cells*. This chapter explores using emulsion techniques to encapsulate αCT1 in PLGA nanoparticles for delivery to glioblastoma cells. Particle size was of particular interest due to application needs in the brain. However, drug loading was low in the particles. This work has been submitted to *Materials Science and Engineering: C* and is currently under review.

Chapter 6: *Flash nanoprecipitation method for increased loading of a Connexin43 mimetic peptide-loaded PLGA nanoparticle to target glioblastoma cells*. In this chapter, the challenge of low drug loading was addressed by using flash nanoprecipitation for encapsulation of αCT1. In order to further increase loading, several parameters of this method were explored for effect on loading. Release studies using the optimized particles were also conducted. This chapter is in progress for submission to *Nanotechnology* and is expected to be submitted for publication by January 2019.

Chapter 7. *Concluding Remarks*. This chapter summarizes the presented contributions and provides an outlook for future work to develop improved characterization and synthesis techniques for polymeric nanoparticles.

Chapter 3

Effective Cellulose Nanocrystal Imaging using Transmission Electron Microscopy

Characterization of CNCs usually includes the need for imaging in order to confirm aspect ratio and determine amount of agglomeration. Imaging almost always uses TEM for CNCs due to their size and shape. However, in order to accurately measure particle dimensions, CNCs need to be dispersed and visible against the similarly-electron-dense sample grid. This chapter provided a method for our lab to prepare TEM samples of CNCs without the use of radioactive staining or use of glow discharge device, to both of which our lab had limited access. Further chapters using TEM prepared samples used the developed method.

In this chapter, all data were collected and analyzed equally between myself and Ms. Kelly Stinson-Bagby. The chapter was drafted equally between myself and Ms. Stinson-Bagby, and edited by my academic advisor, Dr. E. Johan Foster. This chapter is reprinted as it appears in Carbohydrate Polymers, with permission from Elsevier

Effective cellulose nanocrystal imaging using transmission electron microscopy
Rose Roberts,* Kelly L. Stinson-Bagby,* and E. Johan Foster
Carbohydrate Polymers, 2018, 186, pp. 429-438.
DOI: 10.1016/j.carbpol.2018.01.054

*Authors contributed equally to the paper.

Carbohydrate Polymers 186 (2018) 429–438

Contents lists available at ScienceDirect

Carbohydrate Polymers

journal homepage: www.elsevier.com/locate/carbpol

Effective cellulose nanocrystal imaging using transmission electron microscopy

Kelly L. Stinson-Bagby[1], Rose Roberts[1], E. Johan Foster[*]

Virginia Tech, Department of Materials Science and Engineering, Macromolecules Innovation Institute (MII), 213 Holden Hall, 445 Old Turner Street, Blacksburg, VA, 24061, USA

ARTICLE INFO

Keywords:
Cellulose nanocrystals
Transmission electron microscopy
Stain
Dispersion
Contrast

ABSTRACT

Characterization of cellulose nanocrystals (CNCs) is often complex and tedious. With their increased use for biological materials, polymer reinforcing agents, and other applications, better characterization methods of CNCs are needed to ensure product quality. However, because of their small size, hydrogen bonding, and low electron density, individual CNCs are difficult to image with high resolution and magnification using electron microscopy. Methods to help counter these challenges include staining for increased contrast and techniques to increase dispersion. This work tested several stains, dispersing agents, and sample supports to find a consistent method of individualizing CNCs and providing good contrast for imaging in transmission electron microscopy (TEM). The most consistent method found uses a low concentration of CNCs, bovine serum albumin as a dispersing agent, and Nanovan® as the contrasting stain on a silicon monoxide-coated Formvar TEM grid.

1. Introduction

Cellulose nanocrystals (CNCs) are derived from the crystalline regions found in cellulose (Habibi, Lucia, & Rojas, 2010; Kaushik, Fraschini, Chauve, Putaux, & Moores, 2015). Their size can vary greatly depending on source material and extraction method; hence, accurate characterization of individual crystals is important (Habibi et al., 2010). Transmission electron microscopy (TEM) is a well-used method for imaging CNCs but comes with major challenges including the sample preparation factors dispersibility and contrast (Kaushik et al., 2015).

Dispersibility issues arise due to the attractive forces between the CNCs. The crystalline regions of cellulose are held together through inter- and intra-molecular hydrogen bonds and van der Waals forces which are difficult to break (Kaushik et al., 2015; Moon, Martini, Nairn, Simonsen, & Youngblood, 2011). Hydrogen bond stacking and van der Waals forces can hold CNCs together in bundles, especially during the drying on a surface such as a TEM grid, which is difficult to avoid if no other method than sonication is being used for dispersion (Espinosa, Kuhnt, Foster, & Weder, 2013; Hosseinidoust, Alam, Sim, Tufenkji, & van de Ven, 2015; Kaushik et al., 2015; Postek et al., 2011; Qua, Hornsby, Sharma, & Lyons, 2011). Other methods to prevent agglomeration during drying involve altering the pH to allow electrostatic forces to disperse the CNCs or by adding an adsorbing dispersion agent such as bovine serum albumin (BSA) to sterically hinder agglomeration during drying (Kaushik, Chen, Van de Ven, & Moores, 2014; Michen et al., 2015).

The contrast in TEM is affected by electron density of the material and its size. Cellulose is made of mostly carbon, so its electron density is low which limits contrast (Kaushik et al., 2014; Kaushik et al., 2015). CNCs also average between 5 and 20 nm in diameter, which is not much depth for transmitting electrons to interact with the sample. In addition, TEM sample substrates are typically carbon-based so both the sample and the substrate will transmit to the detector similar electron outputs, meaning the contrast between sample and substrate is low (Habibi et al., 2010). A stain containing a heavy metal salt, such as uranyl acetate, is often used to increase contrast. Uranyl acetate is one of the most widely used heavy metal negative stains, but it is relatively expensive, toxic, and radioactive, which introduces restrictions on its use (Ikeda, Inoue, Kanematsu, Horiuchi, & Park, 2011; Kaushik et al., 2014; Kaushik et al., 2015). Other stains are available but have not been widely explored. Though staining benefits imaging contrast other imaging side effects can occur, including aggregation of the sample during drying and measurement inaccuracy during image analysis (Kaushik et al., 2014).

Table 1 outlines various methods used by other researchers for TEM imaging of CNCs, which influenced the work discussed in this paper. In general, lower magnifications produce higher contrast, but are not at an

* Corresponding author.
E-mail addresses: kstinson@vt.edu (K.L. Stinson-Bagby), rose64@vt.edu (R. Roberts), johanf@vt.edu (E.J. Foster).
[1] Authors that contributed equally to the paper.

https://doi.org/10.1016/j.carbpol.2018.01.054
Received 10 November 2017; Received in revised form 16 January 2018; Accepted 17 January 2018
Available online 31 January 2018
0144-8617/

Table 1
TEM imaging techniques previously used for CNCs (key below).

Source	Dispersion Method (Dispersant), concentration	Stain	Grid Type	Grid Drying Method	Voltage (kV)	Mag Acceptable for Measurements	Contrast	Dispersion	Stain Comments	Reference
W	US, pH3 (W), 0.1–0.3 w/w%	UA or none	SiO, C, F	–	L or H	G	G	G	NA	Kaushik et al. (2014)
Cotton	(W), 1–2%	UA	C	–	L	G	G	G	S, T	Montanari, Roumani, Heux, & Vignon (2005)
Flax	(W)	1% UA**	CC	Rm Temp	M	G	M	M	S	Qua et al. (2011)
Wood	(CM), 5 mg/mL	UA***	Cu	Overnight	M	G	M	P	S, T, C	Zhou et al. (2015)
Wood	(W), 0.1 w/w%	2% UA*	GC	–	M	G	P	G	T	Hosseinidoust et al. (2015)
Cotton	US (W)	2% AM	Cu	–	L	G	P	G	T	Choi (2006)
Wood	US or S (W), 0.01 wt%	2% UA	F	–	M	M	G	M	S, C	de Paula, Mano, Duek, & Pereira (2015)
Tunicate, Cotton	S (W), 0.1 mg/mL	–	CC	70C 2 h	L	M	G	M	S, C	Jorfi, Roberts, Foster, & Weder (2013)
Cassava Bagasse+	HV	1% AM	Cu	Rm Temp	M	M	G	M	T	Wicaksono, Syamsu, Yuliasih, & Nasir (2013)
Tunicate	(W), 0.1 mg/mL	–	CC	70C 2 h	L	P	G	M	NA	Potter et al. (2014)
Tunicate	BS (DMF), 0.1 mg/mL	None	CC	70C 4 h	L	P	G	M	S	Biyani (2014)
Wood	(W), 0.1 mg/mL	–	CC	70C 1 h	L	P	G	M	S, C	Espinosa et al. (2013)
–	US (CF), 1 w%	2% UA#	CC	–	H	G	G	M	S, C	Kvien, Tanem, & Oksman* (2005)

Key for Table 1

Dispersion		Stain		Grid Type		Voltage	
> Mechanical Dispersion		UA	uranyl acetate	Cu	Copper	H	High (150–200 kV)
S	sonicate (general)	AM	ammonium molybdate	C	Carbon	M	Medium (100–120 kV)
BS	bath sonicator			CC	Carbon Coated	L	Low (60–80 kV)
US	ultrasonicator			F	Formvar		
HV	high velocity mixer			GC	Glow discharged Carbon		
pH3	water adjusted to pH 3 using HCl			SC	SiO coated		
> (Solution Medium)							
(W)	water						
(DMF)	DMF						
(CM)	cell culture media (Mueller-Hinton)						
(CF)	chloroform						

Mag Acceptable		Contrast and Dispersion		Stain related	
G	Mag optimal range (< 300 nm scale)	G	Good	C	crystals
M	Mag acceptable with additional contrast strategies like staining (> 300 nm, < 1 μm scale)	M	Moderate	S	splotchiness/excess stain not targeted onto CNCs
P	Mag too high (> 1 μm scale)	P	Poor	T	

– No information.
+ Nanofibrils, not cellulose nanocrystals.
* Drop of stain on for 5 min, washed 3 x by adding a drop of water for 10 s each (rinse method).
** Drop of stain on for 30 s, then immersed in water (dunk method).
*** Dipped in glutaraldehyde before dipped in UA (study with E.coli).
# CNC solution allowed to drip through the grid, then the grid floated in UA solution for 3 min.

acceptable magnification to accurately measure the aspect ratio of individual crystals. When the magnification is high, contrast decreases and makes it difficult to determine the precise location of the edges of the CNCs. Staining can help to increase contrast at high magnification and dispersion can be enhanced through sonication and solvent selection to break apart the CNC bundles for isolation of individual crystals. There have been several examples in literature that have been successful in producing images of dispersed CNCs with very clear images (Elazzouzi-Hafraoui et al., 2008). However, these examples have used the radioactive, positively charged stain uranyl acetate, or a processing technique called glow discharge, or both (see Table 1). Glow discharge is used to clean the TEM grid, but it is also used as part of various processes to create a positively charged surface on the grid. This positive charge can help attract the CNCs while also preventing agglomeration during drying since the CNCs have a slight negative charge (Ranby, 1951) but finding positively-charged TEM grids for purchase can be elusive. Additionally, if a glow discharge device is inaccessible or radioactive materials and waste handling is unavailable, it can be difficult to achieve high quality CNCs images for characterization purposes.

In this study, we show that by combining and testing previously used methods and materials, high-contrast TEM images of individualized (well-dispersed) CNCs is possible for characterization purposes without using radioactive stains or altering grid surface properties. Several methods of CNC sample preparation for TEM, sample application to the TEM grid, grid type, stain type, and various dispersion methods were explored. Freeze-dried and never-dried source materials were used as well as CNCs modified by tagging with rhodamine B or oxidizing with TEMPO. A troubleshooting table is also provided for identifying and correcting TEM artifacts during imaging.

2. Materials and equipment

2.1. Materials

Source cellulose nanocrystal (CNC) materials were obtained from US Forest Service as a freeze-dried product (sulfuric acid hydrolysis, from wood pulp; 0.94 wt% sulfur content on dry CNCs) and from the University of Maine as an 11.8 wt% CNC aqueous gel (sulfuric acid hydrolysis, from wood pulp; 1.00 wt% sulfur content on dry CNCs). PELCO® TEM 200 mesh copper grids with Formvar/carbon or Formvar/silicon monoxide support films were obtained from Ted Pella, Inc. TEMPO (MW 156.25), rhodamine b, bovine serum albumin (BSA), hydrochloric acid (HCl), iodine, and ammonium molybdate were obtained from Sigma Aldrich. Uranyl acetate was obtained from SPI Supplies and NanoVan® (methylamine vanadate) was obtained from Nanoprobes, Inc.

2.2. Equipment

The imaging of CNCs was conducted on the JEOL 2100 TEM, field thermionic emission analytical electron microscope, located at the Nanoscale Characterization and Fabrication Laboratory (NCFL), a facility which is part of the Virginia Tech Institute for Critical Technology and Applied Sciences (ICTAS). Single tilt sample manipulation was used with the default setting for this TEM at 200 kV and 108 μA. To assist with mixing and dispersion of materials a Qsonica Q55 ultrasonic processor (110 V, 55 W, 50/60 Hz) was used for ultrasonication and a Branson Ultrasonics M2800 cleaner (120 V, 40 kHz) was used for bath sonication.

3. Approach

The biggest factor in imaging individual CNCs is contrast, however, if the concentration of CNCs is not in an appropriate range and well dispersed then optimizing contrast has little effect. Thus, CNC concentration and dispersion were addressed first in our work by comparing different dilutions of freeze-dried and never-dried CNCs then dispersing with mechanical and chemical means. Next, the TEM sample grid type was evaluated to determine how well the CNCs adhered to the surface. From there, various stains and application methods were explored to optimize the TEM imaging of individual CNCs.

The final protocol for CNC sample preparation for TEM imaging is as follows. The CNCs were dispersed in DI water to a prescribed concentration using bath sonication to ensure dispersion. The CNC solution was then applied to the TEM grid by drop with a transfer pipette. This drop was then left on the grid for one minute before a drop of stain was applied and let stand for 30 s prior to removing the excess with the dunk method, described in Section 4.3 below. The grid was then allowed to fully dry in air while in the sample case at least 12 h prior to imaging with the TEM. The following sections discuss the development of this standard protocol.

4. Results and discussion

4.1. Concentration and dispersion

The goal of characterizing individual CNCs from solution depends on several key parameters including the concentration and dispersion of the particles on the TEM grid. The concentration of the CNC sample for TEM imaging is a balance between overlapping particles (hindering individual CNC characterization) and too few particles (limiting the ability to locate the CNCs). CNC dispersion concentrations similar to those found in literature (see Table 1) were compared during this study, including 5 mg/mL, 1 mg/mL, 0.1 mg/mL, and 0.01 mg/mL. Fig. 1a–d show a comparison of concentrations obtained in this study. It was determined that a sample concentration range between 0.1 mg/mL and 0.01 mg/mL was plentiful enough to locate the particles yet minimal enough to limit multilayer deposition. At these low concentrations, the probability of CNC−CNC interaction is minimal, so clumping is limited (Gençer, Schütz, & Thielemans, 2016; Lu et al., 2014; Xu, Tang, & Ouyang, 2017). Negatively charged sulfate ester groups inherent on sulfur-hydrolyzed CNCs also aid in dispersion in water (Zhong, Fu, Peng, Zhan, & Sun, 2012). Further options were also explored to limit bundle formation during drying.

Additionally, the state of the starting materials was evaluated to determine the impact of freeze-dried versus never-dried CNCs. The CNC material from the US Forest Service was received as a freeze-dried product which was rehydrated in DI water (freeze-dried CNCs). The CNC product from the University of Maine was received as an 11.8 wt% gel in which the CNCs had never been dried (never-dried CNCs). In other words, from the hydrolysis process to the packaging of the aqueous gel, the CNC product remained in an aqueous media. It was found that the dried CNCs clumped more than the never-dried CNCs, which was also reported by (Kaushik et al., 2014). Fig. 1 shows the typical findings during this study of clumping being more prevalent with the dried CNCs compared with never-dried CNCs.

For further particle dispersion, bovine serum albumin (BSA) was added to the CNC solution prior to sample preparation for TEM (Michen et al., 2015). BSA is a protein with positively and negatively charged areas and can be used as a surfactant. Because the CNCs have a slight negative charge due to the sulfate groups, positive groups on the BSA adhere to the negatively charged CNCs with the remaining BSA chain providing steric stability for the particle. This keeps the CNC particles separated during drying of the droplet on the TEM grid (see Fig. 1e–f) (Michen et al., 2015). Using the protocol by Michen et al., the concentration of BSA was determined for each concentration of CNCs used (Michen et al., 2015). It was determined that for the 1:1 vol ratio of BSA to CNC solution suggested by Michen's protocol, a concentration of 2 mg/mL of BSA in water was added to 0.1 mg/mL CNC solution. Likewise, for 0.01 mg/mL CNC solution, 0.2 mg/mL BSA solution was added in a 1:1 vol ratio. Higher concentrations of BSA were initially

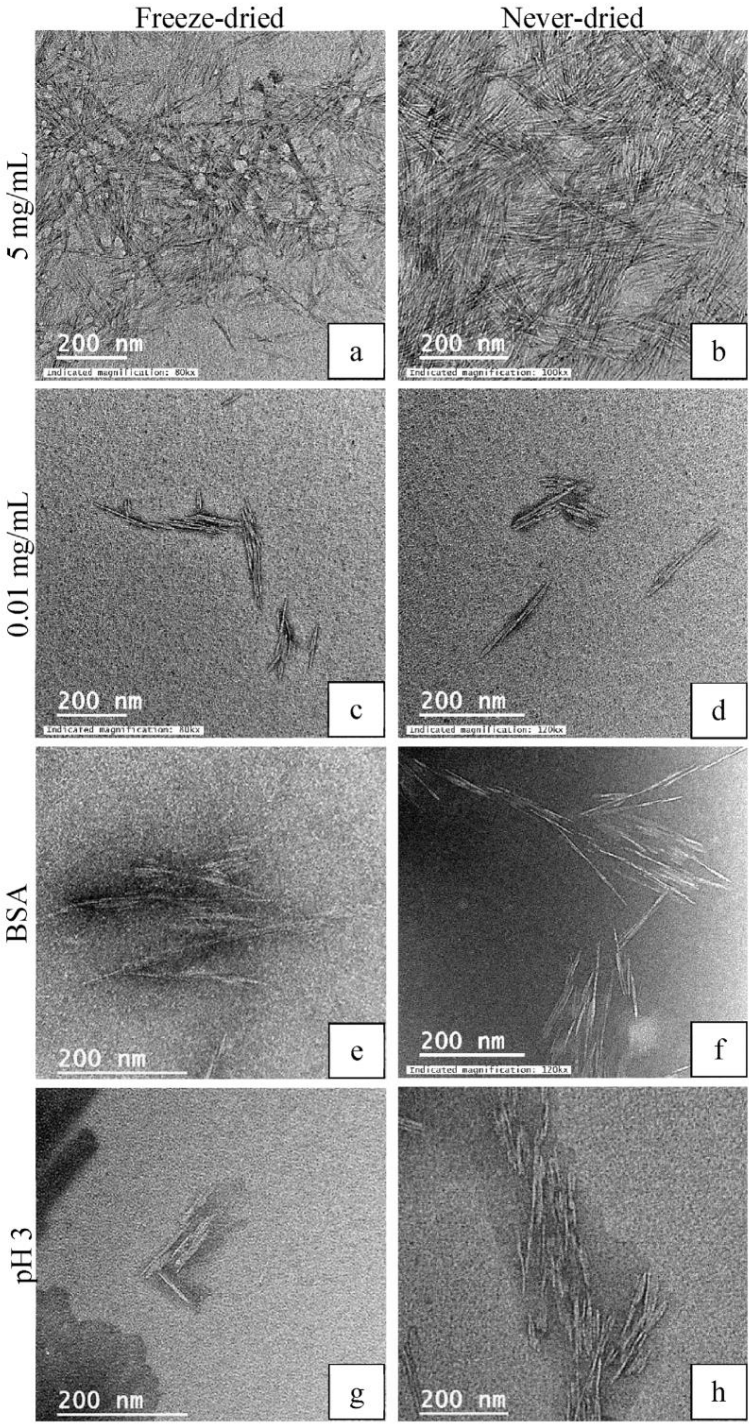

Fig. 1. Transmission electron micrographs of various methods used to disperse CNCs. CNCs dispersed with a high concentration of 5 mg/mL from a) freeze-dried or b) never-dried source material; CNCs dispersed with a low concentration of 0.01 mg/mL from c) freeze-dried or d) never-dried source material; low concentration (0.01 mg/mL) of CNCs additionally dispersed using BSA from e) freeze-dried or f) never-dried source material; low concentration (0.01 mg/mL) of CNCs additionally dispersed using HCl to reach pH 3 from g) freeze-dried or h) never-dried source material. All images used NanoVan® stain for increased contrast.

used and it was found that a film of BSA and/or excessive crystals of BSA would form on the sample, causing charging, obscuring visibility of CNCs, or limiting magnification. The BSA did provide dispersion advantages for both the freeze-dried and wet CNC materials. However, if there was clumping within the CNC solution prior to the addition of BSA, the BSA did not separate the particles. Therefore, sonication was frequently used before and after the addition of the BSA.

Another method for CNC dispersion was to lower the pH of the CNC

solution to take advantage of electrostatic repulsion. It has been shown that CNCs bundles can be dispersed at low pH where the surface charge and zeta potential are sufficient to prevent aggregation in solution (Kaushik et al., 2014). At pH 4, CNCs are fully protonated and the pKa of sulfate ester groups is around 2 (Beck, Méthot, & Bouchard, 2014; Cranston, Gray, & Rutland, 2010). Zeta potentials of CNCs at low concentrations remain stable at near −20 mV or lower, and viscosities of CNC solutions are also lower between pH 2–4 compared with more neutral pH solutions, indicating fewer particle interactions and more separation at low pH (Navon, Radavidson, Putaux, Jean, & Heux, 2017; Xu, Atrens, & Stokes, 2017). Thus a CNC solution with pH 3 was selected to study the effect on aggregation during drying. To make a pH 3 solution, 0.01N HCl was added to 0.01 mg/mL CNCs until the pH reached 3.0. This solution was then dropped onto a TEM grid and stained with NanoVan® for imaging in the TEM. Fig. 1e–h shows a comparison between dispersion using BSA and low pH, for both dried and never-dried CNCs. There appears to be no significant difference in the dispersion effects between the use of bovine serum albumin and low pH. Likewise, for dried CNCs versus never-dried CNCs dispersed with BSA compared with low pH, there was no significant effect. It was noted that for the samples examined with pH 3 and staining, some of the stain within the samples concentrated and appears as spotting as shown in Fig. 1g–h, which was likely due to the pH change.

4.2. TEM grid type

For the CNC sample to successfully deposit and survive the electron bombardment from the TEM the proper grid type is necessary. TEM grids with a support film, such as Formvar, can be used to image small nanometer size samples. Several grids with different surface coatings were evaluated, including Formvar with carbon and Formvar with silicon monoxide. The layer of evaporated carbon provides conductivity while the silicon monoxide is a more hydrophilic surface than carbon alone (Kaushik et al., 2014).

The final grid that was selected for experimentation was the silicon monoxide-coated Formvar grids. In addition to being hydrophilic, the silicon monoxide coating is stable under high voltage electron beam and provides a lower background contrast which enhanced the viewing of the CNCs. Subsequently, during this study it was also observed that the Formvar grids began to become more hydrophobic with age and more difficult to use so the aqueous sample droplets would not adhere. Plasma cleaning is recommended to address this issue and is common practice for use of TEM grids with support films. For this study, newly purchased grids were used for each sample to avoid aging of the grids.

4.3. Staining solution and stain method

The contrast between the CNCs and the background is key to locating the CNCs and focusing on the details of individual crystals on a TEM grid at high magnification (above 100 kX). Because of the similarity in electron density of the CNCs with the Formvar grids in addition to the small thickness of the CNCs (5–20 nm), additional measures usually need to be taken to enhance contrast of the CNCs. This may include staining the sample or modifying the TEM electron beam through voltage or aperture adjustments. Fig. 2 shows images of stained versus unstained CNCs where the stained CNCs have more defined edges and are more quickly found in the TEM. It is difficult in static images to express the challenge in locating individual or small clumps of CNCs, but generally the user begins at a magnification less than 50 kX (still a high magnification) and areas of interest are typically identified by areas that appear darker or less uniform. The magnification is gradually increased and focus is adjusted at which point the indication of CNCs begins to appear such as in Fig. 2a–b. Staining usually eases this process because the heavy metal stain contrasts with the CNCs and the background through a large difference in electron density. Finally, magnification above 100 kX and up to 500 kX is used to image the CNCs such as in Fig. 2c–d. Again the stained CNCs are easier to focus on (note that over and under focusing are not addressed here) and though damage to the CNCs by the electron beam does occur, it is not seen as quickly with the stained samples.

We evaluated several stains for this work to determine an optimal chemical and method for TEM imaging of individual CNCs. For staining cellulose materials, uranyl acetate is generally used by most researchers (see Table 1). Several other stains were chosen which were non-radioactive in nature in order to increase ease of use and disposal. These stains included iodine, ammonium molybdate and a vanadium-based solution branded NanoVan® (Hainfeld et al., 1994; Kaushik et al., 2015). These negatively-charged stains have been used successfully in literature, but as they are oppositely charged in water compared with the positively charged uranyl acetate, they are generally not as efficient in staining CNCs but are more accessible. Fig. 3 illustrates the three non-radioactive stains with CNCs.

Iodine was initially thought to be the easiest and most accessible stain method. The 0.05 M iodine solution as received was diluted to 2% by volume and directly applied to the sample on the TEM grid. While the iodine stain provided a dark background for contrast, the stain overbearingly adsorbed to both the sample and Formvar surface and did not give clear edges to the CNCs. Hence, details could not be visualized enough for size analysis of the individual CNCs. Other works published suggest that iodine would best be used with vapor deposition rather than the aqueous drop method used in this study (Boyde, McCorkell, Taylor, Bomphrey, & Doube, 2014), though iodine was also not well studied in literature for the application of cellulose nanocrystals.

Ammonium molybdate was another possible alternative due to its previous use in literature and ease of access (see Table 1). However, the aggressiveness of the stain meant that most all of the surface of the grid and sample was stained, limiting contrast between object and background when used at a concentration of 2 w/v%.

Finally, a vanadium-based commercial stain, NanoVan®, was obtained and used within this study. This stain was received in a ready to use formulation so no dilution was required. It was found that the NanoVan® provided good contrast in a similar manner found when uranyl acetate stain was used. NanoVan® and ammonium molybdate both have a slight negative charge, however, NanoVan®, was found to migrate specifically to the CNCs more than ammonium molybdate. Samples stained with ammonium molybdate showed limited CNC stain targeting since the stain was similarly attracted to the CNCs and the TEM grid. This difference in stain effectiveness is likely due to differences in van der Waals forces or that molybdate has a divalency compared with the monovalency of vanadate.

In order for the stains to function properly, the deposition method was key. It was found that CNCs that had already been applied to a grid surface and dried did not attract the stain; therefore, the stain did not isolate the CNCS or provide any additional contrast. Hence, the CNCs needed to remain hydrated when the stain was applied. After a CNC solution was dropped onto the TEM grid it was left to set for one minute to allow CNCs to adsorb to the surface of the grid, falling out of the droplet. Then the staining solution was applied directly to the sample droplet. The stain was left to set 15–30 s to allow an appropriate amount of stain to deposit.

To remove the excess droplet left on the grid, several methods were tested (see Fig. 3): wick, rinse and dunk. To wick the excess, a tissue paper was used to touch the edge of the TEM grid briefly to pull away excess liquid. To rinse, a drop of DI water was deposited on top of the droplet on the grid then the excess was wicked away as described above. Finally, to dunk, after the stain wait time was complete the TEM grid was dipped (dunked) in and directly out of a beaker containing DI water. There was no wicking step used after the grid was dunked because the droplet is removed during the dunk. For each of these methods, the TEM grid was held by its edge with a pair of reverse action tweezers. Additionally, after the excess stain was removed by any of the methods, the grid remained wet and was placed into the sample box

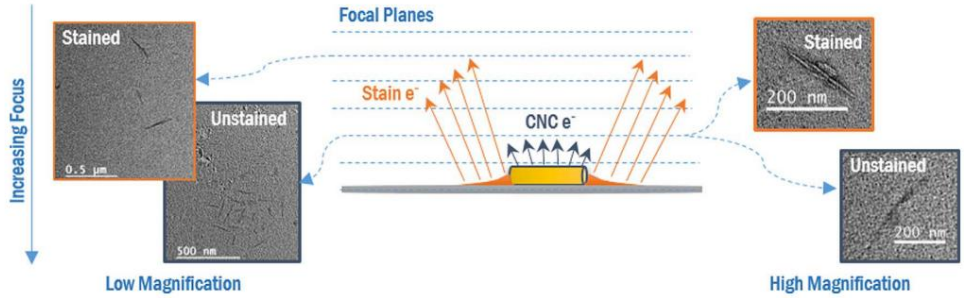

Fig. 2. TEM images of stained (a and c) and unstained CNCs (b and d) at increasing focal planes. When identifying CNCs on the grid, the user begins at a higher focal plane and increases focus until CNCs are found, at which point magnification can increase. Stained CNCs are quicker and easier to find in TEM and are less prone to damage than unstained CNCs.

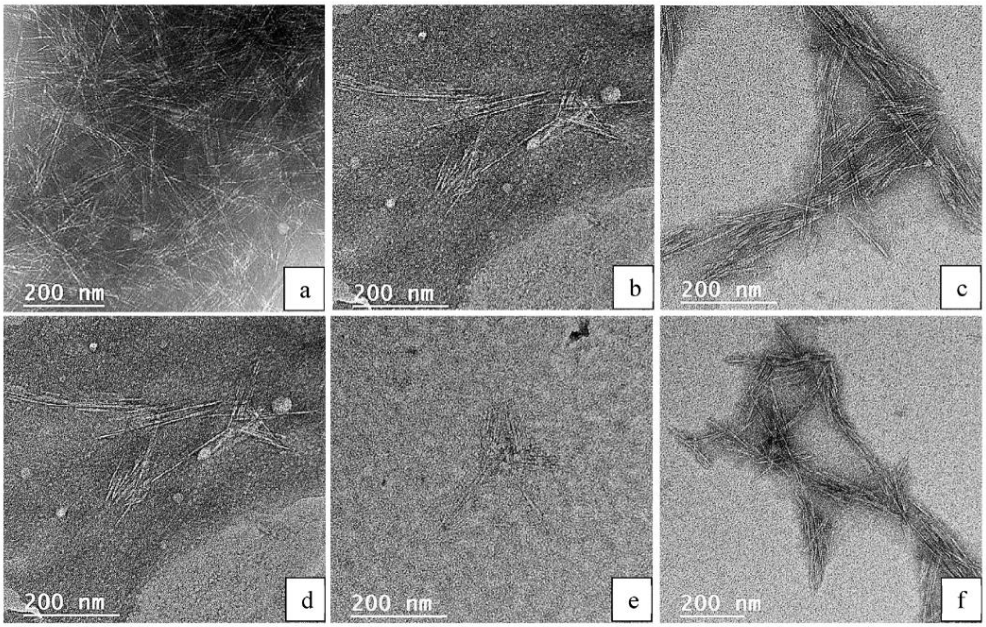

Fig. 3. Several stains were evaluated as alternatives to uranyl acetate; (a) iodine was unable to isolate CNCs well enough to gather detailed images; (b) ammonium molybdate was an aggressive stain and did not consistently migrate to the CNCs exclusively, since the dye covers a large area of the grid (dark areas); (c) NanoVan® provided the best and most consistent staining, highlighting the CNCs. After the stain is deposited onto the sample (TEM grid with sample droplet), the excess must be removed. Three methods were evaluated: (d) wicking with an absorbent paper which left behind excess stain and BSA crystals, (e) adding an addition drop of DI water then wicking the excess which tended to wash away much of the stain though it did remove the excess BSA crystals, and (f) dunking the grid into a beaker of DI water which removed excess crystalline stain and BSA and left behind the stained sample.

where it was left to dry fully for 12–24 h.

These stain removal methods were evaluated with TEM images. It was found that the wicking method generally left behind excess stain and BSA crystals, obscuring the CNCs, and in some cases removing many of the CNCs from the sample grid. The rinse method tended to remove too much stain and sometimes sample such that the increase, in contrast, was relatively low. The dunk method provided the most consistent means to remove excess stain and remaining BSA without removing CNCs.

4.4. Staining modified CNCs

A brief analysis was conducted to determine if the best methods identified in this study could be applied to modified CNCs. From the received University of Maine product, CNCs were modified with TEMPO (TEMPO-CNCs). The process for TEMPO oxidation was based on papers prepared by (Habibi, Chanzy, & Vignon, 2006) and (Follain, Marais, Montanari, & Vignon, 2010). From the received US Forest Service product, the CNCs were modified with rhodamine b (R-CNCs) based on methods from (Haghpanah et al., 2013). The final standard protocol formed from the above experiments was used for TEM sample preparation, including BSA dispersion, NanoVan® as the stain, and the dunk method to remove excess stain. The R-CNCs, shown in Fig. 4a, minimally attracted the stain and the BSA was left in excess. The TEMPO-CNCs, shown in Fig. 4b, did not become stained, instead, the stain appeared to have clumped, which then attached to the CNCs. Further studies of imaging modified CNCs in TEM is necessary for technique enhancement.

Rhodamine b has an overall positive charge and TEMPO-oxidation causes a higher negative charge, so staining differences are expected. Since TEMPO remains negatively charged, it is expected that the stain would target the CNCs, rather than the stain clumping as shown in Fig. 4. Rhodamine is oppositely charged, so less stain targeting is expected compared with sulfonated CNCs. Further studies to image

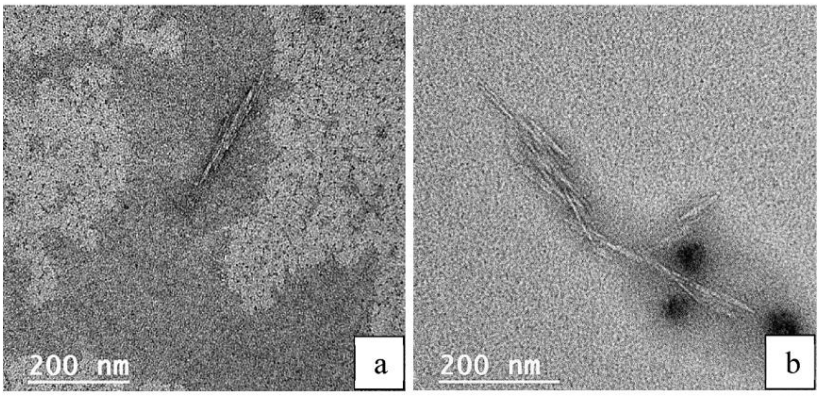

Fig. 4. Since there is much work conducted with modified CNCs, an evaluation of the stains in this study were combined with (a) R-CNCs and (b) TEMPO-CNCs. Small clusters of CNCs were achievable using BSA and NanoVan® to treat the CNC dispersion during TEM sample preparation.

modified CNCs in TEM is necessary for technique enhancement and likely requires optimization based on the surface charge of each specific system.

4.5. Imaging using reduced voltage

An alternative means for increasing contrast in the TEM images of CNCs with reduced voltage was evaluated. Images of unstained CNCs were taken using a JOEL 2100 TEM operated at voltages lower than 200 kV, specifically 120 kV and 80 kV. Fig. 5 shows the resulting comparison of the three voltage settings viewing the same CNC nanoparticle. With decreasing voltage, a slight increase, in contrast, was possible, however, there was a decrease in resolution. Locating and focusing on the CNCs became more difficult as the accelerating voltage was reduced as discussed previously and illustrated in Fig. 2.

Additionally, it was observed during this work that with extended electron beam exposure, the CNC particles will show degradation, decreasing in sharpness within the images and eventually appearing to fully degrade leaving a shadow of the particle within the Formvar film.

4.6. New insights

This study evaluated several sample preparation methods for TEM imaging of CNCs. The most consistent results of good contrast and individual CNCs at high magnification were found when using a low (0.01–0.1 mg/mL) concentration of CNCs dispersed in an aqueous solution with BSA, dropped onto a TEM grid with Formvar/silicon monoxide support surface, and stained with NanoVan®. Excess stain was best removed using the dunk method and images were taken at 200 kV.

The CNC solution concentration found to maximize the dispersion of CNCs such that individual particles could be distinguished was 0.01 mg/mL and dispersed with bath sonication. This solution was further dispersed with 0.2 mg/mL of BSA and mixed with a vortex mixer. Additionally, it was shown that using a never-dried source of CNCs improved dispersibility. These aqueous samples of CNCs prepared with BSA were applied dropwise to a 200 mesh copper TEM grid with silicon monoxide coated Formvar support film to ensure the capture of CNCs on the grids. Finally, heavy metal negative staining was used to enhance the contrast between the CNC particles and the Formvar grid surface. A standard stain for this type of work with biological material is uranyl acetate, a radioactive material, which poses health, handling and disposal limitations; therefore, alternative stains were evaluated. The alternative that provided acceptable contrast consistently stained the CNCs, and left minimal residue on the sample was NanoVan® and was deposited dropwise then removed with the dunk method.

4.7. Troubleshooting

Troubleshooting guidelines have been compiled from experience derived from this study. Table 2 provides a list of common problems during TEM imaging of CNCs and their likely causes with subsequent proposed solutions.

5. Conclusion

Transmission electron microscopy (TEM) is a common technique for acquiring images of CNCs at high magnification. However, CNCs image contrast and resolution can be limited by the low electron densities of these carbon materials and their low profile (thin). By enhancing the particle dispersion with a surfactant and choosing the appropriate grid surface, a well dispersed CNC sample can be successfully prepared for TEM imaging. This study evaluated several stains and staining methods

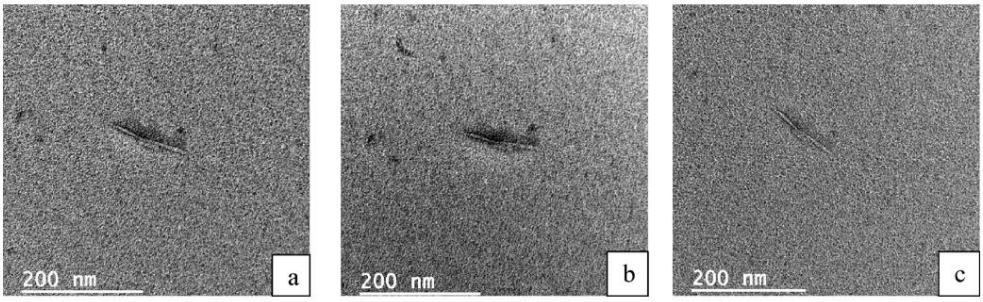

Fig. 5. TEM images of the same never-dried CNC from a 0.01 mg/mL concentration dispersion with BSA and not stained but imaged at varying voltages (a) 80 kV, (b) 120 kV, and (c) 200 kV 200 kV is considered standard voltage for this study. With a decrease in voltage, there was a slight contrast increase and a decrease in resolution.

Table 2
Troubleshooting tips for imaging CNC samples in TEM.

Problem	Possible Reason	Solution	Problem Image	Solution Image
Mat of CNCs	Concentration of CNCs is too high	Lower concentration of CNC solution	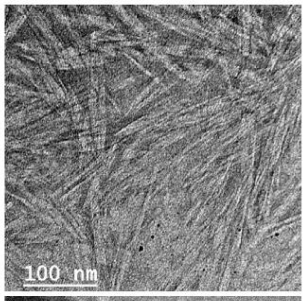	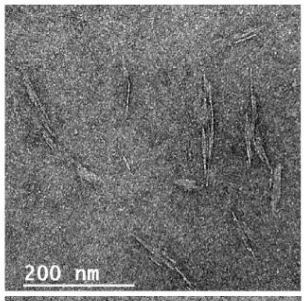
Clumping CNC	CNCs not well dispersed	• Increase sonication time • Use wet CNCs that have never been dried post-hydrolysis • Recalculate BSA concentration needed; alternatively, lower pH of CNC solution to 3-3.5 if not using BSA	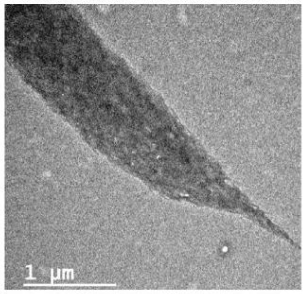	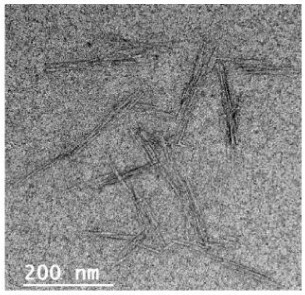
Grid film holes or film rupture	Excess charge build up on surface of the film which may be caused by excess BSA, stain, other salt, or lack of sample all of which could not be directing the current to drain away from the grid	• Adjust the concentration of the BSA or stain; alternatively balance the ratio of sample to stain • It is possible that the CNC sample solution has residual reagents such as salts remaining from processing; samples can be washed, such as using a centrifuge method or dialysis	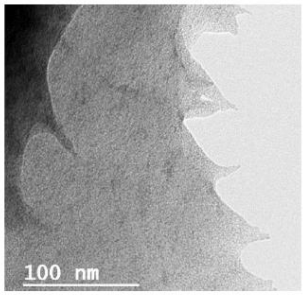	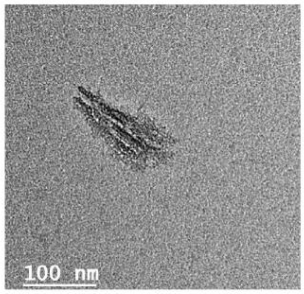
High magnification focus challenges	Excess residual BSA, stain or reagents obscuring sample or causing excess charge on the surface	Modification of BSA or stain concentrations, pre-washing of sample to remove reagents or use of the dunk method to remove excess after staining	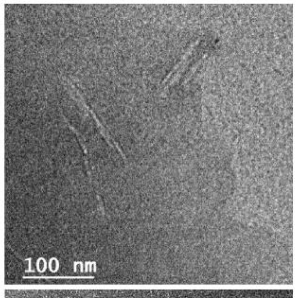	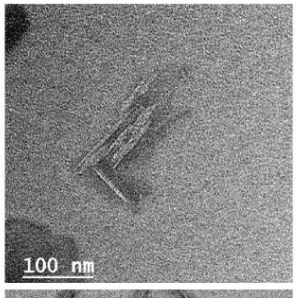
Little to no sample can be located	• Low concentration of sample • Hydrophobic grid surface • Excessive removal post-staining	• Increase the concentration of sample • Use fresh/new grid, plasma clean grid and store grids in desiccant enclosure are options • If the dunk method washes away too much material and the grid is fresh, try the wick process for removal of excess post-staining	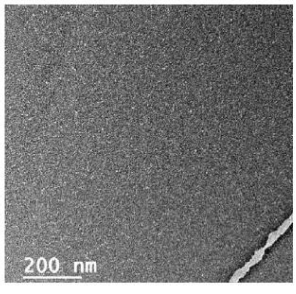	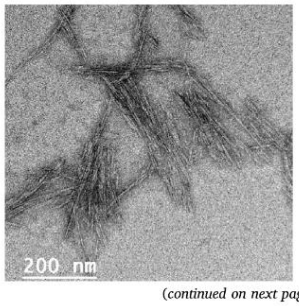

(*continued on next page*)

Table 2 (*continued*)

Problem	Possible Reason	Solution	Problem Image	Solution Image
BSA crystals	Excess BSA due to concentration or inadequate excess removal post-staining	• Adjust the concentration of BSA or ratio of BSA to sample solution • Reduce incubation period for BSA/sample solution; i.e. use BSA/sample solution directly after mixing • If the dunk method leaves residual crystals, combine a rinse drop with the dunk	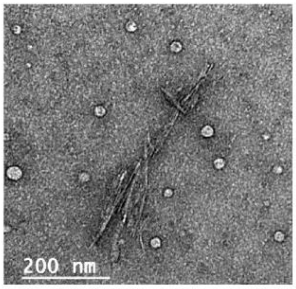	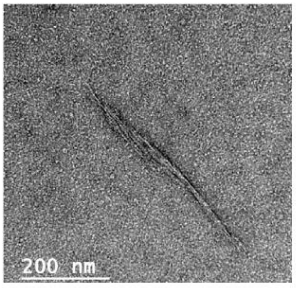
Crystalline deposits	Excess stain crystals	• Adjust the concentration of stain solution • Reduce the stain wait • If the dunk method leaves residual crystals, combine a rinse drop with the dunk	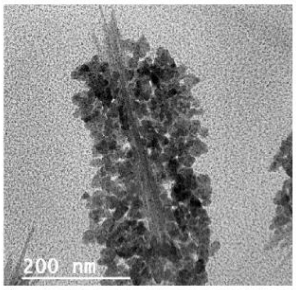	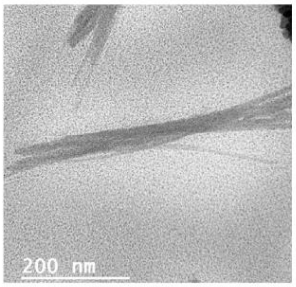
Splochiness in images	This could be due to excess stain or BSA/reagents being stained	• Enhance the excess removal method by combining a rinse drop with the dunk • Reduce the concentration or quantity of stain or BSA • Wash samples pre-staining with a centrifuge method or dialysis to eliminate residual reagents	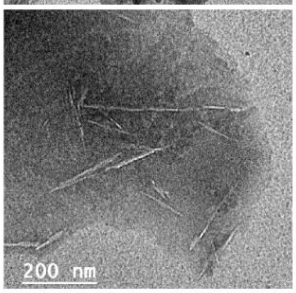	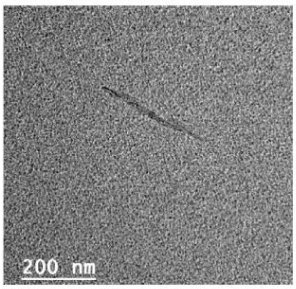
Stain covering all surfaces rather than migrating to sample	• The surface groups on the CNC samples may not be compatible with the stain chosen • There may be too much BSA coating the surface of the sample and grid	• Try other stains • Reduce the concentration or quantity of BSA and/or increase the aggressiveness of the excess removal post-staining with either a rinse combined with dunk or multiple dunks	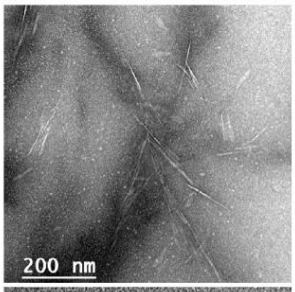	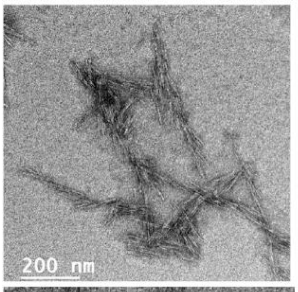
CNC contrast degradation	The grid under observation has been exposed to the beam for too long. The CNCs begin to degrade with exposure.	Locate and focus on the plane of the CNCs, then move to an adjacent grid to image CNC's. This will limit the time required to focus and acquire an image because the first grid will have taken the majority of the beam time while the user aligns and focuses to the correct plane.	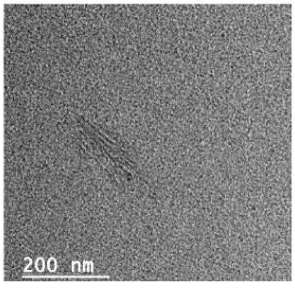	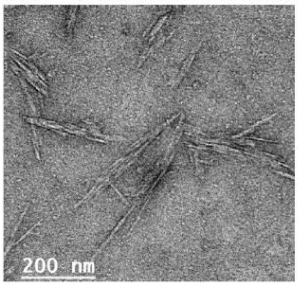

for contrast enhancement of CNCs in TEM imaging. A final protocol using bovine serum albumin, SiO-coated TEM grid, NanoVan® stain, and a dunk method for sample application was found to be a reliable method for TEM imaging of individual CNCs without using radioactive stain or an expensive glow-discharge device. A TEM imaging trouble-shooting table was also provided to identify and correct imaging artifacts. Future work may include an analysis of staining for SEM imaging in addition to alternative stain types and dispersants for CNCs with various surface functional groups.

Funding

The authors gratefully acknowledge financial support from the Material Science and Engineering Department at Virginia Tech and the Endowment for Forestry and Communities (P3Nano). Author EJF is visiting Professor in LabEx Tec 21, Grenoble, France (Investissements d'Avenir − grant agreement n°ANR-11-LABX-0030).

Conflicts of interest

The authors have no conflicts of interest to disclose with respect to this article.

Acknowledgements

The authors acknowledge use of the facilities and the assistance of Chris Winkler at the Nanoscale Characterization and Fabrication Laboratory (NCFL) at Virginia Polytechnic Institute. The authors would also like to thank Kathy Lowe at the Virginia-Maryland College of Veterinary Medicine for their assistance with uranyl acetate staining and waste disposal.

References

Beck, S., Méthot, M., & Bouchard, J. (2014). General procedure for determining cellulose nanocrystal sulfate half-ester content by conductometric titration. *Cellulose, 22*(1), 101–116. http://dx.doi.org/10.1007/s10570-014-0513-y.

Biyani, M. (2014). *Light stimulated mechanically adaptive cellulose based nanocomposites, (Doctorate).* University of Fribourg.

Boyde, A., McCorkell, F. A., Taylor, G. K., Bomphrey, R. J., & Doube, M. (2014). Iodine vapor staining for atomic number contrast in backscattered electron and X-ray imaging. *Microscopy Research and Technique, 77*(12), 1044–1051. http://dx.doi.org/10.1002/jemt.22435.

Choi, Y. (2006). *Cellulose nanocrystals filled carboxymethyl cellulose composites, (Master of science).* Oregon State University.

Cranston, E. D., Gray, D. G., & Rutland, M. W. (2010). Direct surface force measurements of polyelectrolyte multilayer films containing nanocrystalline cellulose. *Langmuir, 26*(22), 17190–17197. http://dx.doi.org/10.1021/la1030729.

Elazzouzi-Hafraoui, S., Nishiyama, Y., Putaux, J.-L., Heux, L., Dubreuil, F., & Rochas, C. (2008). The shape and size distribution of crystalline nanoparticles prepared by acid hydrolysis of native cellulose. *Biomacromolecules, 9*(1), 57–65.

Espinosa, S. C., Kuhnt, T., Foster, E. J., & Weder, C. (2013). Isolation of thermally stable cellulose nanocrystals by phosphoric acid hydrolysis. *Biomacromolecules, 14*(4), 1223–1230. http://dx.doi.org/10.1021/bm400219u.

Follain, N., Marais, M.-F., Montanari, S., & Vignon, M. R. (2010). Coupling onto surface carboxylated cellulose nanocrystals. *Polymer, 51*(23), 5332–5344. http://dx.doi.org/10.1016/j.polymer.2010.09.001.

Gençer, A., Schütz, C., & Thielemans, W. (2016). Influence of the Particle Concentration and Marangoni Flow on the Formation of Cellulose Nanocrystal Films. *Langmuir, 33*(1), 228–234.

Habibi, Y., Chanzy, H., & Vignon, M. R. (2006). TEMPO-mediated surface oxidation of cellulose whiskers. *Cellulose, 13*(6), 679–687. http://dx.doi.org/10.1007/s10570-006-9075-y.

Habibi, Y., Lucia, L. A., & Rojas, O. J. (2010). Cellulose nanocrystals: Chemistry, self-assembly, and applications. *Chemical Reviews, 110*(6), 3479–3500. http://dx.doi.org/10.1021/cr900339w.

Haghpanah, J. S., Tu, R., Da Silva, S., Yan, D., Mueller, S., Weder, C., & Montclare, J. K. (2013). Bionanocomposites: Differential effects of cellulose nanocrystals on protein diblock copolymers. *Biomacromolecules, 14*(12), 4360–4367. http://dx.doi.org/10.1021/bm401304w.

Hainfeld, J. F., Safer, D., Wall, J. S., Simon, M., Lin, B., & Powell, R. D. (1994). Methylamine vanadate (NanoVan) negative stain. *Paper presented at the In proc. 52nd ann. mtg. micros. soc. amer.*.

Hosseinidoust, Z., Alam, M. N., Sim, G., Tufenkji, N., & van de Ven, T. G. (2015). Cellulose nanocrystals with tunable surface charge for nanomedicine. *Nanoscale, 7*(40), 16647–16657. http://dx.doi.org/10.1039/c5nr02506k.

Ikeda, K., Inoue, K., Kanematsu, S., Horiuchi, Y., & Park, P. (2011). Enhanced effects of nonisotopic hafnium chloride in methanol as a substitute for uranyl acetate in TEM contrast of ultrastructure of fungal and plant cells. *Microscopy Research and Technique, 74*(9), 825–830. http://dx.doi.org/10.1002/jemt.20964.

Jorfi, M., Roberts, M. N., Foster, E. J., & Weder, C. (2013). Physiologically responsive, mechanically adaptive bio-nanocomposites for biomedical applications. *ACS Appl Mater Interfaces, 5*(4), 1517–1526. http://dx.doi.org/10.1021/am303160j.

Kaushik, M., Chen, W. C., Van de Ven, T. G., & Moores, A. (2014). An improved methodology for imaging cellulose nanocrystals by transmission electron microscopy. *Nordic Pulp and Research Center: Nanocellulose, 29*(1), 23.

Kaushik, M. Fraschini, C. Chauve, G. Putaux, J.-L. Moores, A. (2015) Transmission Electron Microscopy for the Characterization of Cellulose Nanocrystals. In The Transmission Electron Microscope − Theory and Applications (pp. 129–163): InTech.

Kvien, I., Tanem, B. S., & Oksman*, K. (2005). Characterization of cellulose whiskers and their nanocomposites by atomic force and electron microscopy. *Biomacromolecules, 6*, 3160–3165.

Lu, Q., Tang, L., Lin, F., Wang, S., Chen, Y., Chen, X., & Huang, B. (2014). Preparation and characterization of cellulose nanocrystals via ultrasonication-assisted FeCl3-catalyzed hydrolysis. *Cellulose, 21*(5), 3497–3506.

Michen, B., Geers, C., Vanhecke, D., Endes, C., Rothen-Rutishauser, B., Balog, S., & Petri-Fink, A. (2015). Avoiding drying-artifacts in transmission electron microscopy: Characterizing the size and colloidal state of nanoparticles. *Scientific Reports, 5*, 9793. http://dx.doi.org/10.1038/srep09793.

Montanari, S., Roumani, M., Heux, L., & Vignon, M. R. (2005). Topochemistry of carboxylated cellulose nanocrystals resulting from TEMPO-mediated oxidation. *Macromolecules, 38*(5), 1665–1671. http://dx.doi.org/10.1021/ma048396c.

Moon, R. J., Martini, A., Nairn, J., Simonsen, J., & Youngblood, J. (2011). Cellulose nanomaterials review: Structure, properties and nanocomposites. *Chemical Society Reviews, 40*(7), 3941–3994. http://dx.doi.org/10.1039/c0cs00108b.

Navon, Y., Radavidson, H., Putaux, J. L., Jean, B., & Heux, L. (2017). pH-sensitive interactions between cellulose nanocrystals and DOPC liposomes. *Biomacromolecules, 18*(9), 2918–2927. http://dx.doi.org/10.1021/acs.biomac.7b00872.

Postek, M. T., Vladár, A., Dagata, J., Farkas, N., Ming, B., Wagner, R., & Beecher, J. (2011). Development of the metrology and imaging of cellulose nanocrystals. *Measurement Science and Technology, 22*(2), 024005. http://dx.doi.org/10.1088/0957-0233/22/2/024005.

Potter, K. A., Jorfi, M., Householder, K. T., Foster, E. J., Weder, C., & Capadona, J. R. (2014). Curcumin-releasing mechanically adaptive intracortical implants improve the proximal neuronal density and blood-brain barrier stability. *Acta Biomaterialia, 10*(5), 2209–2222. http://dx.doi.org/10.1016/j.actbio.2014.01.018.

Qua, E. H., Hornsby, P. R., Sharma, H. S. S., & Lyons, G. (2011). Preparation and characterisation of cellulose nanofibres. *Journal of Materials Science, 46*(18), 6029–6045. http://dx.doi.org/10.1007/s10853-011-5565-x.

Ranby, B. G. (1951). The colloidal properties of cellulose micelles. *Fibrous Macromolecular Systems: Cellulose and Muscle*, 158–164.

Wicaksono, R., Syamsu, K., Yuliasih, I., & Nasir, M. (2013). Cellulose nanofibers from cassava bagasse: Characterization and application on tapioca-film. *Chemistry and Materials Research, 3*(13), 10.

Xu, Y., Atrens, A. D., & Stokes, J. R. (2017). Rheology and microstructure of aqueous suspensions of nanocrystalline cellulose rods. *Journal of Colloid and Interface Science, 496*, 130–140. http://dx.doi.org/10.1016/j.jcis.2017.02.020.

Zhou, J., Butchosa, N., Jayawardena, H. S., Park, J., Zhou, Q., Yan, M., & Ramstrom, O. (2015). Synthesis of multifunctional cellulose nanocrystals for lectin recognition and bacterial imaging. *Biomacromolecules, 16*(4), 1426–1432. http://dx.doi.org/10.1021/acs.biomac.5b00227.

Zhong, L., Fu, S., Peng, X., Zhan, H., & Sun, R. (2012). Colloidal stability of negatively charged cellulose nanocrystalline in aqueous systems. *Carbohydrate polymers, 90*(1), 644–649.

de Paula, E. L., Mano, V., Duek, E. A. R., & Pereira, F. V. (2015). Hydrolytic degradation behavior of plla nanocomposites reinforced with modified cellulose nanocrystals. *Química Nova*. http://dx.doi.org/10.5935/0100-4042.20150108.

Chapter 4

Collection of Airborne Ultrafine Cellulose Nanocrystals by Impinger with an Efficiency Mimicking Deposition in the Human Respiratory System

CNC toxicity to humans and the environment is not yet fully understood, however there are concerns of irritation to the lungs based on the aspect ratio being similar to asbestos. Because CNC production is increasing, safety in production facilities is of utmost concern. This chapter provides an initial step to develop an industrially practical method for quantifying the concentration of CNCs in air. This chapter expands on CNC characterization methods developed in the previous chapter. Characterization methods used in this chapter are applied to a different type of particle in subsequent chapters.

In this chapter, data and analysis concerning CNC labeling and characterization was performed by myself, directed by Dr. E. Johan Foster. Aerosolization of CNCs and design of impinger was performed by Mr. Kevin Gettz and Dr. Larissa V. Stebounova, directed by Dr. Thomas Peters at the University of Iowa. Dr. Jo Anne Shatkin advised on practicality of system development for its use in industrial settings. The chapter was drafted by myself except for sections surrounding aerosolization methodology and design of the impinger nozzle, which were drafted by Mr. Gettz and Dr. Stebounova. The draft was later edited by Dr. Thomas Peters, Dr. Shatkin, and Dr. Foster. This chapter was accepted in the Journal of Occupational and Environmental Health and the accepted version is reprinted here with permission from Taylor and Francis

Collection of airborne ultrafine cellulose nanocrystals by impinger with an efficiency mimicking deposition in the human respiratory system
Rose Roberts, Kevin Gettz, Larissa V Stebounova, Jo Anne Shatkin, Thomas Peters, and E. Johan Foster
Journal of Occupational and Environmental Hygiene, **2019**, *in press*.
DOI: 10.1080/15459624.2018.1540876.

Collection of airborne ultrafine cellulose nanocrystals by impinger with an efficiency mimicking deposition in the human respiratory system

Rose Roberts[1], Kevin Gettz[2], Larissa V Stebounova[2], Jo Anne Shatkin[3], Thomas Peters[2] and E. Johan Foster[1]

[1]Materials Science and Engineering, Virginia Tech

[2]University of Iowa

[3]Vireo Advisors

Keywords: nanoparticle, nanocellulose, airborne, cellulose nanomaterials

ABSTRACT

As cellulose nanocrystals (CNCs) are increasing in production, establishing safe workplace practices in industry will be paramount to their continued use and growth. As small high-aspect-ratio fibers, CNCs, like conventional cellulose, may be potentially hazardous in the body, especially in the lungs when inhaled. Safeguards are needed to monitor concentrations of CNCs in air in industrial and laboratory settings to protect workers. However, because of their size, morphology, and chemical makeup, CNCs are difficult to characterize and differentiate from other dust and cellulose products. This work is focused on developing an effective method of characterizing the concentration of airborne ultrafine CNCs that may deposit in the respiratory tract. CNCs were tagged with rhodamine b (RhB-CNCs) for improved visualization and characterized using UV-vis spectroscopy (UV-vis), transmission electron microscopy (TEM), and dynamic light scattering (DLS), then aerosolized and collected via a novel method using plastic impingers. Concentration of RhB-CNCs was measured using UV-vis and scanning mobility

particle sizer (SMPS). The plastic impinger with 3D-printed nozzle collected airborne CNCs at an efficiency that improves upon commercially available impingers for relevant particle sizes.

INTRODUCTION

The isolation, modification, characterization and application of cellulose nanoparticles from plants (including wood, coconut husks, sisal, tunicates, cotton, ramie, straw, sugar beet, and many others) and animals (e.g. tunicates) is currently attracting significant attention, driven by the abundance and renewable nature of the biological sources and the attractive mechanical properties of cellulose nanomaterials.[1-2] The latter originate from the hierarchical, uniaxially oriented structure of native cellulosic materials.[3-5]

Extended and aligned cellulose macromolecules (D-glucose units, which are condensed through β(1→4) glycosidic bonds) assemble into microfibrils, in which they are stabilized through hydrogen bonds. The microfibrils are largely crystalline, but they also contain regions that are less well ordered (i.e., largely amorphous). The cross-sectional dimension of the microfibrils ranges from 2-20 nm, depending on the origin of the cellulose; in the case of wood cells[6] the smallest fibril unit, referred to as elementary fibril, has a diameter of ~4 nm. The elementary fibrils aggregate to form microfibrils with diameters of ~15-20 nm, which further aggregate into larger bundles and finally, with "binders" consisting of lignin and hemicelluloses, into cellulosic fibers. These hierarchical structures can be deconstructed by mechanical and chemical processes to isolate nano-cellulose (NC), collectively referred to as *cellulose nanoparticles*. Two main types of cellulose nanoparticles can be distinguished – cellulose nanofibrils (CNF) and cellulose nanocrystals (CNC) – although it should be noted that differences in the isolation processes and the nature of the source also cause some variation within these families.

Cellulose dust is an irritant, so there is reason to believe cellulose nanomaterials in air also may be. Engineered nanoparticles also can remain in the air longer. There are key differences due to particle size – smaller particles (<0.1 μm) tend to be inhaled deeper in the lung than larger particles (>1 μm), which can get trapped in the upper airways and cleared.[7-9] The aspect ratio of CNCs (5-30 aspect ratio) and CNFs (10-100 aspect ratio) raise concerns about fibrotic behavior in the lung.[10] A 24-hour study found inflammation occurred in mice after high dose single exposures to CNC,[11] and cytotoxicity towards bacteria exists,[12] although other *in vitro* studies did not identify these effects.[13-15]

Many researchers, as well as pilot plant operators, are now handling cellulose nanomaterial in various forms, and guidelines are needed to ensure safety. Research groups in Canada and Finland have developed/reported measurement methods for cellulose nanomaterial in liquid media. One study measuring airborne CNF was reported in Finland,[16] and initial results from the National Institute for Occupational Safety and Health (NIOSH) field team reported exposure to CNC from some tasks in the Forest Products Laboratory (FPL) pilot plant.[17] As identified in a recent Roadmap for Nanocellulose Environmental Health and Safety,[18] a reliable method of assessing airborne exposures to CNCs is needed that carefully addresses the presence of background particulate matter.

Particle measurement is challenging because filter media and many background sources of particles are also cellulosic. Sampling methods using carbon-based filters, such as polycarbonate or polymer-based foam filters, make it difficult to quantify collected amount of CNCs because of their similar atomic makeup. In their interim report, NIOSH discusses the need to identify ways to analyze samples collected onto filters, as well as in biological matrices. Determining a reliable method for real time sampling and quantitative assessment of airborne exposure for CNC and CNF

is an urgent need to ensure safety when generating these materials, and for users of pilot plant material in academic, research and other organizations, as well as private/academic producers.

Midget impingers are small and lightweight sampling devices designed for personal sampling, and have been used to collect particles, bioaerosols and gases directly into a volume of liquid since the 1920s.[19-20] Some studies have investigated the collection efficiency (fraction of particles of a specific size collected by the sampler) of single-jet midget impingers (with a nozzle diameter of 1 mm) for submicron particles.[21-23] Collection efficiency in these studies ranged from less than 10% to 40%. A fritted impinger employs a sintered porous glass nozzle instead of a single-jet nozzle to disperse incoming airflow over a greater area. The collection efficiency of an SKC fritted impinger with a fritted nozzle pore size of 170-220 μm was evaluated by Miljevic et al. to be between 35-80%, depending on the particle size capture), for ultrafine (d<100 nm) particles.[24] They observed that the collection efficiency of ultrafine particles was greater in the fritted impinger than in single-jet impingers, although up to 60% of particles was captured in the coarse (100-160 μm) fritted nozzle instead of in the liquid. The authors recommended employing sonication after collection to displace particles in the nozzle into the liquid, although this practice may alter particle morphology if agglomerates had been collected.

The objective of this work was to develop a personal sampling method to quantify the concentration of ultrafine CNC with an efficiency that mimics deposition in the human respiratory system. A plastic impinger was used, as it solves many of the issues that glass impingers present when worn by a worker, such as fragility in an industrial environment. A nozzle that allows the impinger to collect at an efficiency that models nanoparticle deposition in the human respiratory tract following nanoparticulate matter (NPM) criterion[25] was designed. Methods for quantifying the amount of CNCs in an air sample collected with an impinger were explored. CNCs were tagged

with rhodamine b and concentration is quantified using UV-vis. Dynamic light scattering and electron microscopy were used to determine size and morphology of CNCs in solution.

METHODS

Impingers

Initially, we tested two common glass impingers, a single-jet glass midget impinger (Cat No. 225-36-1, SKC, Eighty-Four, PA) followed by a fritted glass midget impinger (Cat No. 225-36-2, SKC, Eighty-Four, PA). To improve collection efficiency, the final impinger personal setup consisted of two 60-mL plastic (perfluoroalkoxy alkane) impingers (Models 201-060-12-033-36 and 201-060-12-033-37, Savillex Eden Prairie, MN) in series, the first of which contains a 3-D printed nozzle, while the second is empty except for a piece of tubing from the inlet that extends to 1 cm from the bottom. This second impinger is meant to capture droplets that escape the first impinger (**Figure 1A**). To improve the collection of particles in the first impinger by diffusion, a nozzle was designed with 90 1-mm holes to disperse airflow over a relatively large surface area (**Figures 1B and C**). This design is analogous to the nozzle used in a fritted glass impinger but the holes are larger. The nozzle was 3-D printed using Stratasys VeroWhite filament. The impinger with the nozzle was filled with 35 mL of deionized water, a greater volume than what common glass midget impingers can hold.

Collection Efficiency Tests

The experimental setup shown in **Figure 2** was used to determine the collection efficiency of the impingers. Dry and particle-free air was supplied to a nebulizer (HEART Continuous

Nebulizer, Westmed, Inc., Tuscon, AZ) and a dilution line. Flow throughout the system was regulated using three mass flow controllers (MFC; MPC20, Porter Instrument, Hatfield, PA). A solution of 11.8 wt% CNCs (see **Table 2**, unmodified CNCs for dimensions) in water (University of Maine Process Development Center, Orono, ME) was diluted to 30 mg/mL with deionized water and aerosolized with the nebulizer after one hour of bath sonication. The aerosol was passed through an ^{85}Kr neutralizer (3054, TSI, Shoreview, MN) to remove excess particle charges and a diffusion dryer containing silica gel to remove excess aerosol moisture. Collection time for efficiency tests was 10 hours for all runs.

Particle number concentration by size was measured using a scanning mobility particle sizer (SMPS; 3938, TSI, Shoreview, MN) comprised of an electrostatic classifier (3082, TSI, Shoreview, MN), a neutralizer (3088, TSI, Shoreview, MN), a condensation particle counter (3788, TSI, Shoreview, MN), and a long differential mobility analyzer (3081A, TSI, Shoreview, MN). After exiting the dilution chamber, a three-way valve was used to route the test aerosol either directly to the SMPS ("upstream") or through the impingers followed by the SMPS ("downstream"). A vacuum pump controlled via the third MFC was used to pull sampled air at a total of 2.5 L/min in combination with the SMPS (0.3 L/min) at the inlet of the leading impinger and through the upstream line. This MFC was adjusted for each sample to account for differences in pressure in the upstream and downstream configuration.

For each particle bin size ranging from 15 nm to 615 nm mobility diameter (includes >99.7% of all CNC sizes), collection efficiency was calculated as shown in Equation 1. Measurements were alternated between upstream and downstream, where C_{down} is the average of the downstream measurements and C_{up} is the average of the upstream SMPS measurements:

$$CE = 1 - \frac{C_{down}}{C_{up}} \quad \text{(Eq. 1)}$$

Initially, the collection efficiency of the plastic impinger method was compared to that of the SKC single-jet glass midget impinger and SKC fritted glass midget impinger. The comparison used the same set up (**Figure 2**) for each of the studies. For the final impinger design, calculated collection efficiency values were adjusted theoretically (based on previous studies using the same sampler) for the impactor (d_{50}=300 nm) and cyclone stage of the Nanoparticle Respiratory Deposition (NRD) Sampler (Zefon International, Ocala, FL) following Park *et al*. 2015.[26] The NRD impactor and cyclone stage were used with the impingers to prevent collection of large particles that may complicate analysis. Adjustment of collection efficiency accounts for these large particles caught in the NRD sampler. Impactor values and NPM criterion values were calculated with a shape factor of 1.43 [27] and a density of 1.6 g/cm^3.[28] This shape factor is for a cylinder with a length-to-width ratio of 10:1, similar to the needle-like shape of individual CNCs. The adjusted impinger *CE* curve was then compared to the target NPM curve using the coefficient of determination, R^2, calculated as:

$$R^2 = 1 - \frac{\Sigma(CE-NPM)^2}{\Sigma\left(CE-Average(CE)\right)^2} \quad \text{(Eq. 2)}$$

An R^2 value of greater than 0.90 was chosen as the target value for the proposed impinger method. Upper and lower confidence intervals were also calculated following O'Shaughnessy and Schmoll 2013 [29] to determine the certainty of measurements by particle size.

Rhodamine-B Tagging Process

Tagging of CNCs using RBITC was accomplished with a method modified from Haghpanah, et al.[30] Briefly, 2 g CNCs (U.S. Forest Products Laboratory, hydrolyzed from wood using sulfuric acid) were dispersed in 150 mL dimethyl formamide (DMF, Fisher Scientific, HPLC grade). To

this, 0.09 g (0.03 mol eq per glucose unit in cellulose) of rhodamine b isothiocyanate (RBITC, Sigma Aldrich, BioReagent, mixed isomers grade) and 1 drop of dibutyltin dilaurate (DBTDL, Sigma Aldrich, 95% pure) were added. The mixture was heated to 100 °C overnight under nitrogen, then allowed to cool. DMF and excess rhodamine were removed from tagged CNCs (RhB-CNCs) via dialysis (Fisher, MWCO 12,000). **Figure 3** shows the reaction scheme for RBITC attachment to CNCs.

Extent of Labeling Characterization

Characterizing the extent of labeling for each batch of RhB-CNCs is necessary in order to accurately measure the concentration of RhB-CNCs in water using UV-vis. First, a calibration of rhodamine b (Sigma Aldrich, ≥95%, HPLC grade) in water was established using UV-vis spectrophotometry (Agilent Cary 60 UV-vis, Santa Clara, CA). Then, a calibration of each batch of RhB-CNCs was created and amount of rhodamine attached to the CNCs was calculated.

Transmission Electron Microscopy

TEM (JEOL 2100, Peabody, MA) was used to image CNCs suspended in aqueous. Samples were prepared on silicon monoxide/Formvar-coated copper grids (purchased from Ted Pella) using the final protocol formulated by Stinson-Bagby, et al.[31] Briefly, a droplet of suspended CNCs (0.01 wt% in DI-water) was mixed with 0.01 wt% bovine serum albumin solution (lyophilized powder, ≥96%, agarose gel electrophoresis grade) in a 1:1 volumetric ratio. The CNC/BSA solution was then dropped onto a grid and allowed to settle for at least one minute. A drop of NanoVan® stain (methylamine vanadate, purchased from Nanoprobes, Inc.) was then dropped on top of the CNC

droplet and allowed to stain for 15-30 seconds. The grid was then dunked in DI-water and allowed to dry for at least 12 hours at room temperature before imaging.

CNC Particle Size

Hydrodynamic diameter of CNCs in suspension was confirmed using the dynamic light scattering method on a Malvern Zetasizer Nano-ZS (Westborough, MA). Samples were measured without further dilution before and after aerosolization to determine if CNCs were agglomerating and what sizes were collected using the impinger.

RhB-CNC Sample Collection

RhB-CNCs were collected using the final double-impinger setup with the first impinger having the 3D-printed nozzle. Tagged CNCs were used to determine the concentration of CNCs in the impinger liquid, as current analytical methods cannot accurately quantify untagged CNCs. Collection was performed identically to the CE tests with a few minor changes. The concentration of the RhB-CNC solution used in nebulizer was 0.7 mg/mL and the collection time was 10 hours. A smaller dilution chamber was substituted for the larger chamber used in the collection efficiency experiments. For this test, 30 mL of water was used in the impinger instead of 35 mL to minimize the already low amount of water that would exit the first impinger during a long sampling period. Particle mass concentrations were measured by the SMPS at the start and end of each 10-hour period to compare to mass concentration values calculated from UV-Vis results.

In order to quantify amount of RhB-CNCs collected in the impinger liquid, samples were measured by UV-vis without further modification. The absorption peak was used to back-calculate

the concentration of RhB-CNCs in solution using calibration curves for rhodamine b and RhB batch-specific calibration curves.

RESULTS AND DISCUSSION

Impinger CNC Collection

Figure 4a shows the unadjusted collection efficiency by size (i.e., collection efficiency without theoretical correction for the NRD impactor applied) of the plastic impinger method compared to other commercial impingers used for air sampling. The targeted NPM curve, which models the deposition in the human respiratory tract, is added to the particle mobility diameter to map how closely the impinger set up may be able to represent how CNCs will deposit in the lungs. The unadjusted collection efficiency of the plastic impinger method was closer to the target NPM curve than the SKC glass single-jet midget impinger at 2.0 L/min, which was used to collect preliminary data for this project, and the SKC glass fritted midget impinger at 2.5 L/min, which was the model for the multi-holed design of the plastic impinger nozzle. The increased collection efficiency of the plastic impinger method can be attributed to the dispersion of air over larger contact area afforded by the holes in the first impinger nozzle and the increased volume of water compared to what commonly used glass impingers can hold. The plastic impinger is taller and therefore, allows more time for particles smaller than 100 nm to diffuse from bubbles and be collected in the sampler. The lowest efficiency of the plastic impinger method was observed between 200 and 300 nm, as the mechanisms of impaction and diffusion are not dominant for particles in that size range.[24] While the plastic impinger is taller than the glass impinger, it is not much bulkier and will not interfere with workers who will potentially be wearing the impinger.

The adjusted collection efficiency by size, NPM curve, and the size distribution of CNCs are shown in **Figure 4b**. Size distribution is added for reference. The geometric mean diameter of aerosolized CNCs was 164 ± 5 nm. The size of aerosolized CNCs is likely due to agglomeration in air or other potential artifacts present in SMPS characterization of high-aspect-ratio particles.[32] The collection efficiency of the plastic impinger method was evaluated against the NPM curve. An R^2 value of 0.94 was calculated using Equation 2 for particle sizes between 45 and 600 nm once the data were adjusted for the impactor. As shown by the increasing range in the upper and lower confidence intervals, collection efficiency was highly variable for particles smaller than 50 nm due to low particle counts. While low particle counts may indicate the data is nearing a limit of detection, it is not likely that airborne CNC particles smaller than 50 nm will exist in the workplace, as smaller particles will quickly agglomerate to form particles within or above the effective size range. Thus, the plastic impinger method agrees well with the NPM curve for those sizes of relevance in the workplace.

In this work, we targeted a collection method for the ultrafine fraction of airborne CNC that would deposit in the respiratory tract. The plastic impinger method could be used without the NRD impactor to collect airborne agglomerate CNC. The collection efficiency without the NRD impactor would be similar to that shown in Figure 4a, having a minimum at ~200 nm, increasing for particles smaller than that size due to diffusion, and increasing for particles larger than that size due to impaction. This shape is similar to the deposition of particles in all regions of the human respiratory tract.[33] In further work, we could modify the number and size of the holes in the nozzle of the first plastic impinger to more closely mimic deposition in all regions of the respiratory tract.

CNC Labeling with Rhodamine B

CNCs were successfully labeled with rhodamine B. UV-vis shows a shift in the absorption peak after labeling, indicating rhodamine b attachment. The absorption peak of RhB alone is at 554 nm but shifts to between 562-566 nm after attachment to CNCs. Typical UV-vis absorption spectra and calibration curves of rhodamine b and RhB-CNCs are shown in **Figure 5**. Using these calibrations, extent of rhodamine b labeling was calculated using Equation 3. It was found that 2.2 µg RhB/mg RhB-CNC was attached during labeling. This is similar to the amount of labeling Haghpanah et al. achieved (12.36 mmol/kg, or 4.8 µg Fluorescein/mg Fluorescein-CNC).[30] Haghpanah used three times as much fluorescein compared to the rhodamine used here (molar basis), which could explain why more fluorescein was attached to their CNCs. When testing UV-vis as a method for determining concentration of RhB-CNCs, it was found that an error up to about 11% could be expected, shown in **Table 1**.

$$\frac{Absorbance\ of\ R{-}CNCs}{Slope\ of\ RhB\ Calibration} * \frac{1}{Concentration\ of\ R{-}CNCs} = \frac{Mass\ of\ RhB}{Mass\ of\ R{-}CNCs} \quad \text{(Eq. 3)}$$

After labeling, RhB-CNCs in suspension can be observed as a pink liquid and dried RhB-CNCs as a fluffy, pink powder. In comparison, unmodified CNCs appear as a clear or slightly blueish-white liquid for a CNC suspension and a white powder for dry CNCs TEM images showed no observable difference in size or morphology of CNCs after labeling, as seen in **Figure 6** and **Table 2**. Size was measured from at least 50 individual CNCs in 3-5 TEM images using ImageJ software. CNC size and aspect ratio are similar to literature values found for wood-based CNCs.[34-35]

Collection of RhB-CNC for DLS and UV-Vis Analysis

The collected samples were analyzed using DLS to assure that CNCs are present in the solutions. **Figure 7** shows DLS of RhB-CNCs before and after collection by impinger. Comparing RhB-CNCs before and after collection, there appears to be a shift in particle size to be larger after collection. This is likely due the formation of agglomerates upstream of the impingers. **Figure 7** shows the size distributions in the impinger solution after collection. The size distributions of all samples are similar with no significant differences between them. The hydrodynamic diameter of the CNCs both pre- and post-impinger samples as measured by DLS was 78±15. This is similar in size to the CNCs measured via TEM (**Table 2**).

UV-vis was then used to quantify the concentration of RhB-CNCs collected in the samples. **Figure 8** shows the UV-vis absorption of the three RhB-CNC samples collected with the impinger method over a 10-hour period. Some scattering of the aerosolized RhB-CNC was present, which is similar to scattering observed in CNC-only absorbance curve in **Figure 5**, and can be seen as the gradually sloping curve that peaks around 400 nm. The scattering was removed before peak absorbance at 554 nm was taken for CNC concentration calculations. **Table 3** shows that airborne concentrations calculated from UV-Vis results do not agree with the actual aerosolized concentrations given by the SMPS. This may be due to rhodamine degradation or detachment of rhodamine from CNCs during the aerosolization process. Another possibility is that there may have been some residual rhodamine b not removed by dialysis that may have skewed the calibration. Moreover, the ratio of scattering due to CNC particles compared with UV-vis peak from rhodamine content is greater in post-impinger samples compared with the pre-impinger sample, which suggests some rhodamine detachment. The UV-vis peak in post-impinger samples also shifts closer to 554 nm, which is the peak of standalone rhodamine b. Nevertheless, UV-vis helps confirm the impinger collection method as a proof-of-concept device. Because of the

discrepancy between UV-vis and SMPS measuring capabilities, SMPS was used to calculate collection efficiency.

CONCLUSIONS

The plastic impinger method presented here collected airborne ultrafine CNC with an efficiency that mimics deposition in the human respiratory system. This collection efficiency is greater than commercially available impingers for relevant particle sizes. SMPS is a reliable method for determining the concentration of RhB-CNCs in solution after aerosolization and collection via impinger, and UV-vis supports the data observed using SMPS. TEM and DLS can work together to confirm particles collected are in fact CNCs. Further work includes finding a method of quantifying unlabeled CNCs in order to be more useful in an industrial environment.

ACKNOWLEDGEMENTS

The authors acknowledge the assistance of Kelly Stinson-Bagby for imaging samples via TEM and use of the facilities at the Nanoscale Characterization and Fabrication Laboratory (NCFL) at Virginia Polytechnic Institute. P3Nano provided funding for the research.

REFERENCES

FIGURES

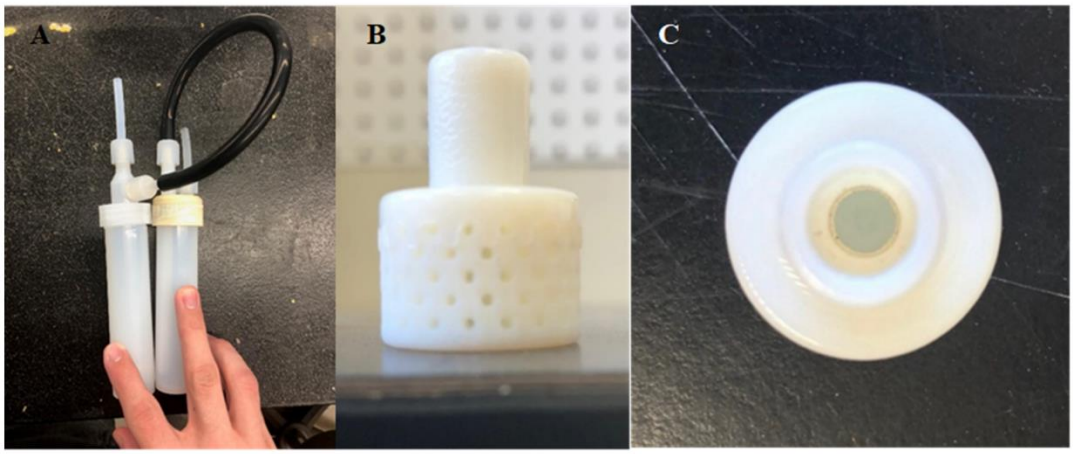

Figure 1. Pictures of 2 plastic impingers (A) and a 3D-printed impinger nozzle used in first impinger (B, C).

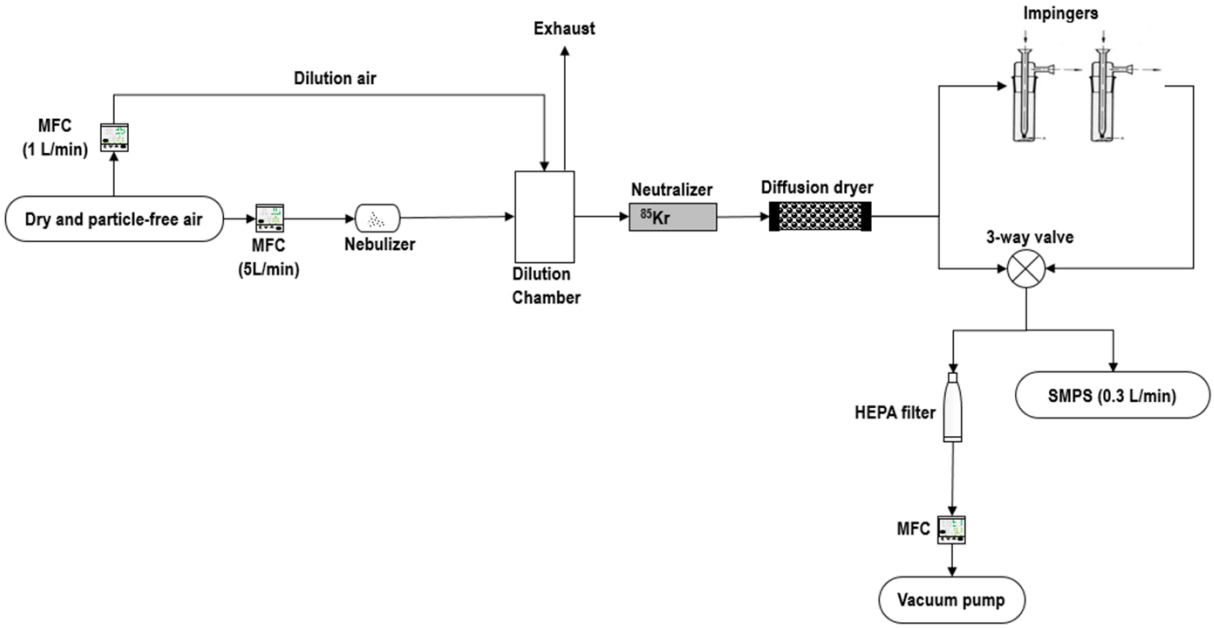

Figure 2. Experimental setup for aerosolization, measurement, and collection of CNC.

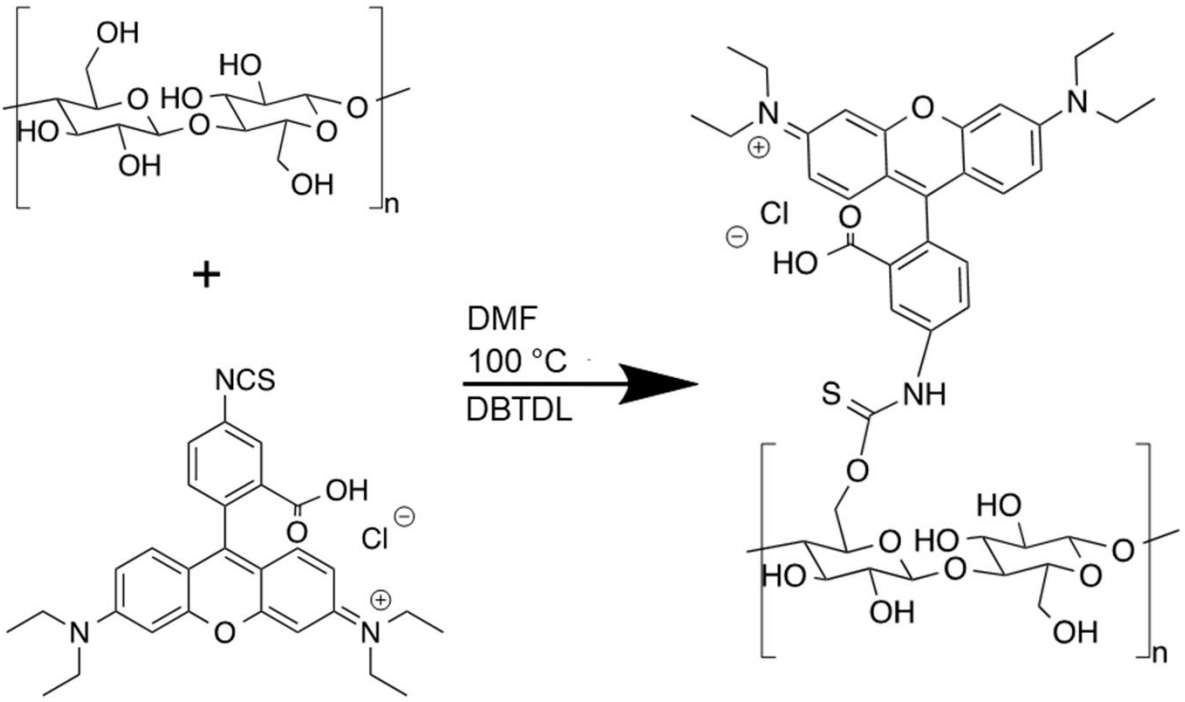

Figure 3. Reaction scheme for RBITC attachment to CNCs.

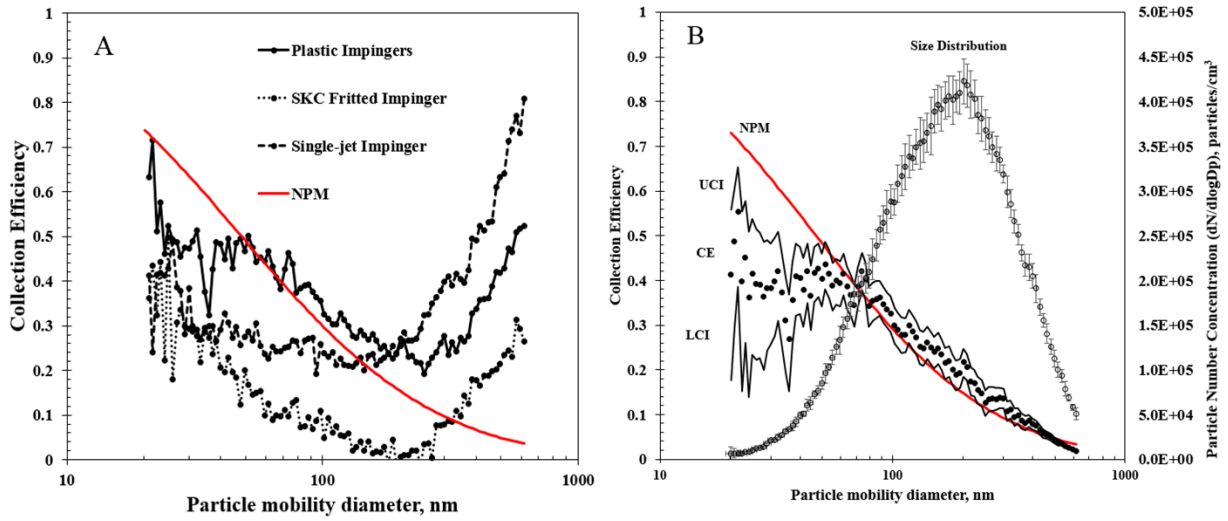

Figure 4. (a) Unadjusted collection efficiency of plastic impinger method, SKC fritted impinger, and SKC single-jet impinger. (b) Impactor-adjusted collection efficiency of impinger method compared to target NPM curve. Size distribution indicated by secondary y-axis. Upper (UCI) and lower (LCI) confidence intervals indicate variance in collection efficiency measurements. Target NPM curve shown for comparison to final design criteria.

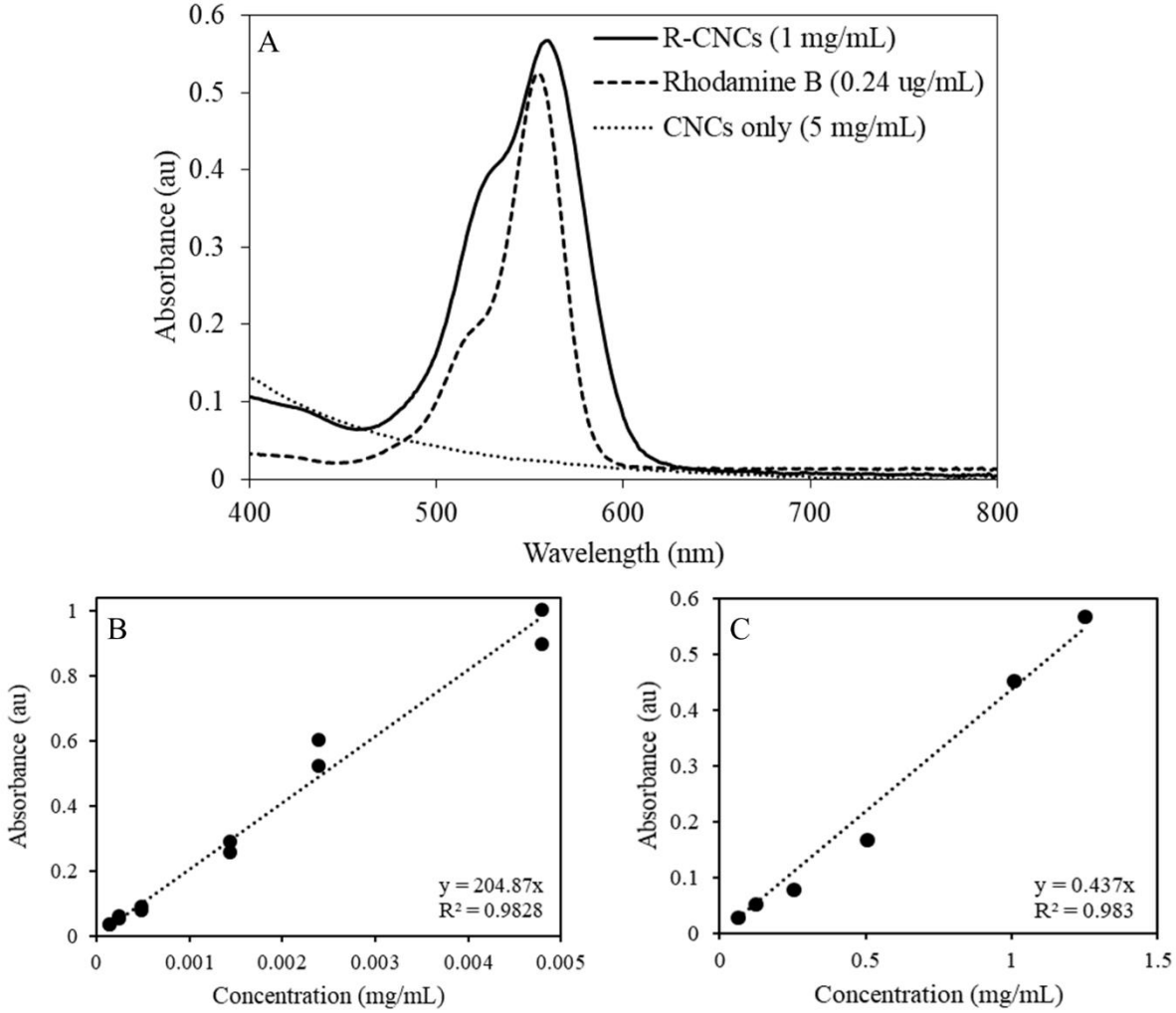

Figure 5. Extent of labeling of RhB-CNCs using A) UV-vis of CNCs, rhodamine b, and RhB-CNCs in water and calibration curves of B) rhodamine b in water and C) RhB-CNCs in water.

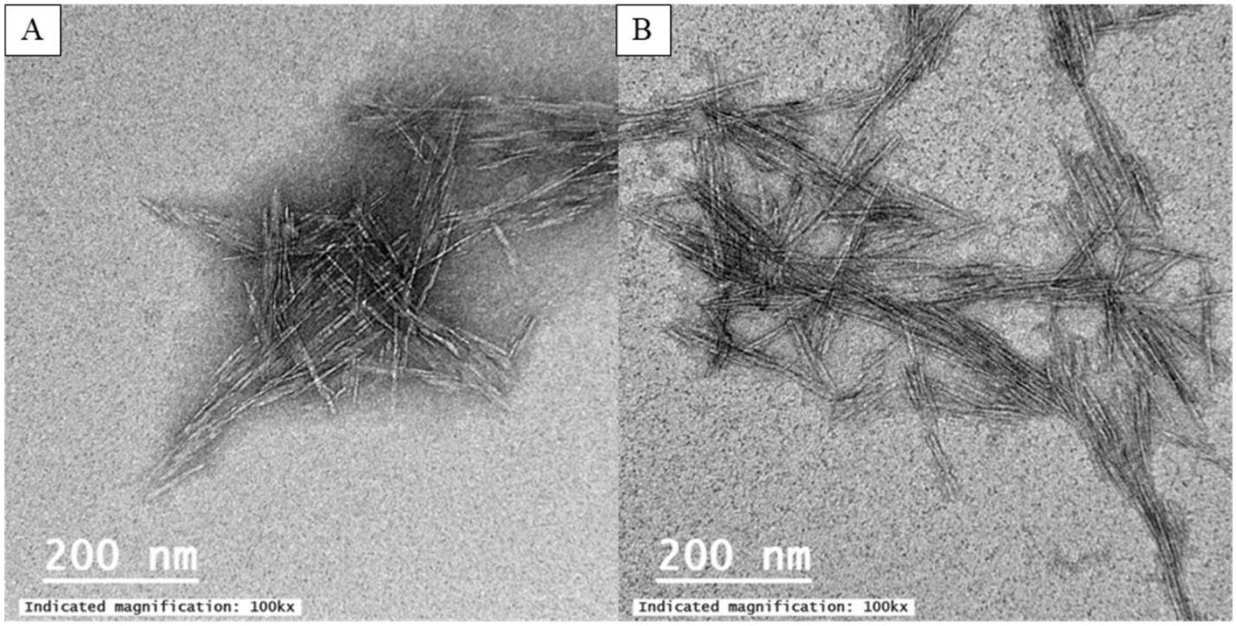

Figure 6. TEM images of CNCs before (A) and after (B) rhodamine modification.

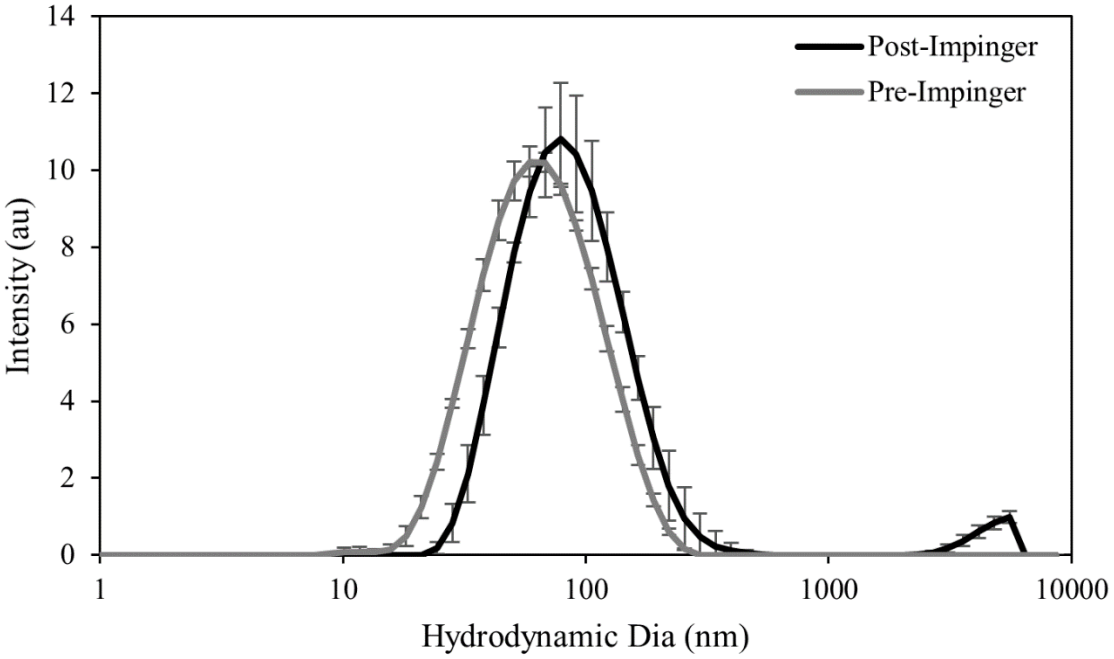

Figure 7. Particle size of RhB-CNCs as measured by DLS.

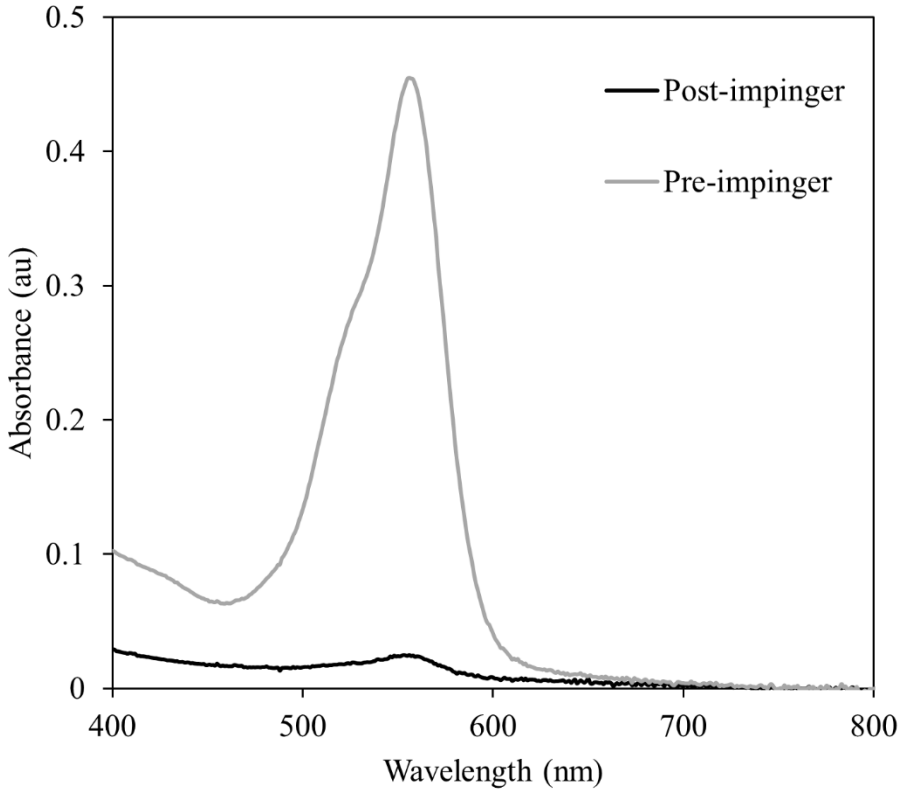

Figure 8. UV-vis absorbance of rhodamine on CNCs from impinger collection.

TABLES

Table 1. Absorbance and concentration of RhB-CNCs

Known Concentration (mg/mL)	Absorbance	Calculated RhB Concentration (mg/mL)	Converted to CNC Concentration (mg/mL)	Deviance between Known and Calculated Concentration (%)
1.25	0.566	0.00276	1.25	0.0961
0.35	0.163	0.000795	0.360	2.96
0.125	0.0504	0.000246	0.111	-10.9
0.0625	0.0282	0.000138	0.0624	-0.0939

Table 2. Size of CNCs measured from TEM images.

	Length (nm)	**Width (nm)**	**Aspect Ratio**
Before Modification	84.5±32.9	5.5±1.4	15.3
After Modification	97.1±39.3	5.4±1.3	18.0

Table 3. Comparison of aerosolized RhB-CNC mass concentrations obtained by UV-Vis analysis and SMPS. SMPS represents expected values, while UV-Vis results are calculated from actual UV absorbance of sample. SMPS results are presented as ranges due to changes in nebulization over time.

Sample	UV-Vis C_{air} ($\mu g/m^3$)	SMPS C_{air} ($\mu g/m^3$)
1	571	1042-3292
2	406	3986-4539
3	355	2828-4059

1. Eichhorn, S. J.; Dufresne, A.; Aranguren, M.; Marcovich, N. E.; Capadona, J. R.; Rowan, S. J.; Weder, C.; Thielemans, W.; Roman, M.; Renneckar, S.; Gindl, W.; Veigel, S.; Keckes, J.; Yano, H.; Abe, K.; Nogi, M.; Nakagaito, A. N.; Mangalam, A.; Simonsen, J.; Benight, A. S.; Bismarck, A.; Berglund, L. A.; Peijs, T., Review: current international research into cellulose nanofibres and nanocomposites. *Journal of Materials Science* **2010,** *45* (1), 1-33.
2. Samir, M.; Alloin, F.; Dufresne, A., Review of recent research into cellulosic whiskers, their properties and their application in nanocomposite field. *Biomacromolecules* **2005,** *6* (2), 612-626.
3. Paakko, M.; Ankerfors, M.; Kosonen, H.; Nykanen, A.; Ahola, S.; Osterberg, M.; Ruokolainen, J.; Laine, J.; Larsson, P. T.; Ikkala, O.; Lindstrom, T., Enzymatic hydrolysis combined with mechanical shearing and high-pressure homogenization for nanoscale cellulose fibrils and strong gels. *Biomacromolecules* **2007,** *8* (6), 1934-1941.
4. Paakko, M.; Vapaavuori, J.; Silvennoinen, R.; Kosonen, H.; Ankerfors, M.; Lindstrom, T.; Berglund, L. A.; Ikkala, O., Long and entangled native cellulose I nanofibers allow flexible aerogels and hierarchically porous templates for functionalities. *Soft Matter* **2008,** *4* (12), 2492-2499.
5. Capadona, J. R.; Shanmuganathan, K.; Triftschuh, S.; Seidel, S.; Rowan, S. J.; Weder, C., Polymer Nanocomposites with Nanowhiskers Isolated from Microcrystalline Cellulose. *Biomacromolecules* **2009,** *10* (4), 712-716.
6. Hult, E. L.; Iversen, T.; Sugiyama, J., Characterization of the supermolecular structure of cellulose in wood pulp fibres. *Cellulose* **2003,** *10* (2), 103-110.

7. Heyder, J., Deposition of inhaled particles in the human respiratory tract and consequences for regional targeting in respiratory drug delivery. *Proc Am Thorac Soc* **2004,** *1* (4), 315-20.
8. Oberdörster, G.; Sharp, Z.; Atudorei, V.; Elder, A.; Gelein, R.; Kreyling, W.; Cox, C., Translocation of inhaled ultrafine particles to the brain. *Inhal Toxicol* **2004,** *16* (6-7), 437-45.
9. Dong, J.; Shang, Y.; Inthavong, K.; Tu, J.; Chen, R.; Bai, R.; Wang, D.; Chen, C., Comparative Numerical Modeling of Inhaled Nanoparticle Deposition in Human and Rat Nasal Cavities. *Toxicol Sci* **2016,** *152* (2), 284-96.
10. Foster, E. J.; Moon, R. J.; Agarwal, U. P.; Bortner, M. J.; Bras, J.; Camarero-Espinosa, S.; Chan, K. J.; Clift, M. J. D.; Cranston, E. D.; Eichhorn, S. J.; Fox, D. M.; Hamad, W. Y.; Heux, L.; Jean, B.; Korey, M.; Nieh, W.; Ong, K. J.; Reid, M. S.; Renneckar, S.; Roberts, R.; Shatkin, J. A.; Simonsen, J.; Stinson-Bagby, K.; Wanasekara, N.; Youngblood, J., Current characterization methods for cellulose nanomaterials. *Chem Soc Rev* **2018,** *47* (8), 2609-2679.
11. Yanamala, N.; Farcas, M. T.; Hatfield, M. K.; Kisin, E. R.; Kagan, V. E.; Geraci, C. L.; Shvedova, A. A., In Vivo Evaluation of the Pulmonary Toxicity of Cellulose Nanocrystals: A Renewable and Sustainable Nanomaterial of the Future. *ACS Sustainable Chemistry & Engineering* **2014**.
12. Du, L.; Arnholt, K.; Ripp, S.; Sayler, G.; Wang, S.; Liang, C.; Wang, J.; Zhuang, J., Biological toxicity of cellulose nanocrystals (CNCs) against the luxCDABE-based bioluminescent bioreporter Escherichia coli 652T7. *Ecotoxicology* **2015,** *24* (10), 2049-53.
13. Clift, M. J. D.; Foster, E. J.; Vanhecke, D.; Studer, D.; Wick, P.; Gehr, P.; Rothen-Rutishauser, B.; Weder, C., Investigating the Interaction of Cellulose Nanofibers Derived from Cotton with a Sophisticated 3D Human Lung Cell Coculture. *Biomacromolecules* **2011**.
14. Seehra, M.; Stefaniak, A., X-ray diffraction as a measurement tool for biodegradability of cellulose nanocrystals. In *Production and Applications of Cellulose Nanomaterials*, Postek, M. T.; Moon, R. J.; Rudie, A.; Bilodeau, M., Eds. TAPPI PRESS: Peachtree Corners, GA, 2013.
15. Roman, M., Toxicity of Cellulose Nanocrystals: A Review. *Industrial Biotechnology* **2015,** *11* (1), 25-33.
16. Vartiainen, J.; Pöhler, T.; Sirola, K.; Pylkkänen, L.; Alenius, H.; Hokkinen, J.; Tapper, U.; Lahtinen, P.; Kapanen, A.; Putkisto, K.; Hiekkataipale, P.; Eronen, P.; Ruokolainen, J.; Laukkanen, A., Health and environmental safety aspects of friction grinding and spray drying of microfibrillated cellulose. *Cellulose* **2011,** *18* (3), 775-786.
17. Martinez, K.; Eastlake, A.; Rudie, A.; Geracis, C., Occupational Exposure Characterization during the manufacture of cellulose nanomaterials. In *Production and Applications of Cellulose Nanomaterials*, Potstek, M.; Moon, R.; Rudie, A.; Bilodeau, M., Eds. TAPPI PRESS: Peachtree Corners, GA. , 2013; pp 61-66.
18. Shatkin, J. A.; Kim, B., Cellulose nanomaterials: life cycle risk assessment, and environmental health and safety roadmap. *Environmental Science: Nano* **2015,** *2* (5), 477-499.
19. Lin, X., et al., Effect of sampling time on the collection efficiency of all-glass impingers. *American Industrial Hygiene Association Journal* **1997,** *58* (7), 480-488.
20. Grinshpun, S. A.; Willeke, K.; Ulevicius, V.; Juozaitis, A.; Terzieva, S.; Donnelly, J.; Stelma, G. N.; Brenner, K. P., Effect of Impaction, Bounce and Reaerosolization on the Collection Efficiency of Impingers. *Aerosol Science and Technology* **1997,** *26* (4), 326-342.
21. Spanne, M.; Grzybowski, P.; Bohgard, M., Collection Efficiency for Submicron Particles of a Commonly Used Impinger. *American Industrial Hygiene Association Journal* **1999,** *60* (4), 540-544.

22. Wei, Z.; Rosario, R. C.; Montoya, L. D., Collection efficiency of a midget impinger for nanoparticles in the range of 3–100 nm. *Atmospheric Environment* **2010,** *44* (6), 872-876.
23. Hogan, C. J.; Kettleson, E. M.; Lee, M. H.; Ramaswami, B.; Angenent, L. T.; Biswas, P., Sampling methodologies and dosage assessment techniques for submicrometre and ultrafine virus aerosol particles. *Journal of Applied Microbiology* **2005,** *99* (6), 1422-1434.
24. Miljevic, B.; Modini, R. L.; Bottle, S. E.; Ristovski, Z. D., On the efficiency of impingers with fritted nozzle tip for collection of ultrafine particles. *Atmospheric Environment* **2009,** *43* (6), 1372-1376.
25. Cena, L. G.; Anthony, R.; Peters, T. M., A Personal Nanoparticle Respiratory Deposition (NRD) Sampler. *Environmental Science & Technology* **2011,** *45*, 6483-6490.
26. Park, J. H.; Mudunkotuwa, I. A.; Mines, L. W. D.; Anthony, T. R.; Grassian, V. H.; Peters, T. M., A Granular Bed for Use in a Nanoparticle Respiratory Deposition Sampler. *Aerosol Science and Technology* **2015,** *49* (3), 179-187.
27. Hinds, W. C., *Aerosol technology: properties, behavior, and measurement of airborne particles*. Wiley: 1999.
28. Dufresne, A., *Nanocellulose*. De Gruyter: Berlin/Boston, GERMANY, 2013.
29. O'Shaughnessy, P. T.; Schmoll, L. H., Particle Count Statistics Applied to the Penetration of a Filter Challenged with Nanoparticles. *Aerosol science and technology : the journal of the American Association for Aerosol Research* **2013,** *47* (6), 616-625.
30. Haghpanah, J. S.; Tu, R.; Da Silva, S.; Yan, D.; Mueller, S.; Weder, C.; Foster, E. J.; Sacui, I.; Gilman, J. W.; Montclare, J. K., Bionanocomposites: differential effects of cellulose nanocrystals on protein diblock copolymers. *Biomacromolecules* **2013,** *14* (12), 4360-7.
31. Stinson-Bagby, K. L.; Roberts, R.; Foster, E. J., Effective cellulose nanocrystal imaging using transmission electron microscopy. *Carbohydr Polym* **2018,** *186*, 429-438.
32. Chen, B. T.; Schwegler-Berry, D.; Cumpston, A.; Cumpston, J.; Friend, S.; Stone, S.; Keane, M., Performance of a scanning mobility particle sizer in measuring diverse types of airborne nanoparticles: Multi-walled carbon nanotubes, welding fumes, and titanium dioxide spray. *J Occup Environ Hyg* **2016,** *13* (7), 501-18.
33. ICRP, Human respiratory tract model for radiological protection. Publication 66, Pergamon Press, Oxford, UK. *Ann. ICRP* **1994,** *24*, 272.
34. Moon, R. J.; Martini, A.; Nairn, J.; Simonsen, J.; Youngblood, J., Cellulose nanomaterials review: structure, properties and nanocomposites. *Chem Soc Rev* **2011,** *40* (7), 3941-94.
35. Hosseinidoust, Z.; Alam, M. N.; Sim, G.; Tufenkji, N.; van de Ven, T. G., Cellulose nanocrystals with tunable surface charge for nanomedicine. *Nanoscale* **2015,** *7* (40), 16647-57.

Chapter 5

Development of PLGA Nanoparticles for Sustained Release of a Connexin43 Mimetic Peptide to Target Glioblastoma Cells

Glioblastoma becomes resistant to chemotherapy quickly, however αCT1 is a new peptide drug that keeps glioblastoma cells sensitive to chemotherapy, specifically temozolomide. Unfortunately, the peptide is metabolized by the body within about 24 hours, which is not conducive to long term treatments in the brain. This chapter discusses the development of nanoparticles to encapsulate αCT1 in order to release the drug over several weeks. The method of encapsulation is double emulsion-solvent evaporation. Particles were first developed using the model drug rhodamine B, then αCT1 was introduced. αCT1 release from particles was observed over three weeks. Effect of toxicity on cells was also observed. This chapter uses characterization methods for nanoparticles from previous chapters. This chapter discovers the largest challenges with drug encapsulation for this αCT1 particle system, providing a foundation for the next chapter.

In this chapter, all data were collected and analyzed by myself except ELISA assays and cellular studies were performed by Dr. Samy Lamouille. The peptide drug αCT1 was graciously provided by Dr. Christina L. Grek and Dr. Gautam S. Ghatnekar. Dr. Zhi Sheng and Dr. Robert G. Gourdie gave input into nanoparticle needs for glioblastoma treatment. Dr. E. Johan Foster supported the research and experimentation. The manuscript was drafted by myself, except sections discussing ELISA assay methodology and cellular studies' methodology and results. Remaining authors later edited the chapter. This chapter is currently under review in Materials Science and Engineering: C for publication, and formatting for the chapter is as submitted for publication.

Development of PLGA nanoparticles for sustained release of a Connexin43 mimetic peptide to target glioblastoma cells
Rose Roberts, Christina L. Grek, Gautam S. Ghatnekar, Zhi Sheng, Robert G. Gourdie, Samy Lamouille, E. Johan Foster
Materials Science and Engineering: C, manuscript in review.

Development of PLGA nanoparticles for sustained release of a Connexin43 mimetic peptide to target glioblastoma cells

Rose Roberts[a], Christina L. Grek[b], Gautam S. Ghatnekar[b], Zhi Sheng[c,d,e], Robert G. Gourdie[c,d,e,f,g,h] Samy Lamouille[c,i], E. Johan Foster[a]

[a]Virginia Tech, Macromolecule Innovation Institute and Materials Science and Engineering Department, Blacksburg, VA;
[b]FirstString Research, Inc., Mount Pleasant, SC;
[c]Virginia Tech Carilion Research Institute and School of Medicine, Roanoke, VA;
[d]Faculty of Health Science, Virginia Tech, Blacksburg, VA;
[e]Department of Internal Medicine, Virginia Tech Carilion School of Medicine, Roanoke, VA;
[f]Virginia Tech-Wake Forest University School of Biomedical Engineering and Sciences, Blacksburg, VA;
[g]Department of Emergency Medicine, Virginia Tech Carilion School of Medicine, Roanoke, VA;
[h]Virginia Tech Carilion Research Institute, Center for Heart and Regenerative Medicine Research, Roanoke, VA.
[i]Department of Biological Sciences, Virginia Polytechnic Institute and State University, Blacksburg, Virginia

Co-corresponding Authors (include phone #, email, and postal address):
Samy Lamouille, 540-526-3302, lamouils@vtc.vt.edu, R3001, 2 Riverside Circle Roanoke, VA 24016
E. Johan Foster, (540) 231-8165, johanf@vt.edu, 203 Holden Hall, 445 Old Turner Street, Blacksburg, VA 24061

Address where work was completed: 312 Holden Hall, 445 Old Turner St., Virginia Tech, Blacksburg, VA 24061

Funding**:** This work was supported by the U.S. Endowment for Forestry & Communities, Inc. P3Nano to Johan Foster at Virginia Tech, National Institutes of Health [R41 CA217503 to Samy Lamouille at Acomhal Research, R43 CA195937 to FirstString Research, R21 CA216768 to Zhi Sheng, and RO1 HL56728 to Rob Gourdie]. FirstString Research graciously provided the peptide αCT1.

Declarations of interest: None

Abstract

Effective therapeutic delivery of peptide and protein drugs is challenged by short *in vivo* half-lives due to rapid degradation. Sustained release formulations of αCT1, a 25 amino acid peptide drug, would afford lower dosing frequency in indications that require long term treatment, such as chronic wounds and cancers. In this study, rhodamine B (RhB) was used as a model drug to develop and optimize a double emulsion-solvent evaporation method of poly(lactic-co-glycolic acid) (PLGA) nanoparticle synthesis. Encapsulation of αCT1 in these nanoparticles (NPs) resulted in a sustained *in vitro* release profile over three weeks, characterized by an initial burst release over the first three days followed by sustained release of up to 73% of total encapsulated drug over the remaining two and a half weeks. NP uptake by glioblastoma stem cells was through endocytosis and RhB and αCT1 were observed in cells after at least 4 days.

Keywords: drug release, αCT1 peptide, glioblastoma, stem cell

Introduction

In vivo susceptibility to physical and chemical alteration (i.e. denaturation, aggregation, oxidation, hydrolysis, etc.) has hindered the therapeutic development of peptides and proteins. Biodegradable nanoparticles offer the opportunity to achieve sustained therapeutic drug delivery in addition to offering drug targeting and reduced off-target side effects.[1-3] Due to their biocompatibility and biodegradability, polymeric nanoparticles, such as poly(lactic-co-glycolic acid) (PLGA) nanoparticles, have been used extensively for controlled release of various drugs, especially small molecules.[4-5] Sustained drug release is especially useful for chronic diseases, such as non-healing ulcers, and other ailments that may take weeks or longer to heal and require

repetitive therapeutic intervention.[5] A polymer nanoparticle release system should thus be ideal for αCT1 (also referred to as αCT1 or ACT1 in publications), a novel synthetic C-terminus connexin43 mimetic peptide drug currently in clinical trials for the treatment of chronic wounds[6-8] and animal trials for the treatment of glioblastoma (brain cancer).[9] In the treatment of chronic wounds, the current treatment paradigm involves multiple topical applications over the course of healing. The development of a sustained release αCT1 formulation could help reduce overall treatment costs and increase patient compliance. The peptide has successfully been encapsulated in previous work using alginate microparticles via an electrospray method, resulting in modest drug release profiles of about 24 hours.[10-11] Given that the therapeutic application of αCT1 may include conveyance within the narrow extracellular spaces of brain tissue (for glioblastoma treatment)[9] or intravenous delivery, a nanoparticle release system may be a preferred mode of drug delivery compared with microparticles or other bulkier release methods.

PLGA is widely used in drug delivery for a variety of applications, including in micro- and nanoparticles to improve vaccinations, cancer treatments, cardiovascular treatments, and regenerative medicine.[2-4] PLGA is useful for controlled-release because it degrades over several weeks by hydrolysis through cleavage of its backbone ester linkages, forming biologically compatible byproducts, lactic acid and glycolic acid, which are readily metabolized by the body through the Krebs cycle and eliminated as carbon dioxide and water.[2, 4] PLGA has also been approved by the FDA as a drug delivery vehicle, streamlining the approval process for drugs that incorporate PLGA in controlled release formulations, such as αCT1.[12] Degradation rates for PLGA can be manipulated to extend from months to years, offering potent opportunity in

sustained peptide release and the reduction of treatment applications and the number of invasive procedures.

Many studies have been successful in encapsulating hydrophilic and hydrophobic drugs using PLGA, especially small molecules, but peptides and proteins can be more challenging to encapsulate, while keeping a minimal particle size.[13-18] While there are several methods to create nanoparticles, one of the most common is the emulsion-solvent evaporation method.[19] The emulsion-solvent evaporation method involves first dissolving the polymer in a volatile, water-immiscible solvent before emulsifying in water with a surfactant, then allowing the solvent to evaporate. Hydrophobic drugs are generally encapsulated via a single emulsion process as described above (o/w), while hydrophilic drugs use a double emulsion (w/o/w) method.[2, 19]

In this study, PLGA nanoparticles were prepared using the emulsion-solvent evaporation method for the encapsulation and controlled release of the synthetic peptide drug αCT1. αCT1 is a hydrophilic drug that is highly soluble in water, so it was anticipated that a double emulsion process would be most appropriate for nanoparticle production. To allow for a more comprehensive investigation, drug loading was also compared with a single emulsion process.

Materials and Methods

General

All purchased materials were used without further purification. PLGA (poly(D,L-lactide-co-glycolide; 7000-17000 MW, 50:50 lactic acid:glycolic acid, acid terminated), PVA (poly(vinyl alcohol); 13000-23000 MW, 87-89% hydrolyzed), rhodamine B (RhB; HPLC grade, ≥95%),

phosphate buffered saline powder (PBS; reconstituted in DI-water; BioPerformance Certified, pH 7.4), sucrose (BioUltra, for molecular biology, ≥99.5% (HPLC)), trehalose (Pharmaceutical Secondary Standard, certified reference material), and bovine serum albumin (BSA; essentially fatty acid free and essentially globulin free, ≥99%, agarose gel electrophoresis) were purchased from Sigma Aldrich. Ethyl acetate (EA; HPLC grade) was purchased from Fisher Scientific. The peptide drug, α–connexin carboxyl-terminal (αCT1) peptide was synthesized by the American Peptide Company (now Bachem; Sunnyvale, CA). The αCT1 peptide corresponds to a short sequence at the Connexin43 C-terminus RPRPDDLEI) linked to an antennapedia internalization sequence (RQPKIWFPNRRKPWKK).

Synthesis of Single Emulsion Particles

Single emulsion nanoparticle (SE-NP) synthesis method was modified from Mathew et al., 2012.[12] Briefly, after dissolving PLGA in EA, 0.1 mg of RhB was added directly to the PLGA solution. The solution was vortexed and then added to 1 mL of 2.5 w/v% solution of PVA in water. The solution was probe sonicated for 2 minutes at 40% amplitude. The solution was immediately added to 50 mL of 0.3 w/v% PVA in water, then was stirred for at least three hours to allow for EA evaporation.

SE-NPs were loaded with rhodamine B to test the difference in amount of drug loaded in the particles between single and double emulsion methods. RhB was used as a model drug for finding trends in drug loading because of its ease in concentration characterization. Furthermore, RhB and αCT1 share similar physiochemical characteristics including a positive overall charge. While the sizes of the molecules are different and could create differences in particle size, trends

in loading and interactions with PLGA should be similar because of their charges. BSA is used to more closely mimic the size of the peptide. While much larger than αCT1 (MW 66.5 kDa compared with 3.5 kDa), it is on the extreme of bulkiness and should easily show trends in particle size during process modifications.

Synthesis of Double Emulsion Particles

The applied synthesis protocol was modified from Mathew et al. and Zhang et al.[12, 18] Briefly, the double emulsion particles (DE-NPs) containing αCT1 (αCT1-NPs) were synthesized at room temperature by first dissolving 0.025 g of PLGA in 1 mL of EA for 30 minutes while vortexing intermittently. 50 µL of a 2 mmol αCT1 solution in water was then added and sonicated using a Qsonica Q55 probe sonicator at 40% amplitude for 2 minutes. The primary emulsion was then immediately added dropwise to 1 mL of 2.5 w/v% solution of PVA in water while vortexing. This mixture was then immediately probe sonicated again at 40% amplitude for 2 minutes. The double emulsion was then transferred to 50 mL of 0.3 w/v% PVA solution in water and stirred for at least three hours to allow for ethyl acetate evaporation. For rhodamine b or BSA nanoparticles (RhB-NPs, BSA-NPs), the same protocol was followed substituting a 2 mmol solution of rhodamine B or BSA in water for the αCT1 solution. Particles to be used in cell culture experiments were sterilized by filtration using Fisherbrand 25mm nylon sterile syringe filters with a 0.2 µm pore size or made in a sterile biosafety cabinet during particle synthesis with all materials sterilized before use. Particles were then washed via the centrifugation method three times to remove excess PVA, frozen at ≤-20 °C, and lyophilized, then stored at -20 °C.

Materials Characterization Methods

Scanning electron microscopy (SEM) was performed at the Nanoscale Characterization and Fabrication Laboratory in Blacksburg, VA using the LEO (Zeiss) field-emission SEM. Analysis of SEM images was completed using ImageJ software. Dynamic light scattering (DLS) and zeta potential were measured using a Malvern Zetasizer Nano-ZS. UV-vis absorbance for rhodamine release studies was measured using a Cary 60 UV-Vis spectrophotometer by Agilent Technologies.

In Vitro Release of Drug from Nanoparticles

Lyophilized nanoparticles were resuspended in 0.01 M PBS solution at 1 mg/mL and incubated at 37 °C for the duration of the release study. At each time point, the particles were centrifuged into a pellet and the supernatant was collected for drug content analysis. The removed supernatant was replaced with the same volume of fresh PBS solution in order to maintain a consistent concentration and the particles were redispersed via bath sonication for 10-15 minutes. Samples of dispersions were taken and analyzed for dynamic light scattering (DLS). SEM samples were prepared by adding a drop of the particle suspension onto silicon wafer pieces taped to an SEM stub for future analysis.

Cell Culture

The human glioblastoma (GBM) cell line SF295 was maintained in Dulbecco's modified Eagle medium (Thermo Scientific) supplemented with 10% fetal bovine serum (Atlas Biologicals, Inc.), streptomycin (100 μg/ml) and penicillin (100 IU/ml). Human GBM stem cells (GSCs) VTC-037, isolated from a GBM patient who received surgery at the Carilion Clinic, as described previously,[9, 20] and LN229/GSC were maintained in Dulbecco's modified Eagle medium

supplemented with Gibco® B-27® Supplements (Thermo Scientific), fibroblast growth factor (ProSpec-Tany TechnoGene Ltd., 20 ng/ml), and epidermal growth factor (ProSpec-Tany TechnoGene Ltd., 20 ng/ml).

Enzyme Linked Immunoassay (ELISA)

To enable peptide tracking in *in vitro* and *in vivo* assays, an amino-terminal biotin tag was added to the αCT1 sequence. The *in vitro* release of biotin-tagged αCT1 was measured by sandwich enzyme linked immunoassay (ELISA) using the OptEIA kit (BD Biosciences). Each well of a Nunc MaxiSorp™ 96-well microplate (Thermo Scientific) was coated with coating buffer containing 1 µg/mL of anti-C-terminus connexin43 antibody (Sigma-Aldrich) and incubated overnight at 4 °C. The wells were then washed before blocking with 1% bovine serum albumin for 2 h at room temperature. Serial dilution of biotin-tagged αCT1 as standards and samples containing biotin-tagged αCT1 collected at different times from the *in vitro* release study were added in the corresponding wells and incubated overnight at 4 °C. The wells were then washed before adding 1 µg/ml Neutravidin-conjugated HRP (Thermo Scientific) for 1 h at room temperature. After washing, 3,3',5,5'-Tetramethylbenzidine (TMB) chromogenic substrate solution was added and reacted for 10 min at room temperature in the dark, and the absorbance was measured at OD650 using a microplate reader (Molecular Devices). The reaction was then stopped by the addition of 2 M sulfuric acid and the absorbance was measured at OD450 using a microplate reader. All measurements were conducted in triplicate.

Cell Imaging and Immunofluorescence

Cells were seeded in 6-well plates or 35-mm glass-bottomed dishes (Mat-Tek) and RhB-NPs or αCT1-NPs filtered through 0.45 mM pores before lyophilization were resuspended in PBS and added to the medium at different concentrations. After overnight incubation, cells were then washed five times with PBS, replenished with fresh medium and observed at various times by phase-contrast and fluorescence microscopy using the EVOS™ FL Auto Imaging System (Thermo Scientific), or fixed at various times with 4% paraformaldehyde for 20 minutes and permeabilized with 0.1% Triton X-100 in a 3% BSA blocking solution for 2 hours at room temperature. Immunostaining was conducted with anti-C-terminus Connexin 43 antibody (Sigma-Aldrich, 1:3000) and detected using secondary antibody conjugated to Alexa Fluor® 488 (Thermo Scientific, 1:500). Biotin-tagged αCT1 was detected with Streptavidin conjugated to Alexa Fluor® 647 (Thermo Scientific, 1:500). Wheat Germ Agglutinin (WGA) conjugated to Alexa Fluor® 488 (Thermo Scientific, 1:500) was used to stain cell membranes. Slides were mounted using ProLong Gold anti-fade reagent with DAPI (Thermo Scientific). Cells were examined under an Opterra inverted fluorescence confocal microscope (Bruker).

Results

Particle Size Optimization

PLGA nanoparticles encapsulating rhodamine B and αCT1 were synthesized. The initial double emulsion particles were made by using 0.05 g PLGA and 2 mL of EA in the primary emulsion and 5 w/v% PVA in the secondary emulsion. However, due to filtering requirements of 0.2 μm for sterilization purposes, the synthesis process required optimization in order to decrease particle size until the majority of the particles were below 0.2 μm. The amount of PLGA, ethyl acetate, and PVA were modified in order to optimize the size of the particles. An ice bath was

also added in order to keep the PLGA below its glass transition temperature (T_g) during high-energy sonication to prevent NP coalescence. Finally, in order to better mimic how αCT1 may change the particle size during size optimization of the particles, 2 mM BSA in water was used as the drug mimic because of its bulkiness. BSA, while larger than αCT1, is hydrophilic and will provide a measure of how size of the molecule encapsulated may affect the size of the particle. BSA was chosen because of the bulkiness and because of its availability.

Table 1 gives a description of the parameters that were modified during the optimization. Because the peak diameter of single emulsion particles was generally below 200 nm, no optimization steps were conducted for the single emulsion particles. Dynamic light scattering (DLS; Malvern Zetasizer Nano ZS) was used to detect average nanoparticle diameter (**Figure 1**). The original parameters used to make particles (Table 1, Sample 1) showed the largest average diameter at 229 nm. Small batch sizes and a lower concentration of PVA in the outer phase during emulsification yielded the smallest average diameter size with the lowest polydispersity index (PDI), meaning these smaller particles were more homogenous in size compared with other samples, and more than half of the collected particles can pass through a sterilization-sized filter (0.2 μm). Parameters from Sample 3 resulted in the smallest particles and PDI, so Sample 3 parameters were applied in the synthesis of double emulsion particles.

Table 1. Particle size optimization of double emulsion particles using bovine serum albumin. BSA=bovine serum albumin, PLGA=poly(lactic-co-glycolic acid), EA=ethyl acetate, PVA=poly(vinyl alcohol), Dia=diameter, stdev=standard deviation, PDI=polydispersity index.

Sample	BSA (μL)	PLGA (g)	EA (mL)	w/v% PVA in outer phase	Ice bath	Diameter (nm) (avg ± stdev)	PDI (avg ± stdev)
1	100	0.05	2	5	No	229±4	0.301±0.014
2	50	0.025	1	5	Yes	149±1	0.190±0.019
3	50	0.025	1	2.5	Yes	143±1	0.158±0.014
4	50	0.025	1	20	Yes	165±1	0.219±0.004

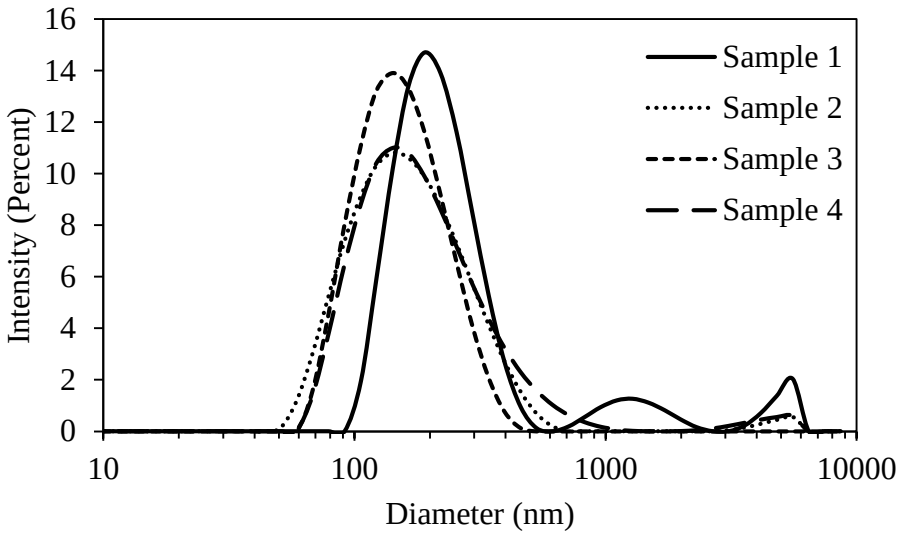

Figure 1. Graph of dynamic light scattering peaks for particle size optimization using BSA as a model drug.

RhB Loading Content and Efficiency Comparison between Single and Double Emulsions

Next, an initial estimation of drug loading and release was made on both single emulsion and double emulsion particles using RhB. While RhB is smaller than αCT1, it is hydrophilic like αCT1, has a low cost, and is more quickly and easily measured by using UV-vis rather than

ELISA assay. So, it is expected that ere will be differences in loading between αCT1 and RhB due to RhB having the ability to diffuse more quickly because of its small size, however RhB will provide a gauge as to how the drug may be released from the particles over time and relative amounts loaded.

Table 2 compares the loading content and encapsulation efficiency of the single and double emulsion particles. The drug content, calculated using **Eq. 1**, was similar for both single and double emulsions. However, drug entrapment, calculated using **Eq. 2**, was higher for double emulsions compared with single emulsions. **Figure 2** also shows the release profiles of the drug from single and double emulsion particles. Over seven days, particles produced using single emulsion synthesis had a higher burst-release of rhodamine, releasing to completion more quickly than the double emulsion particles, which released 94% of rhodamine after seven days.

Table 2. Drug loading and encapsulation efficiency of RhB-PLGA-NPs (all particles filtered to 0.2 μm before measuring loading).

Sample	RhB Loading (ng drug/mg particles)	RhB Loading (%±st.dev)	Encapsulation Efficiency (%±st.dev)
RhB-PLGA-NPs, SE	160±53	0.0160±0.0053	0.00028±0.00015
RhB-PLGA-NPs, DE	167±9	0.0167±0.0009	0.0018±0.0004

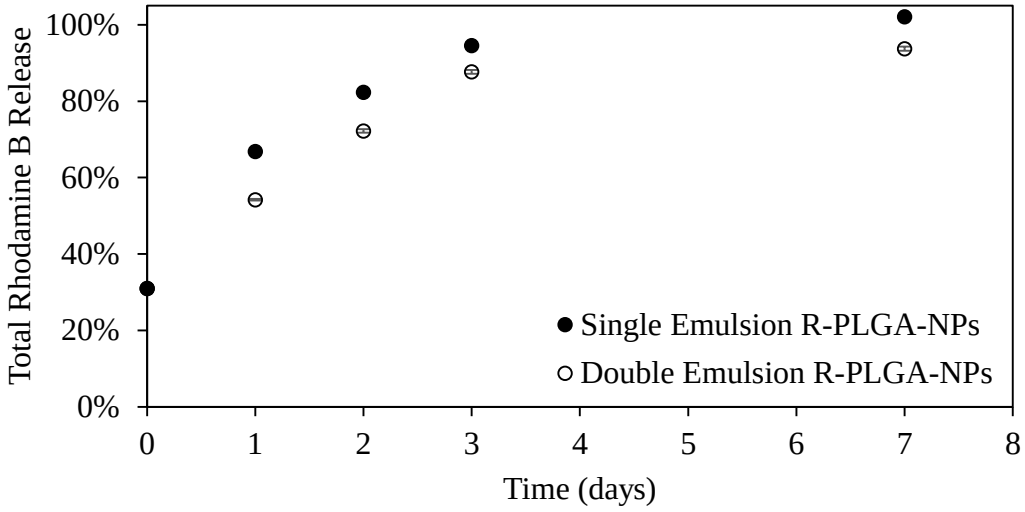

Figure 2. Percent release of rhodamine B from PLGA-NPs over time. Error bars are included (based on 3 or more repetitions), but are smaller than the data markers.

Double emulsion particles had a higher encapsulation efficiency and took longer to release all of the encapsulated material. As the goal is to develop a sustained release αCT1 formulation, these results supported further evaluation of the double emulsion particles.

$$Drug\ Loading\ (^{w}/_{w}\,\%) = \frac{Mass\ of\ Drug\ in\ NPs}{Mass\ of\ Recovered\ NPs} * 100\% \qquad \textbf{Eq. 1}$$

$$Encapsulation\ Efficiency\ (\%) = \frac{Mass\ of\ Drug\ in\ NPs}{Mass\ of\ Drug\ used\ in\ Formulation} * 100\% \qquad \textbf{Eq. 2}$$

Cryoprotectants

Lyophilization is used for long-term storage of the particles in order to keep the particles dry. RhB-NPs and αCT1-NPs were kept frozen to keep the particles below PLGA's T_g and to reduce

possible exposure to moisture, which would prematurely degrade the particles. In order to lyophilize, particles in solution must first be frozen. Before use in clinical trials, the particles are to be resuspended in DI-water or PBS buffer solution and sterilized by filtration at 0.2 μm if particles were not synthesized in a sterile cabinet.

It was noticed that after lyophilization and resuspension, a significant portion of particles were lost during sterile filtration procedures. Even though the zeta potential of the rhodamine-loaded NPs after lyophilization (-28±2 mV) implied a stable suspension, the size of the particles increased during the freezing and/or drying process. It has been hypothesized that freezing allows ice crystals to puncture neighboring particles and essentially fuse them together to make a larger particle. Various methods have been explored to protect PLGA nanoparticles during freezing with positive results, but in general cryoprotectants such as small sugars (sucrose, trehalose, dextrose, sorbitol, etc.) are most commonly used.[21-24] In this study, fast freezing via liquid nitrogen and the addition of cryoprotectants trehalose and sucrose were used to limit particle size growth.

Figure 3 shows a particle diameter of 183 nm before freezing. A slow freeze without cryoprotectant increased particle diameter to above 240 nm and a fast freeze limited growth to reach an average of 215 nm. When large amounts of cryoprotectant are added, such as at 15 w/v% in solution, particle size increased above the size of slow freezing without cryoprotectants, at around 260 nm. Adding large amounts (10% or greater) has in some cases been shown to increase particle size above that of particles frozen without cryoprotectant.[22, 24] In this study, adding cryoprotectants in smaller amounts, especially at 1 w/v%, limited particle size growth.

When trehalose was used at 1 w/v% and frozen quickly, particle size dropped below that of particles frozen with a fast freeze alone. When sucrose is added at 1 w/v%, with either fast or slow freezing, the average particle size remained the closest to the original particle size. The addition of trehalose at 1 w/v% and a slow freeze resulted in a similar particle size to methods using sucrose at the same concentration. Moving forward, 1 w/v% sucrose was added to all particle suspensions before freezing and lyophilizing.

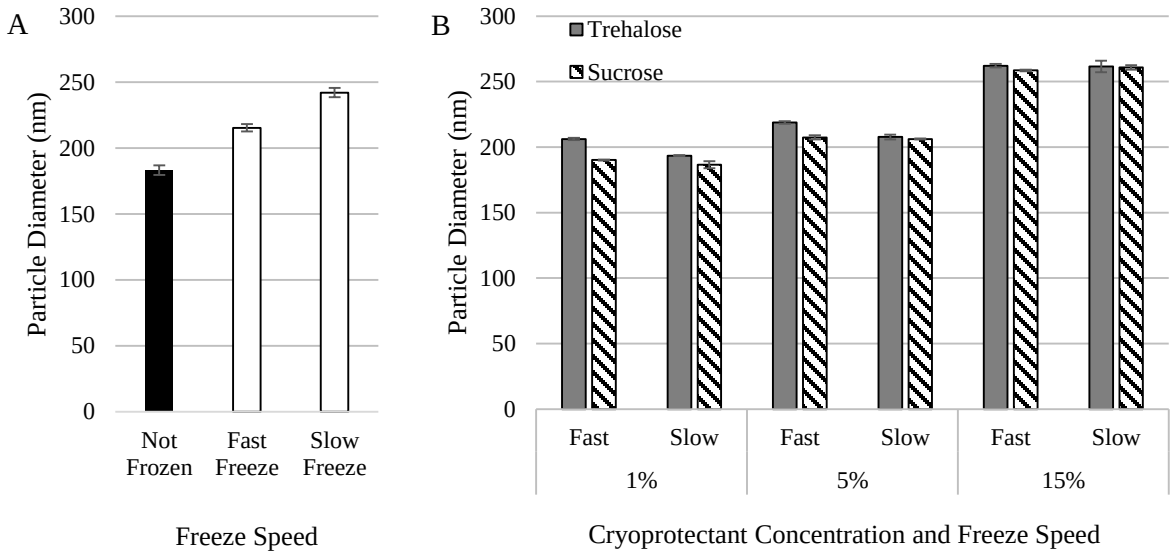

Figure 3. A) Change in particle diameter with and without freezing when cryoprotectants are not in use. B) Particle diameter after freezing in relation to amount of cryoprotectant used. When 1% sucrose (fast or slow freeze) or 1% trehalose (slow freeze) is added, particle sizes achieved are near the size of unfrozen NPs. Trehalose and sucrose added at concentrations of 15% increased particle size to greater than freezing the particles slowly without any cryoprotectant. Error bars are the standard deviation of at least three samples.

Loading and Degradation of αCT1-NPs

After optimizing cryoprotectant parameters to reduce change in NP size during storage, loading and degradation studies were completed on αCT1-NPs. Particles were filtered to 0.2 μm before analysis. Drug loading by mass, measured via ELISA assay and calculated using Equation 1, was 962±88 ng drug/mg particles, % loading was 0.0962±0.0088%, and encapsulation efficiency was 0.000966±0.00049%. Error is the standard deviation of at least three samples. Zeta potential of αCT1-NPs after lyophilization was -23 mV. Entrapment of αCT1 appears to be higher than that for RhB-NPs at almost 1 μg/mg particles, but percent drug loading is less than 0.1% for RhB-NPs and αCT1-NPs.

Figure 4A shows the cumulative release of αCT1 over 21 days, where measurements were made via sandwich ELISA. The release profile showed a burst effect, in which about 50% of peptide was released after three days, followed by a sustained release over the subsequent 18 days until 73% of the total encapsulated drug was released.

Particle morphology and diameter changes were monitored over time using measurements from DLS and SEM image analysis via ImageJ software. Particle size diameters measured using DLS were approximately twice the size of measurements made via SEM. Both DLS and SEM showed increasing particle size from 186 to 208 over the course of 7 days, then increased in size again between 2 and 3 weeks to 223 nm. **Figure 4B** shows the particle size and polydispersity index (PDI) of the particles over time during the degradation study as measured by DLS. PDI also increased with time. Similar particle size trends were found with measurements by SEM. **Figure 4C-H** shows SEM images at Day 1, Day 7, and Day 21 of the degradation. Pores or holes seem to appear after Day 7, and increase in size and quantity with time.

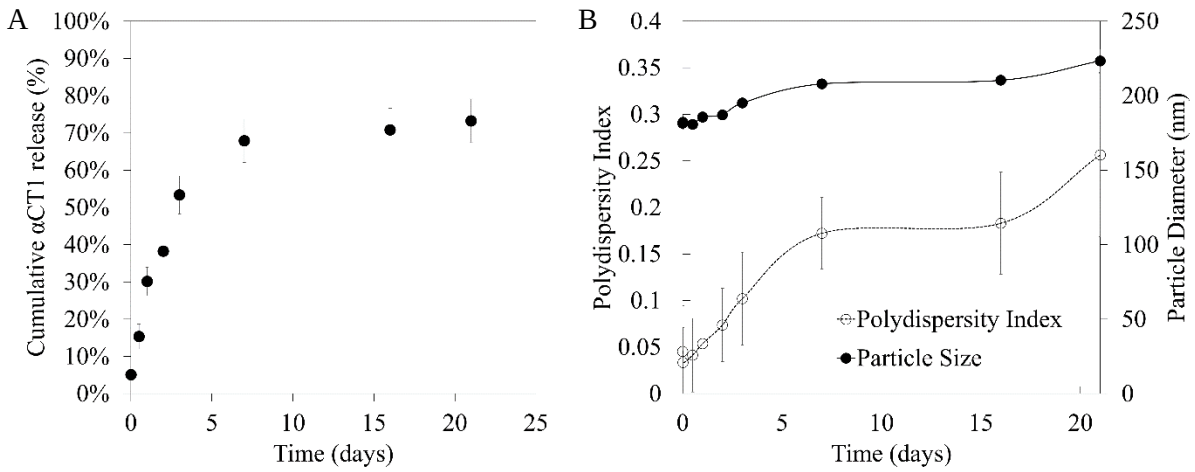
A
Cumulative αCT1 release (%)
100%
90%
80%
70%
60%
50%
40%
30%
20%
10%
0%
0
5
10
15
20
25
Time (days)
B
Polydispersity Index
0.4
0.35
0.3
0.25
0.2
0.15
0.1
0.05
0
Particle Diameter (nm)
250
200
150
100
50
0
Polydispersity Index
Particle Size
0
5
10
15
20
Time (days)

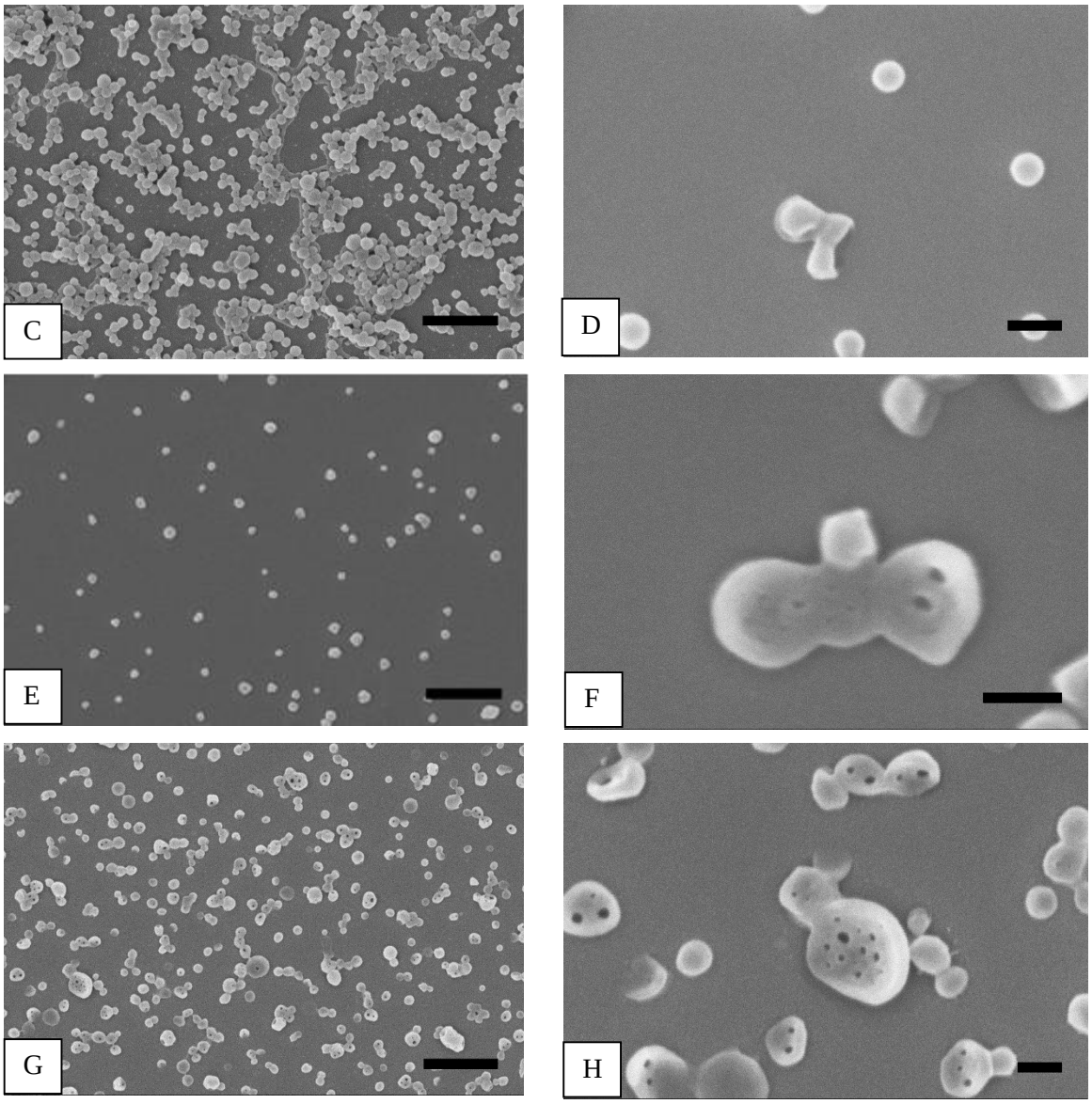

Figure 4. A) Graph of cumulative release of αCT1 from nanoparticles over time as a function of percentage of total drug encapsulated, as measured via sandwich ELISA assay. B) Particle diameter (Z-average) measured by DLS during the degradation of αCT1 nanoparticles and the polydispersity index of the nanoparticles, indicating homogeneity of particle size. SEM images of αCT1-NPs at (C and D) Day 1, (E and F) Day 7, and (G and H) Day 21. Scale bars are 1 μm (C, E, and F) and 100 nm (D, F, and H).

RhB-NP and αCT1-NP Uptake in GSCs and GBM cells

RhB-NPs added to VTC-037 GSCs at various concentrations showed that at least 300 µg/mL of NPs could be added to cells without affecting cell plate adhesion (**Figure 5A**). This concentration was then used for a three-week cell culture to study degrading RhB-NPs and their effect on cells and how long RhB may remain in the cells over time (**Figure 5B**). For the first week of release, a large amount of RhB is present in the cells. At 14 and 21 days, RhB signal is still detected in the cells even after cell passage through trypsinization at day 10.

When 200 µg/ml of RhB-NPs were added to VTC-037 GSCs, cells incubated at 37 °C showed uptake of the RhB-NPs similar to **Figure 5**, but cells incubated at 4 °C had reduced cellular uptake of the RhB-NPs (**Figure 6**).

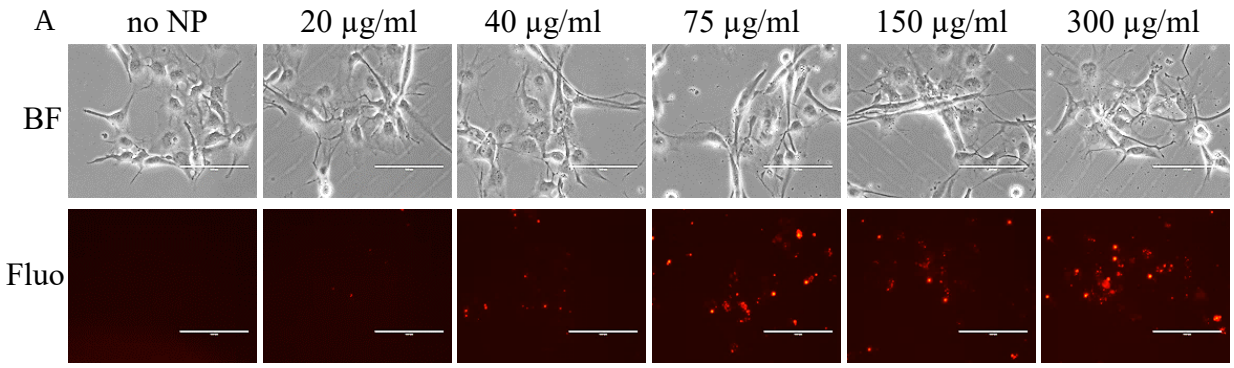

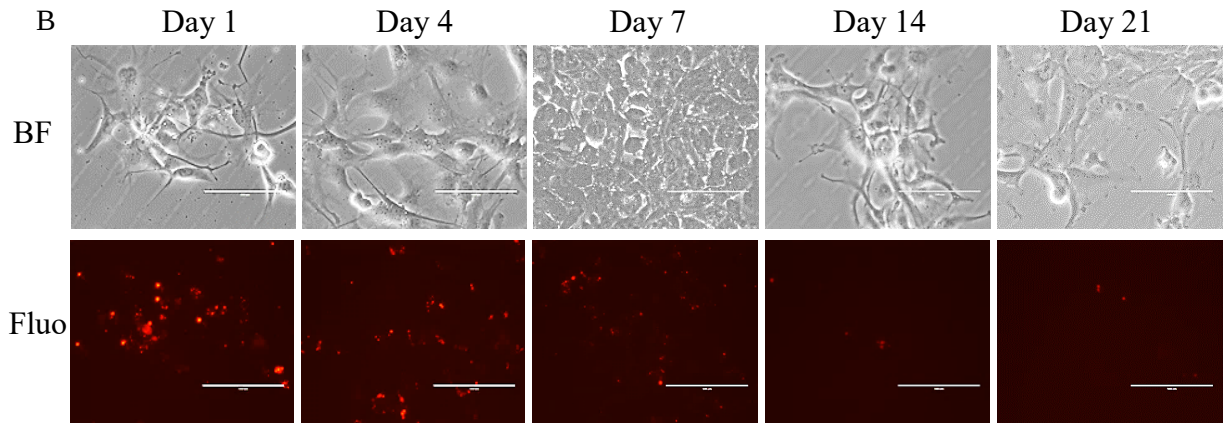

Figure 5. A) Cellular uptake of varying concentration of RhB-NPs to determine optimal concentration for remaining cell studies. Cells incubated overnight before imaging. B) Release of RhB from NPs incorporated into VTC-037 GSCs over three weeks. BF: Bright Field, Fluo: Fluorescence. Scale bar: 200 µm.

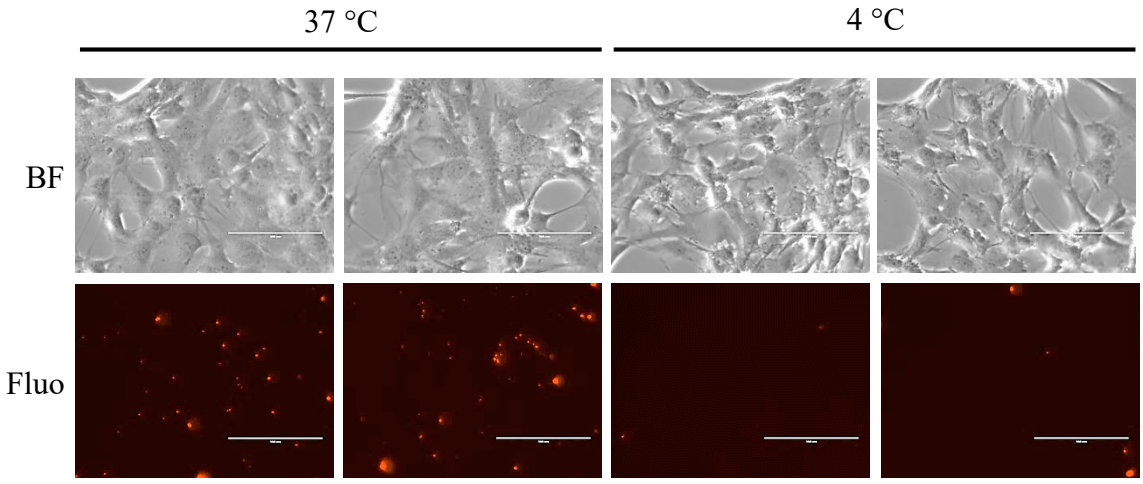

Figure 6. Incorporation of RhB-NPs into GSCs at 37 °C and 4 °C after incubation for 1 hr. BF: Bright Field, Fluo: Fluorescence. Scale bar: 200 µm.

Staining of cell membranes and nuclei with and without RhB-NPs added at 200 µg/ml in the medium of LN229/GSCs shows cellular uptake of NPs is occurring, as RhB-NPs are present in the cytosol but excluded from the nuclei (**Figure 7**). When αCT1-NPs were added at 1 mg/ml in the medium of SF295 cells (RhB-NPs at 1 mg/ml used as a positive control for NP cellular uptake), detection of biotin-tagged αCT1 following αCT1-NP uptake demonstrates the presence of αCT1 in the cells after one and four days (**Figure 8**).

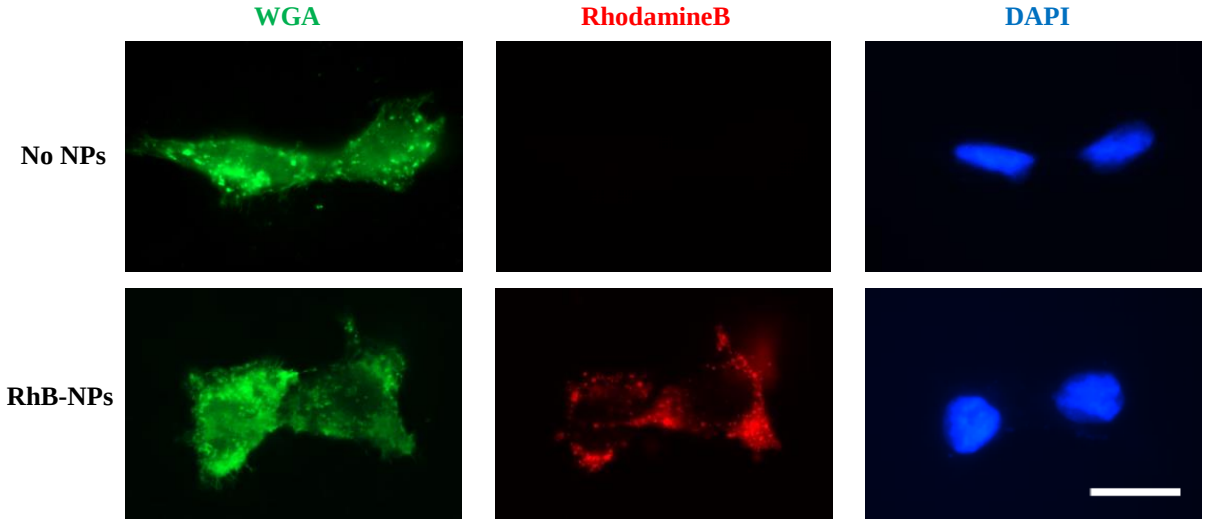

Figure 7. Cellular uptake of RhB-NPs. Scale bar: 20 µm.

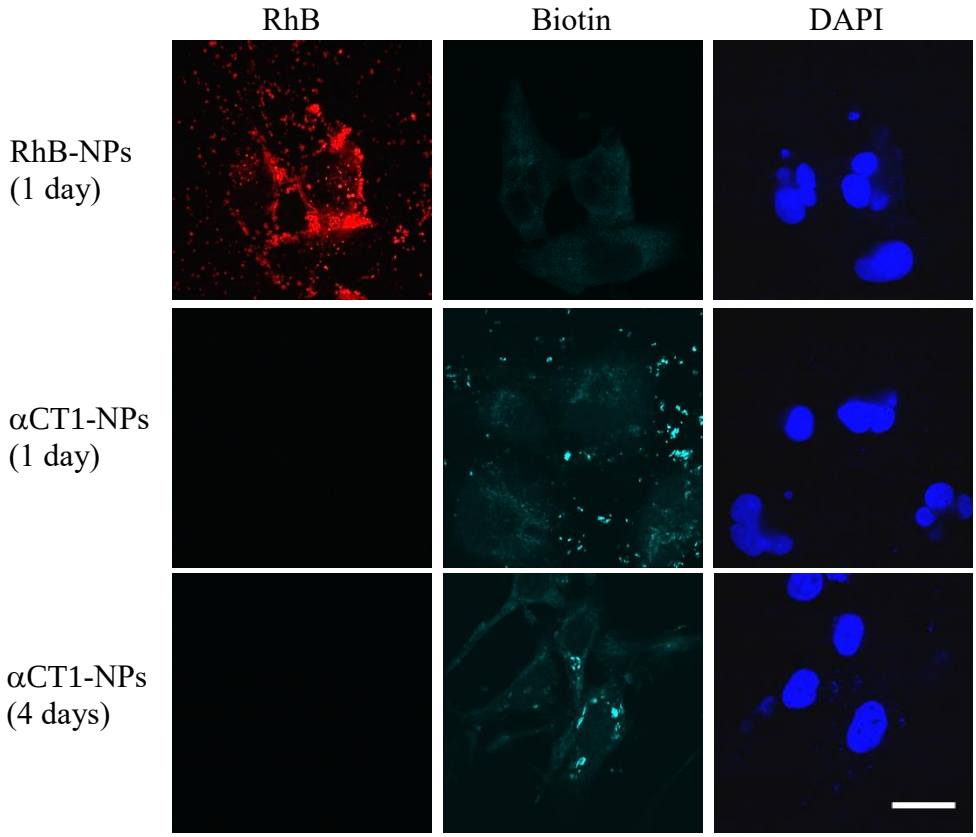

Figure 8. Cellular uptake of RhB- and αCT1-NPs in GBM cells (SF295). Scale bar: 20 μm.

Discussion

This work describes a method to encapsulate the peptide αCT1 using a double emulsion-solvent evaporation method a well as the methods used to minimize particle size for the purpose of sterilization of particles via filtration. Particles release peptide over about 21 days i*n vitro*. It is also demonstrated that VTC-037 GSCs uptake the particles and the presence of peptide in cells is detectable for at least four days. The results indicate that particles may be used for controlled release of αCT1 peptide.

A major factor to consider when creating implantable materials is the sterilization process. Here, sterilization by filtration was determined to be the method least likely to alter the release profile of the encapsulated peptide, so particle size was optimized to achieve the smallest diameter. Particle size optimization reduced the average particle size from 229 nm in diameter to 143 nm in diameter. All other particle sizes had average diameters under 170 nm. This is likely due to dropping the primary emulsion into the PVA solution while vortexing, which became possible when a smaller batch size was used. Smaller batch sizes prevent the solutions from being thrown out of the container during vortexing when the primary emulsion is added to the secondary outer phase.

Particle size of samples 2-4 (see **Table 1**) are similar to that reported by Musumeci et al., where encapsulation of docetaxel resulted in loaded PLGA particles with diameters between 157-172 nm.[25] Sample 3 during size optimization study showed the optimal conditions for minimalizing particle diameter.

The shape of the release profile of RhB from PLGA shown here is similar to the docetaxel release profile reported by Musumeci et al., where following an initial burst release the majority of the drug was released in the first week.[25] However, single and double emulsions should encapsulate amounts of drug differently. Single emulsions generally encapsulate hydrophobic drugs in higher loading percentages, while double emulsions provide a space for hydrophilic drugs to occupy so they are less driven towards the outermost phase.[26] The RhB content in the particles here are similar between the single and double emulsions. Because so little RhB was actually encapsulated, the low loading could be mostly due to adsorption on the surface of the

particles rather than incorporation inside the particles. Encapsulation efficiency is higher for the double emulsion particles because more particles were collected than for single emulsion particles.

As mentioned, the observed encapsulation efficiencies and RhB loading are low for small molecules compared with values in the literature. In comparison, Zhang et al. were able to encapsulate several hundred micrograms of hydrophilic small molecule drugs per milligram of loaded particles.[17] A possible explanation is that RhB-PLGA interactions may limit the amount of RhB that is encapsulated. For example, Budhian et al. discuss the importance of drug-polymer miscibility and its effect on loading, at least for the process of nanoprecipitation.[27] A similar case may be occurring for the RhB-PLGA system, however this was not confirmed.

Chereddy et al. reported loading LL37 peptide of 1.02 μg/mg particles, but achieved a 70% loading efficiency compared with 0.96 μg/mg and <1% encapsulation efficiency for αCT1-NPs shown here. Chereddy reported a particle size of 304.5 nm, which may account for some of the difference with encapsulation efficiency since αCT1-NPs were filtered to 0.2 μm, causing loss in efficiency calculations.[13] Zhang et al. showed a 1.1% drug loading of insulin with encapsulation efficiency near 50% with particle sizes less than 140 nm in diameter. Zhang also did not mention any filtration of particles or associated loss.[18] Thus, while drug loading is too low for practicality here, it is similar to that achieved by others encapsulating peptides.

The peptide release profile from αCT1-NPs appears similar to peptide release from PLGA found by Chereddy et al., where 60% of the drug was released within the first three days, followed by

about 80% of total release at 14 days.[13] Cartiera et al. encapsulated the hydrophobic drug curcumin in PLGA (using single-emulsion method) and also reported burst release profiles, however only 20-30% of was released in the first several hours before releasing up to almost 70% in a more linear fashion for an additional 18 days.[14] The drug's hydrophobicity may have limited the burst release, creating the difference in release profile shape.

Increase in NP size over time was anticipated due to fact that PLGA generally erodes in bulk at neutral to acidic pH at small thicknesses.[28] Bulk erosion occurs when degradation speed occurs more slowly than water uptake, compared with surface erosion in which degradation and removal of polymer occurs more quickly than water uptake. In the case of surface erosion, degradation is limited to the surface of the polymer matrix.[28-29] Here, bulk-eroding PLGA-NPs swell with water during the first few days while the polymer degrades hydrolytically but before erosion occurs.[28, 30] When the particles increase in size again around three weeks, agglomeration of the particles is likely the main cause of size increase. Rescignano et al. also observed agglomeration in nanoparticles as degradation progressed.[31] This is likely due to PVA stabilizer being removed from the surface during nanoparticle erosion. PVA, which is likely incorporated into the PLGA shell even after wash cycles, helps sterically hinder agglomeration. PVA dissolves in water, so as the particle degrades the PVA could also be dislodging and dissolving into the surrounding water. Once the steric hindrance is removed, it would be easier for the particles to agglomerate, thus the size increases. The holes that appear in the NPs are likely due to polymer being removed through erosion channels from the particles during degradation and erosion.[30-31]

When NPs were introduced to cells, staining of cell membranes and nuclei with and without RhB-NPs (**Figure 7**) RhB-NPs were detected in the cytosol but excluded from the nuclei, supporting NP cellular uptake. When cells are incubated at 4 °C, little cellular uptake of the RhB-NPs occurred, which implies energy-dependent endocytosis is the main pathway of NP uptake.[32-33] RhB-NPs as well as αCT1-NPs are internalized by the cells. GBM (SF295) cells uptake the particles and it is observed that αCT1 remains in the cells for at least 4 days (**Figure 8**), which implies that the particles may be able to be used for long-term release.

Conclusions

PLGA nanoparticles successfully encapsulated αCT1 and released 73% of the drug over three weeks *in vitro*. When introduced to human GSCs, RhB was clearly detectable for the first seven days, and then at minimal amounts at 14 and 21 days. RhB was likely detected as a released RhB molecule as well as still encapsulated in a particle. αCT1-NPs introduced to GSC showed αCT1 present in cells over at least four days. However, drug loading and encapsulation efficiency were low, below the therapeutically relevant doses of αCT1, unless an impractical amount of nanoparticles were to be used. Further studies are needed to improve drug loading in order to raise the dosage to more effective levels for patients. Potential methods to improve drug loading are finding sterilization techniques that can be used without filtering particles and further changing particle synthesis methods or using a different particle synthesis method.

Acknowledgements

We would to like thank James Smyth for technical assistance in confocal imaging and the Nanoscale Characterization and Fabrication Laboratory at Virginia Tech for assistance in scanning electron microscopy.

References

1. Xiong, M. H.; Bao, Y.; Yang, X. Z.; Zhu, Y. H.; Wang, J., Delivery of antibiotics with polymeric particles. *Advanced Drug Delivery Reviews* **2014,** *78*, 63-76.
2. Akagi, T.; Baba, M.; Akashi, M., Biodegradable Nanoparticles as Vaccine Adjuvants and Delivery Systems: Regulation of Immune Responses by Nanoparticle-Based Vaccine. **2011,** *247*, 31-64.
3. Anderson, J. M.; Shive, M. S., Biodegradation and biocompatibility of PLA and PLGA microspheres. *Advanced Drug Delivery Reviews* **1997,** *28*, 19.
4. Danhier, F.; Ansorena, E.; Silva, J. M.; Coco, R.; Le Breton, A.; Preat, V., PLGA-based nanoparticles: an overview of biomedical applications. *J Control Release* **2012,** *161* (2), 505-22.
5. Uhrich, K. E.; Cannizzaro, S. M.; Langer, R. S.; Shakesheff, K. M., Polymeric Systems for Controlled Drug Release. *Chemical Reviews* **1999,** *99* (11), 3181-3198.
6. Ghatnekar, G. S.; Grek, C. L.; Armstrong, D. G.; Desai, S. C.; Gourdie, R. G., The effect of a connexin43-based Peptide on the healing of chronic venous leg ulcers: a multicenter, randomized trial. *J Invest Dermatol* **2015,** *135* (1), 289-98.
7. Grek, C. L.; Prasad, G. M.; Viswanathan, V.; Armstrong, D. G.; Gourdie, R. G.; Ghatnekar, G. S., Topical administration of a connexin43-based peptide augments healing of chronic neuropathic diabetic foot ulcers: A multicenter, randomized trial. *Wound Repair and Regeneration* **2015,** *23* (2), 203-12.
8. ClinicalTrials.gov A Study of Granexin Gel to Treat Diabetic Foot Ulcer. https://clinicaltrials.gov/ct2/show/NCT02666131.
9. Murphy, S. F.; Varghese, R. T.; Lamouille, S.; Guo, S.; Pridham, K. J.; Kanabur, P.; Osimani, A. M.; Sharma, S.; Jourdan, J.; Rodgers, C. M.; Simonds, G. R.; Gourdie, R. G.; Sheng, Z., Connexin 43 Inhibition Sensitizes Chemoresistant Glioblastoma Cells to Temozolomide. *Cancer Research* **2016,** *76* (1), 139-49.
10. Moore, K.; Amos, J.; Davis, J.; Gourdie, R.; Potts, J. D., Characterization of polymeric microcapsules containing a low molecular weight peptide for controlled release. *Microscopy and Microanalysis* **2013,** *19* (1), 213-26.
11. Moore, K.; Bryant, Z. J.; Ghatnekar, G.; Singh, U. P.; Gourdie, R. G.; Potts, J. D., A synthetic connexin 43 mimetic peptide augments corneal wound healing. *Exp Eye Res* **2013,** *115*, 178-88.
12. Mathew, A.; Fukuda, T.; Nagaoka, Y.; Hasumura, T.; Morimoto, H.; Yoshida, Y.; Maekawa, T.; Venugopal, K.; Kumar, D. S., Curcumin loaded-PLGA nanoparticles conjugated with Tet-1 peptide for potential use in Alzheimer's disease. *PLoS One* **2012,** *7* (3), e32616.
13. Chereddy, K. K.; Her, C. H.; Comune, M.; Moia, C.; Lopes, A.; Porporato, P. E.; Vanacker, J.; Lam, M. C.; Steinstraesser, L.; Sonveaux, P.; Zhu, H.; Ferreira, L. S.; Vandermeulen, G.; Preat, V., PLGA nanoparticles loaded with host defense peptide LL37 promote wound healing. *J Control Release* **2014,** *194*, 138-47.
14. Cartiera, M. S.; Ferreira, E. C.; Caputo, C.; Egan, M. E.; Caplan, M. J.; Saltzman, W. M., Partial correction of cystic fibrosis defects with PLGA nanoparticles encapsulating curcumin. *Molecular Pharmacology* **2010,** *7* (1), 86-93.
15. Morales-Cruz, M.; Flores-Fernandez, G. M.; Morales-Cruz, M.; Orellano, E. A.; Rodriguez-Martinez, J. A.; Ruiz, M.; Griebenow, K., Two-step nanoprecipitation for the production of protein-loaded PLGA nanospheres. *Results in Pharma Sciences* **2012,** *2*, 79-85.

16. Liu, Q.; Chen, X.; Jia, J.; Zhang, W.; Yang, T.; Wang, L.; Ma, G., pH-Responsive Poly(D,L-lactic-co-glycolic acid) Nanoparticles with Rapid Antigen Release Behavior Promote Immune Response. *ACS Nano* **2015,** *9* (5), 14.
17. Zhang, X.; Chen, G.; Wen, L.; Yang, F.; Shao, A. L.; Li, X.; Long, W.; Mu, L., Novel multiple agents loaded PLGA nanoparticles for brain delivery via inner ear administration: in vitro and in vivo evaluation. *Eur J Pharm Sci* **2013,** *48* (4-5), 595-603.
18. Zhang, X.; Sun, M.; Zheng, A.; Cao, D.; Bi, Y.; Sun, J., Preparation and characterization of insulin-loaded bioadhesive PLGA nanoparticles for oral administration. *Eur J Pharm Sci* **2012,** *45* (5), 632-8.
19. Makadia, H. K.; Siegel, S. J., Poly Lactic-co-Glycolic Acid (PLGA) as Biodegradable Controlled Drug Delivery Carrier. *Polymers* **2011,** *3* (3), 1377-1397.
20. Kanabur, P.; Guo, S.; Rodgers, C. M.; Simonds, G. R.; Kelly, D. F.; Gourdie, R. G.; Verbridge, S. S.; Sheng, Z., Patient-derived glioblastoma stem cells respond differentially to targeted therapies. *Oncotarget* **2016,** *7* (52), 86406-86419.
21. Peppin, S. S. L.; Worster, M. G.; Wettlaufer, J. S., Morphological instability in freezing colloidal suspensions. *Proceedings of the Royal Society A: Mathematical, Physical and Engineering Sciences* **2007,** *463* (2079), 723-733.
22. Fonte, P.; Soares, S.; Costa, A.; Andrade, J. C.; Seabra, V.; Reis, S.; Sarmento, B., Effect of cryoprotectants on the porosity and stability of insulin-loaded PLGA nanoparticles after freeze-drying. *Biomatter* **2012,** *2* (4), 329-39.
23. Tang, K. S.; Hashmi, S. M.; Shapiro, E. M., The effect of cryoprotection on the use of PLGA encapsulated iron oxide nanoparticles for magnetic cell labeling. *Nanotechnology* **2013,** *24* (12), 125101.
24. Bozdag, S.; Dillen, K.; Vandervoort, J.; Ludwig, A., The effect of freeze-drying with different cryoprotectants and gamma-irradiation sterilization on the characteristics of ciprofloxacin HCl-loaded poly(D,L-lactide-glycolide) nanoparticles. *J Pharm Pharmacol* **2005,** *57* (6), 699-707.
25. Musumeci, T.; Ventura, C. A.; Giannone, I.; Ruozi, B.; Montenegro, L.; Pignatello, R.; Puglisi, G., PLA/PLGA nanoparticles for sustained release of docetaxel. *Int J Pharm* **2006,** *325* (1-2), 172-9.
26. Jain, R. A., The manufacturing techniques of various drug loaded biodegradable poly(lactide-co-glycolide) (PLGA) devices. *Biomaterials* **2000**, 16.
27. Budhian, A.; Siegel, S. J.; Winey, K. I., Haloperidol-loaded PLGA nanoparticles: systematic study of particle size and drug content. *International Journal of Pharmaceutics* **2007,** *336* (2), 367-75.
28. Burkersroda, F. v.; Schedl, L.; Gopferich, A., Why degradable polymers undergo surface erosion or bulk erosion. *Biomaterials* **2002,** *23*, 11.
29. Tamada, J. A.; Langer, R., Erosion kinetics of hydrolytically degradable polymers. *Proc Natl Acad Sci U S A* **1993,** *90*, 5.
30. Gopferich, A., Polymer Bulk Erosion. *Macromolecules* **1997,** *30*, 7.
31. Rescignano, N.; Amelia, M.; Credi, A.; Kenny, J. M.; Armentano, I., Morphological and thermal behavior of porous biopolymeric nanoparticles. *European Polymer Journal* **2012,** *48* (7), 1152-1159.

32. Firdessa, R.; Oelschlaeger, T. A.; Moll, H., Identification of multiple cellular uptake pathways of polystyrene nanoparticles and factors affecting the uptake: relevance for drug delivery systems. *Eur J Cell Biol* **2014,** *93* (8-9), 323-37.
33. Kou, L.; Sun, J.; Zhai, Y.; He, Z., The endocytosis and intracellular fate of nanomedicines: Implication for rational design. *Asian Journal of Pharmaceutical Sciences* **2013,** *8* (1), 1-10.

Chapter 6

Flash Nanoprecipitation Method for Increased Loading of a Connexin43 Mimetic Peptide-loaded PLGA Nanoparticle to Target Glioblastoma Cells

In the previous chapter, low loading of aCT encapsulated in particles was found to be a major challenge. This chapter addresses the low loading by using a flash nanoprecipitation method for encapsulation. Initial data showed an increase in loading. Further increases in loading was explored by using RhB as a model drug and varying several parameters in particle synthesis. Loading increases were confirmed with reintroduction of αCT1. This work found at least a one order of magnitude increase in drug loading compared with that of the previous chapter.

In this chapter, data and analysis of RhB-PLGA-NPs was collected by myself, Ms. Payton Roberts, and Mr. Garrison Ferrell. Data and analysis of αCT1-PLGA-NPs were collected by myself. Dr. Richey M. Davis provided the flash nanoprecipitation mixers so this study could be conducted. Representatives of FirstString Research, Dr. Christina L. Grek and Dr. Gautam S. Ghatnekar, graciously provided αCT1. Zhi Sheng and Robert G. Gourdie provided insight into particle requirements for use in glioblastoma. Dr. Samy Lamouille assisted with ELISA assays. The chapter was drafted by myself, later edited by my academic advisor, Dr. E. Johan Foster. This chapter has not yet been submitted for publication, and is formatted similarly to the Introduction.

Flash Nanoprecipitation Method for Increased Loading of a Connexin43 Mimetic Peptide-loaded PLGA Nanoparticle to Target Glioblastoma Cells
Rose Roberts, Payton Roberts, Garrison Ferrell, Christina L. Grek, Richey M. Davis, Gautam S. Ghatnekar, Zhi Sheng, Robert G. Gourdie, Samy Lamouille, E. Johan Foster.
Nanotechnology, manuscript in progress.

6.1. Introduction

Glioblastoma is a deadly form of brain cancer that has a five-year survival rate of less than 5%.[1] Current treatment methods include using temozolomide (TMZ) or other chemotherapeutic drugs in conjunction with resection of the tumor. However, because of microscopic tendrils that infiltrate the brain, full tumor removal is impossible. Remaining tumor cells quickly become resistant to chemotherapeutics and radiation.[2] A new peptide drug, αCT1, has been shown to reduce glioblastoma cell resistance to chemotherapy.[1] However, αCT1 is metabolized by the body within about 24 hours,[3] which is not conducive to long-term treatment.

Encapsulation of small molecule, peptide, and protein drugs in biodegradable polymers has been extensively studied to control the release of drugs over time. Various methods can be used for encapsulation, including emulsion-solvent evaporation and nanoprecipitation. Nanoprecipitation, for example, drops a water-miscible organic solvent containing polymer and drug ("solvent stream") into a vat of water ("anti-solvent") such that the polymer in the solvent stream precipitates out of solution as the solvent mixes with the anti-solvent, capturing the drug in the process.[4-5] Precipitation is generally used for hydrophobic drugs, but some hydrophilic drugs have been successfully encapsulated.[4, 6-8]

Flash nanoprecipitation (FN) is a variant of precipitation in which a mixer is used to obtain turbulent mixing speeds for achieving small particle sizes.[6] Turbulent mixing induces supersaturation, limiting nucleation and growth of particles.[6] The Marangoni effect, describing surface tension and flow of the solvent/anti-solvent interfaces, can also have an effect on diffusion of solvent from the growing particles.[5, 7, 9] The advantage of using this process is that the polymer and drug are not exposed to high temperatures, extended shearing, or high-energy sonication.[7] It is also advantageous for molecules such as proteins that may denature in contact with a water/oily interface, which is present in emulsion-solvent evaporation systems.[7, 9] FN has also been shown to increase drug loading in particles, depending on the system.[10]

Others have shown how various factors may affect drug encapsulation. For example, the anti-solvent phase can be altered to make hydrophilic drug solubility less favorable, driving the drug to remain in the solvent phase where the polymer can more easily capture it.[8, 10] Bilati et al. showed that by changing the solvent, particle size of unloaded nanoparticles is affected, and particle size can affect loading capacity of the particles.[4, 6, 9] Concentrations of drug and polymer

in solution overall and relative to each other also effect loading.[11] Drug-polymer interactions, including solubility of drug in the polymer, also effects the loading in the particles.[10-11] A review by Miladi consolidates many of the studies surrounding the understanding of nanoprecipitation.[12] However, there are mixed results from various investigators and flash nanoprecipitation to encapsulate a peptide is still not well understood.

It has been previously shown that αCT1, a short peptide drug, can be encapsulated via double emulsion-solvent evaporation.[13] Here, PLGA nanoparticles were produced using flash nanoprecipitation in order to increase the drug loading. After initial proof of concept, modifications were made to the process to further increase loading. The model drug rhodamine b was used as a substitute for hydrophilic peptide drug αCT1 during system exploration. The system was optimized for maximum drug loading using rhodamine b by modifying solvent, anti-solvent, and post-production processes. Finally, the parameters that gave the highest loading were confirmed using αCT1.

6.2. Materials

Poly(D,L-lactide-co-glycolide) (PLGA) of three different types were purchased from Sigma Aldrich: Resomer 502H (MW 7000-17000, 50:50 lactic acid:glycolic acid, acid terminated), Resomer 502 (MW 7000-17000, 50:50 lactic acid:glycolic acid, ester terminated), and Resomer 504H (MW 38000-54000, 50:50 lactic acid:glycolic acid, acid terminated). Poly(vinyl alcohol) (PVA; 13000-23000 MW, 87-89% hydrolyzed), rhodamine B (RhB; HPLC grade, ≥95%), phosphate-buffered saline (PBS, reconstituted in DI-water; BioPerformance Certified, pH 7.4, 0.01 M) and 2-pyrrolidone (2P, synthesis grade) were also purchased from Sigma Aldrich. Dimethyl sulfoxide (DMSO; sequencing grade, >99.5% pure) was purchased from Thermo Scientific. N-methylpyrrolidone (NMP) was purchased from Fisher Scientific.

6.3. Methods

6.3.1. Synthesis of PLGA-NPs

PLGA nanoparticles were synthesized using the flash nanoprecipitation method. Solvent solution and anti-solvent solutions are prepared separately, then mixed together in a two-jet mixer to create particles. For solvent solutions, RhB-loaded particle solvent solution was prepared by dissolving PLGA and RhB in DMSO or other solvent for at least 30 minutes. For αCT1-loaded

nanoparticles, water must be used as a co-solvent at a concentration of 10 vol% water in DMSO. In previous studies using RhB, it was found that putting the drug in the antisolvent did not change or decreased the loading of drug in the particles, so the drug remained in the solvent solution. In order to prepare the solvent solution, 2.2 w/v% PLGA was first dissolved in DMSO (60 mg PLGA in 2.7 mL DMSO) for 30 minutes, then 0.2 w/v% αCT1 in water (6 mg αCT1 in 0.3 mL water) was added to the PLGA solution and sonicated for at least 15 minutes until solution was clear. To prepare PVA-based anti-solvent solution, PVA was dissolved in DI-water for one hour at 90 °C or until granules were no longer visible. Low pH anti-solvent was prepared by using hydrochloric acid to drop pH of DI-water until reaching a pH of 3. PBS anti-solvent was used as-prepared, at a pH of 7.4 and 0.01 M concentration.

To synthesize particles, one 5 mL glass syringe each was used for the solvent and anti-solvent. About 0.5 mL more of the anti-solvent solution was loaded in the syringe compared to the solvent syringe. Syringes were attached to the mixer, then about 0.5 mL of anti-solvent, or until the volumes of each syringe were the same, was pre-loaded into the mixer to facilitate more homogenous mixing. Then, a Petri dish or other stiff material was used to push both syringes at the same time at a rate of at least 0.5 mL/min through the syringe. Particles were captured in at least 50 mL of DI-water in order to decrease the likelihood of Ostwald ripening before transfer to dialysis tubing. Particles were dialyzed using 12000 MWCO tubing from Fisher for 24 hours unless otherwise stated, with 4-5 water exchanges throughout. Finally, particles were washed twice via centrifugation method to remove excess surfactant before characterization. Centrifuge tubes used were 50 mL conical bottom tubes or Spin-X concentrator tubes (20 mL, molecular weight cut off (MWCO) 10 kDa or 100 kDa, Corning). Particles were frozen at -20 °C for storage.

6.3.2. Particle Sterilization

To make particles sterile, all solutions were sterilized via filtration to 0.2 um and all equipment was sterilized with 70% ethanol before particle synthesis. Sterile dialysis cartridges (Slide-A-Lyzer dialysis cassettes, gamma irradiated, 10000MWCO, 30 mL volume, ThermoFisher Scientific) were used and centrifuge washing was conducted under sterile conditions.

6.3.3. Materials Characterization Methods

Particle size was measured using a Malvern Zetasizer Nano-ZS. Scanning electron microscopy (SEM) was performed at the Nanoscale Characterization and Fabrication Laboratory

in Blacksburg, VA using the LEO (Zeiss) field-emission SEM. UV-vis absorbance for rhodamine release studies was measured using a Cary 60 UV-Vis spectrophotometer by Agilent Technologies.

6.3.4. Enzyme Linked Immunoassay (ELISA)

To enable peptide tracking in *in vitro* and *in vivo* assays, an amino-terminal biotin tag was added to the αCT1 sequence. The *in vitro* release of biotin-tagged αCT1 was measured by sandwich enzyme linked immunoassay (ELISA) using the OptEIA kit (BD Biosciences). Each well of a Nunc MaxiSorp™ 96-well microplate (Thermo Scientific) was coated with coating buffer containing 1 µg/mL of anti-C-terminus connexin43 antibody (Sigma-Aldrich) and incubated overnight at 4 °C. The wells were then washed before blocking with 1% bovine serum albumin for 2 h at room temperature. Serial dilution of biotin-tagged αCT1 as standards and samples containing biotin-tagged αCT1 collected at different times from the *in vitro* release study were added in the corresponding wells and incubated overnight at 4 °C. The wells were then washed before adding 1 µg/ml Neutravidin-conjugated HRP (Thermo Scientific) for 1 h at room temperature. After washing, 3,3',5,5'-Tetramethylbenzidine (TMB) chromogenic substrate solution was added and reacted for 10 min at room temperature in the dark, and the absorbance was measured at OD650 using a microplate reader (Molecular Devices). The reaction was then stopped by the addition of 2 M sulfuric acid and the absorbance was measured at OD450 using a microplate reader. All measurements were conducted in triplicate.

6.3.5. Drug Loading and Particle Yield

Drug loading and encapsulation efficiency were calculated using Equation 1 and Equation 2, respectively, based on the measured concentrations of drug in solution. Calculations were performed similarly for both RhB and αCT1 loaded particles. Particle yield was conducted via gravimetric analysis of particle suspensions.

$$Drug\ Loading\ ({}^{W}/_{W}\,\%) = \frac{Mass\ of\ Drug\ in\ NPs}{Mass\ of\ Recovered\ NPs} * 100\% \qquad \textbf{Eq. 1}$$

$$Encapsulation\ Efficiency\ (\%) = \frac{Mass\ of\ Drug\ in\ NPs}{Mass\ of\ Drug\ used\ in\ Formulation} * 100\% \qquad \textbf{Eq. 2}$$

6.3.6. In Vitro Release of Drug from Nanoparticles

Nanoparticles were suspended in 0.01 M PBS solution at 1 mg/mL and incubated at 37 °C for the duration of the release study. At each time point, the particles were centrifuged into a pellet

and the supernatant was collected for drug content analysis. The removed supernatant was replaced with the same volume of fresh PBS solution in order to maintain a consistent concentration and the particles were redispersed via bath sonication for 10-15 minutes. Samples of dispersions were taken and analyzed for dynamic light scattering (DLS). SEM samples were prepared by adding a drop of the particle suspension onto silicon wafer pieces taped to an SEM stub for analysis.

6.4. Results and Discussion

In order to assist the treatment of glioblastoma, PLGA nanoparticles were loaded with αCT1 in order to control release of the drug over several weeks. Initial loading of the particles was higher than previous work (reference to DE paper), however further understanding of the mechanism of flash nanoprecipitation for this system was explored in order to further increase the loading. Exploration of the 2-jet mixer setup was conducted using RhB, and the modifications that maximized model drug loading were confirmed using αCT1.

6.4.1. Initial Loading and Release of αCT1-NPs

Initial parameters used for particle synthesis were based on solubility of αCT1 and PLGA in DMSO. Particles achieved a loading of 0.05 w/w% and yield of 29% with an encapsulation efficiency of 0.17%. Drug was released over three weeks and showed a linear release profile, as shown in Figure 6.1**Error! Reference source not found.**.

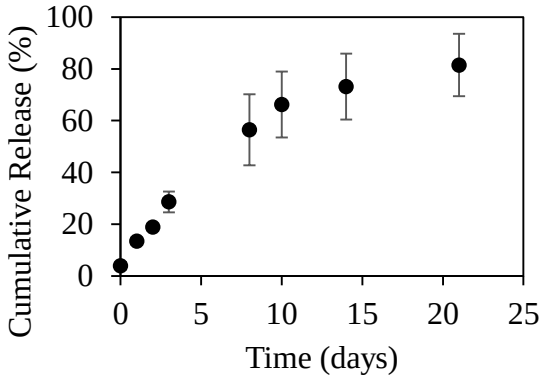

Figure 6.1. Release of αCT1 from PLGA-NPs before increasing loading.

6.4.2. Maximizing Drug Loading

In order to increase drug loading and further understand how parameters affect the 2-jet mixer system, modifications to the solvent, anti-solvent, and capture fluid factors were conducted. The model drug used was RhB due to its hydrophilicity, cost and quick measurement capability

using UV-vis. A description of factors that were modified can be seen in Figure 6.2 and changes in drug loading and encapsulation efficiency can be found in Table 6.1. At least three samples were made for each modification, and standard deviations are reported. Values without standard deviations required all three samples to be combined together in order to have a measurable amount of sample, and so no error can be reported. Because large increases in drug loading are desirable, trends were taken as being 20% larger or smaller than the upper and lower bounds set by the standard deviation.

6.4.2.1. Solvent Solution Variations

Modifications to the solvent solution either did not change or decreased drug loading and encapsulation efficiency for all but sample 7, in which the encapsulation efficiency was higher compared with the control. Using 2-pyrrolidone as a solvent decreased the drug loading. Modifications made to increase drug loading were 1) increase drug added to the system; 2 and 3) changing the solvent based on its solubility parameters, being either higher or lower than the solubility parameter of DMSO; 4 and 5) modifying PLGA by changing the end groups or increasing molecular weight, and 6-9) increasing the concentration of PLGA, and thus the ratio of drug to polymer. Some compounding effects were also explored, by changing the concentration of PVA in the antisolvent for samples 8 and 9.

Previous studies have found that there is a peak loading that can be achieved during drug encapsulation, after which particles maintain the same amount of loading but begin to lose encapsulation efficiency since remaining non-encapsulated material is removed during purification steps.[11-12] To determine if any more rhodamine would be encapsulated, a ten times concentrated solution of RhB in solvent was used to dissolve the PLGA (Sample 1). However, no significant drug loading change occurred.

Effect of Hansen solubility parameter on drug loading was explored (Samples 2 and 3). The solubility parameter describes how quickly two solvents mix with each other. Generally, the further apart the solubility parameters, the less easily two solvents will mix. Water has a Hildebrand solubility parameter of 47.8, DMSO's parameter is at 26.7. Because previous studies have shown a DMSO-water system works for encapsulation, solvents that were miscible with water and had solubility parameters closer to and farther away from DMSO were chosen. NMP has a solubility parameter of 23.1 and 2-pyrrolidone has a solubility parameter of 30.1. Bilati et al.

found a difference in particle size when choosing solvent based on the solubility parameter, in that smaller particle sizes were formed with the solvent and antisolvent solubility parameters were closer together.[9] This is likely due to the ability of the solvent to be drawn more quickly into the antisolvent, to which we theorized a higher drug loading could be achieved since there was less chance of the drug from "escaping" the particles during formation until the solvent could be removed. However, DMSO showed the best drug loading compared with NMP and 2-pyrrolidone.

Two polymer modifications were explored to test whether changes in PLGA increased the drug loading (Samples 4 and 5). Higher molecular weight PLGA has shown mixed results regarding drug loading changes. A molecular weight of 38,000-54,000 did not produce any changes in loading for our system. Changing the end groups of the polymer to ester end-capped would create a more neutral-charged particle. This was found to slightly decrease drug loading compared with control parameters.

Concentration of polymer in the solvent solution was explored by increasing to 2, 3 or 5 times the concentration used in the baseline sample (Samples 6-9). Previous studies have shown that higher drug loading can be achieved when polymer concentration is increased.[14-15] However, no changes were found in drug loading with increased PLGA concentration and agglomeration was observed. At 5 times the concentration, the polymer precipitated and agglomerated such that the mixer clogged. At 3 times the concentration, particles agglomerated soon after dialysis started.

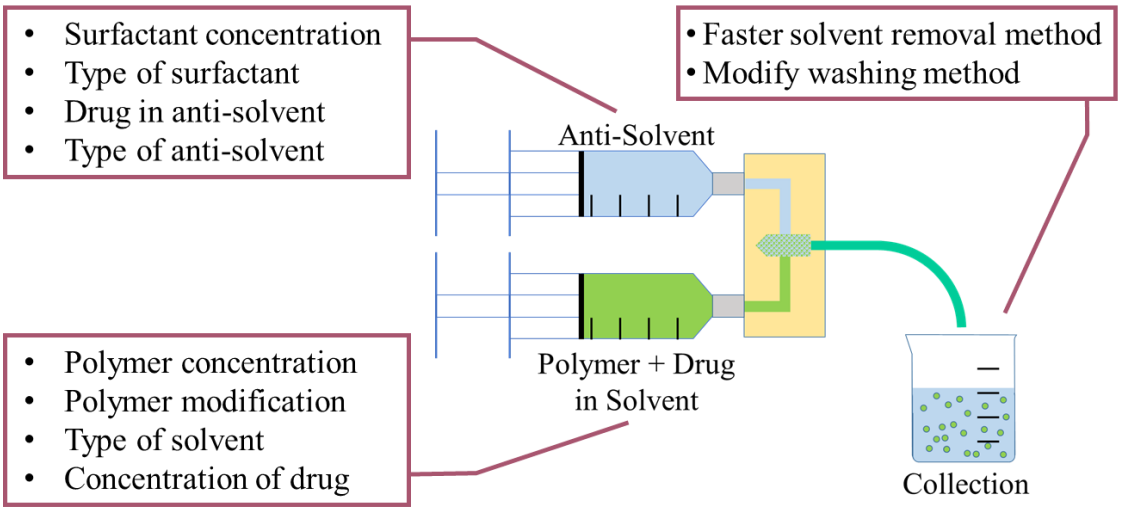

Figure 6.2. Schematic of flash nanoprecipitation 2-jet mixer set up with factors modified for loading maximization study.

6.4.2.2. Anti-solvent Solution Variations

Modifications made to the antisolvent had more success in increasing the drug loading, with two samples showing an increase. No samples showed a decrease in drug loading or encapsulation efficiency. Choice in modifications to increase drug loading included Samples 10-13) increasing or decreasing the concentration of surfactant compared with the control; 14) effect of long-term storage of a PVA solution; 15) effect of filtering the solvent and antisolvent solutions before particle synthesis, as occurs during sterilization procedure; 16 and 17) effect of changing surfactants; 18 and 19) effect of creating a less favorable environment for drug to leach into during dialysis, via pH change and osmotic pressure via salt addition (PBS); and 20) effect of moving the drug in to the antisolvent.

Effect of surfactant concentration and type were explored.[11-12] By increasing PVA concentration, loading improved but encapsulation efficiency decreased (Sample 13). PVA concentrations of 0.3-0.5% had better loading and no change in the encapsulation efficiency, and 0.05% PVA had increased loading and encapsulation efficiency, however the particles showed instability in suspension and agglomerated soon after washing steps were complete (Samples 10-12). Tween 80 was explored as an alternative surfactant in comparison with PVA (Samples 16 and 17). The new surfactant showed an increase in encapsulation efficiency, but also showed agglomeration in both concentrations used.

The anti-solvent was modified to decrease the affinity for RhB to enter into the antisolvent in order to keep the drug in the solvent phase as long as possible (Samples 18 and 19). This would increase the likelihood of the drug to be encapsulated by using an anti-solvent that is a non-solvent for the drug as well as the polymer.[10] Two modifications were used, including using a neutral salt (PBS buffer) without PVA and using water adjusted to pH 3 using HCl. Using salts in the anti-solvent is based on the concept of salting out proteins for purification purposes. A change in pH has been used by Bala et al. when using a double emulsion process to increase loading and by Govender et al during nanoprecipitation.[8, 16] By decreasing pH, the solubility of the drug in the aqueous phase decreased, thus increasing loading. When using PBS, the drug loading was approximately the same as the control, however encapsulation efficiency dropped due to a drop in overall yield of particles. Particles made with an antisolvent with pH 3 had better loading than the control, but worse encapsulation efficiency, again because of an overall lower yield of particles.

Another modification to the anti-solvent was to add the drug to the anti-solvent rather than being in the solvent phase. Several studies have shown this to be a reliable method to encapsulating drug.[17] Our studies show no changes in drug loading from putting RhB in the antisolvent compared with in the solvent phase (Sample 20).

6.4.2.3. Collection and Post-Synthesis Modifications

Final modifications to the samples occurred in the collection process, centering around centrifugation and dialysis steps. These samples showed the largest overall increase in concentration and encapsulation efficiency. Modifications included Samples 21 and 22) centrifuging at a lower temperature in order to help preserve particle integrity (i.e., remain further outside of the T_g of PLGA); and 23) decreasing dialysis time to 6 hours and using Spin-X concentrator tubes, which would allow the particles to concentrate rather than pelleting, in case DMSO is not fully removed.

Some increase in drug loading was seen from using a refrigerated centrifuge (Sample 21). For Sample 23, by dialyzing for a shorter period of time, there is less opportunity for the drug to diffuse through the particle and into the surrounding fluid during solvent removal. Chorny et al. used a volatile solvent for nanoprecipitation, and they explored how increasing solvent evaporation rate could increase loading.[15] While they did not see any change of loading, the concept of decreasing solvent removal time for a non-volatile solvent was a concept we wanted to explore. The purpose of using a concentrator is that it avoids creating a pellet of particles that may be difficult to redisperse after centrifugation if solvent remains in the particles, causing the particles to remain soft and have greater potential of agglomeration. Using the concentrator after 6 hours of dialysis significantly improved loading and encapsulation efficiency of the particles.

Overall, the modifications to the baseline method that increased drug loading most included decreasing PVA content, centrifuging at reduced temperature, using concentrator

centrifuge tubes, and reducing dialysis time.

Table 6.1. Modifications, drug loading, and encapsulation efficiency of samples used for loading maximization experiments.

Sample	Solvent	Anti-Solvent	Collection	Drug Loading %	Encapsulation Efficiency %
Baseline	DMSO 2 w/v % PLGA 0.2 w/v% RhB	1 w/v% PVA in water	Dialyze 24 hrs Wash twice at 25 °C	0.17±0.09	0.61±0.86
Modifications to Solvent					
1	2 w/v% RhB	--	--	0.38±0.19	0.16±0.05
2	2-Pyr as solvent	--	--	0.023	0.0037
3	NMP as solvent	--	--	0.13±0.08	0.34±0.1
4	Ester End-capped PLGA	--	--	0.1±0.03	0.16±0.07
5	PLGA MW 38-54 kDa	--	--	0.20±0.08	0.44±0.4
6	4 w/v% PLGA	--	--	0.18±0.03	1.4±0.5
7	6 w/v% PLGA	--	--	0.130±0.007	2.203±0.218
8	6 w/v% PLGA	0.4 w/v% PVA	--	0.102±0.010	1.678±0.404
9	10 w/v% PLGA	0.4 w/v% PVA	--	0.076	1.729
Modifications to Anti-Solvent					
10	--	0.05 w/v% PVA	--	0.185	0.636
11	--	0.3 w/v% PVA	--	0.36±0.02	2.1±0.5
12	--	0.5 w/v% PVA	--	0.205	0.131
13	--	3 w/v% PVA	--	0.48±0.07	0.21±0.02
14	--	Old PVA	--	0.174	0.201
15	PLGA filtered to 0.2 um	PVA filtered to 0.2 um	--	0.112	0.162
16	--	1 w/v% Tween 80	--	0.114±0.017	1.970±0.225
17	--	0.1 w/v% Tween 80	--	0.084±0.002	1.170±0.044
18	--	pH 3, no PVA	--	0.35±0.06	0.49±0.2
19	--	PBS, no PVA	--	0.15±0.04	0.04±0.005
20	No RhB in solvent	0.2w/v % RhB	--	0.161	0.116
Modifications to Collection					
21	--	0.4 w/v% PVA	Centrifuged at 4 °C	0.311	0.216
22	--	--	Centrifuged at 4 °C	0.113	0.099
23	--	--	Dialyzed for 6 hours, Concentrator tubes	0.366±0.045	6.452±1.257

*-- same parameters used as control

**Values without standard deviations required batch combinations in order to have measureable amount of particle yield and loading

RED value upper bound is 20% lower than control value lower bound, GREEN value lower bound is 20% greater than control value upper bound, based on standard deviations

6.4.3. Particle Size and Morphology of Loading Maximization Study

Particle size of the samples is also important for glioblastoma applications, since the particles should fit between the extracellular space. DLS was used to measure particle size. Each sample was briefly vortex-mixed approximately two minutes before measurements were taken. This allows most large agglomerates to settle before measuring remaining particles, although a few remaining agglomerates appear on graphs above 1000 nm. Most samples otherwise showed a single peak between 150-200 nm in particle diameter. Figure 6.3 shows representative plots of the particle size of several higher-loading samples. Sample 23, in which 6 hours of dialysis and concentrator tubes were used, showed an intensity peak around 150 nm but also showed what could be a convoluted peak near 60 nm. The volume % peak shows Sample 23 around 65 nm, which suggests that most of the particle diameters in Sample 23 are around 60 nm, however larger particles may be biasing the intensity measurement.[18] Since preparation of Sample 23 did not involve changes in any processes during synthesis, only during particle collection, it suggests that there is a higher number of smaller particles in the other samples that may not be fully captured in the wash cycles or are not redispersing well after pelletization.

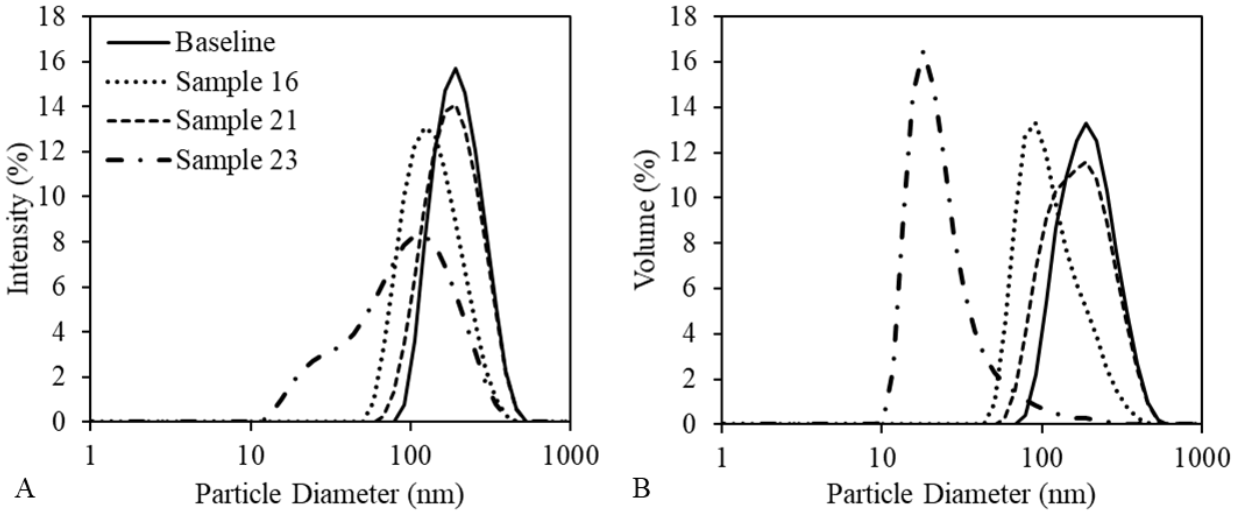

Figure 6.3. Particle size distributions based on A) intensity and B) volume of representative particle sizes for Baseline and Samples 16 (1 w/v% Tween 80), 21 (0.4% PVA, refrigerated centrifuge washes) and 23 (6 hrs dialysis and concentrator centrifuge tubes), measured using DLS.

Particle morphology was observed using SEM, and a sampling of images can be viewed inFigure 6.4. Generally, particles were spherical and smooth. Particles from Sample 23 conditions,

which used the concentrator centrifuge tubes, were more difficult to visualize (Figure 6.4(D, H)). It appeared that a blanket may have been coating the particles, making smaller particles especially difficult to image. It is likely that PVA remained in NP suspension since the MWCO of the concentrator tubes was 10 kDa and PVA molecular weight was 13-23 kDa. Particles that could be seen for Sample 23 were spherical and smooth, and no signs of agglomeration were present.

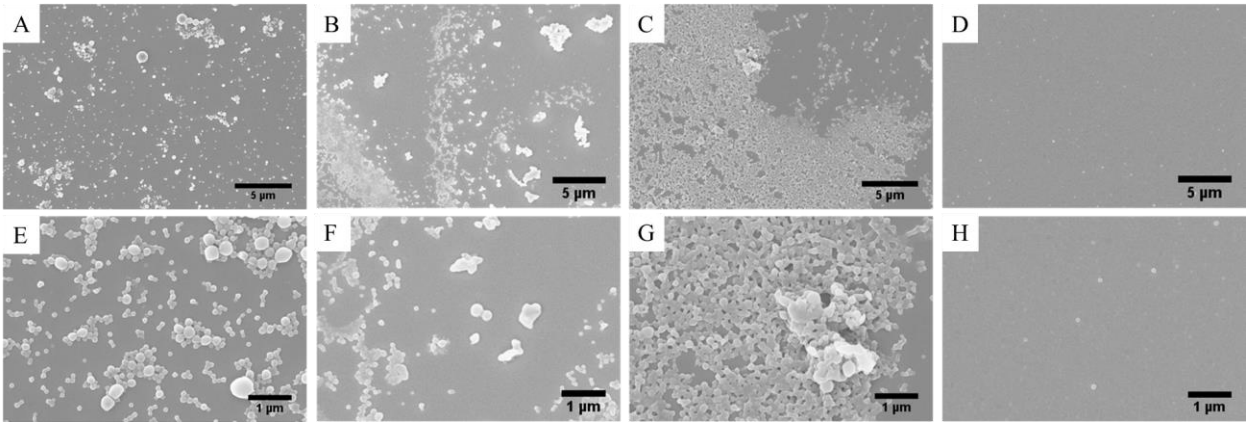

Figure 6.4. SEM images of Baseline (A, E) and Samples 16 (B, F), 21 (C, G), and 23 (D, H).

6.4.4. Confirmation of Loading Increase using RhB

Based on the loading maximization, a confirmation study of the results was conducted using four modifications, explained in detail in

Table 6.2 along with corresponding drug loading and encapsulation efficiencies. The baseline sample remained the same as in the maximization study as a control, then remaining samples included decreased PVA combined with refrigerated wash cycles, using Spin-X concentrator tubes with 6 hours of dialysis, and finally 6 hours of dialysis using centrifuge tubes used for the Baseline, conical bottom 50 mL centrifuge tubes. The final sample was used to determine whether the short dialysis time or the concentrator tubes were making the largest difference in drug loading increase. Additionally, Spin-X tubes used for the confirmation study had a MWCO of 100 kDa in order to promote removal of PVA.

Table 6.2. Loading Confirmation using RhB.

Sample	PVA	Dialysis Time	Wash Cycles	Drug Loading (%)	Encapsulation Efficiency (%)
Baseline	1%	24 hrs	Rm Temp, Falcon	0.22	0.40
Low PVA, Fridge wash	0.5%	24 hrs	4 °C, Falcon	0.18	0.92
Spin-X tubes, MWCO 100 kDa	1%	6 hrs	Rm Temp, Spin-X Tubes	0.48±0.09	7.05±1.54
6hr Dialysis, Reg wash	1%	6 hrs	Rm Temp, Falcon	0.31	0.63

Loading and encapsulation efficiency of αCT1 in particles was highest when using the concentrator tubes, at 0.48% loading, which is more than double the loading of the baseline method (0.22%), and encapsulation efficiency was 7%. Using regular centrifuge tubes and 6 hours of dialysis showed the next highest loading, of 0.31% with an encapsulation efficiency of 0.63%. Using a lower amount of PVA did not increase drug loading, but did increase encapsulation efficiency slightly, to 0.92% compared with 0.4% for the Baseline method.

When using 6 hours of dialysis and regular centrifuge tubes, drug loading is increased, thus part of the drug loading increase observed from using Spin-X tubes is due to the decrease in dialysis time. However, because encapsulation efficiency of the Spin-X tube sample is much higher than when they were not used, the concentrator tubes must be able to capture more particles than regular centrifuge tubes, thus increasing the encapsulation efficiency. However, if this were the only cause of difference between with and without use of the Spin-X tubes, then the drug loading would be expected to be the same as with sample prepared without using Spin-X tubes but same dialysis time. The likely cause of increase to the drug loading with the Spin-X tubes then is likely due to a decreased efficiency to remove drug adsorbed to the outside of the particles. When using concentrator tubes, not as much of the "supernatant" is removed compared with regular centrifuge tubes, and so the drive for adsorbed drug to desorb and move into the surrounding liquid is decreased. This could cause the increased drug loading seen with Spin-X samples.

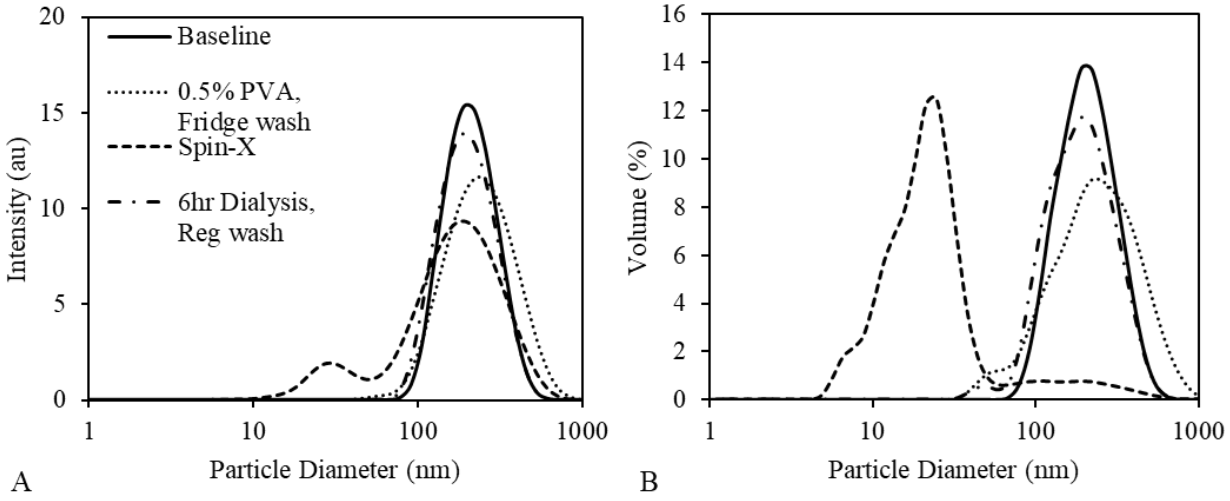

Figure 6.5. Particle size of RhB-PLGA-NPs confirmation samples using DLS by A) intensity and B) volume.

Table 6.3. Comparison of particle sizes via Z-averages of confirmation studies compared with similar samples from the maximization study.

Sample	Max. Study Z-Ave, (PDI)	Confirm. Study Z-ave, (PDI)
Baseline	193.3 ± 1.5 (0.17 ± 0.02)	196.9 ± 15.0 (0.11 ± 0.02)
Low PVA*, Fridge wash	170.6 ± 2.0 (0.14 ± 0.03)	217.7 ± 3.1 (0.21 ± 0.02)
Spin-X	65.0 ± 1.8 (1.16 ± 0.04)	119.7 ± 12.4 (0.44 ± 0.05)
6hr Dialysis, Reg wash	N/A	186.0 ± 2.5 (0.14 ± 0.01)

*Low PVA concentrations used here were 0.4% from the maximization study and 0.5% for the confirmation study.

Particle sizes of the samples were overall similar compared with the maximization study, as shown by the Z-averages of particle size in Table 6.3. The low PVA concentration samples increased in particle size. This could be due to the difference in concentrations used between the maximization study (0.4 w/v%) and the confirmation study (0.5 w/v%). The concentrator tube sample size also increased during the confirmation study. However, the MWCO of the tubes used was increased for the confirmation study from 10 kDa to 100 kDa. The higher MWCO may have allowed some of the smallest particles to be pulled through the membrane. However, in the DLS plots in Figure 6.5, it can be seen that the bi-modal peaks are still present with the Spin-X tubes

that were observed during the maximization study. Volume % peaks show that most of the particles are in the lower range, as in the maximization study.

Particle morphology of the confirmation study samples was similar to those observed in the maximization study, being smooth and mostly spherical in shape. Particles washed with Spin-X tubes appeared more clearly than with the maximization study, most likely because more PVA could be removed from the samples, preventing a heavy blanket of PVA from coating the sample. However, some coating of PVA appeared to be present in the sample, so not all of the excess PVA was removed with the increase of MWCO.

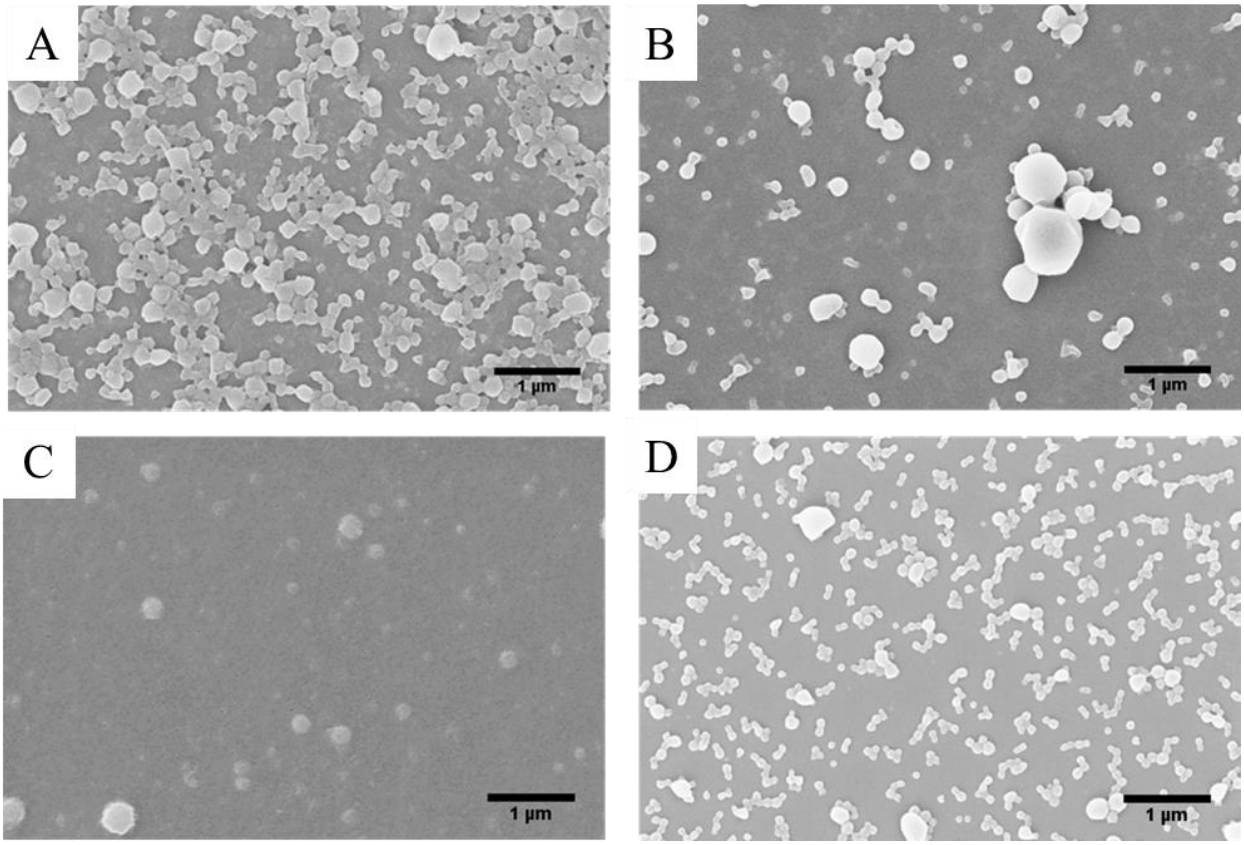

Figure 6.6. SEM images of RhB-PLGA-NPs confirmation study.

6.4.5. Loading Confirmation Study using αCT1

Results from the increase in drug loading using RhB were examined using αCT1 with the goals of 1) determining whether the method found to increase drug loading the most for RhB-PLGA-NPs also increased loading for aCT-PLGA-NPs and 2) determining whether the process used to make sterile nanoparticles changed the drug loading or release profile of the particles.

Sample descriptions can be found in Table 6.4. The baseline method was once again used as a control. Other samples included using Spin-X concentrator tubes (MWCO 100 kDa), checking the sterile process for loading and release changes (by using the Baseline method and filtering all solutions to 0.2 μm before use), and finally a negative control of unloaded PLGA particles.

Table 6.4. Design of Confirmation Study using αCT1.

Sample	**Dialysis Time**	**Wash Cycles**	**Other**
Positive Control 1 (Baseline method)	24 hrs	Falcon	--
Spin-X Concentrator Tubes ("New" method)	6 hrs	Spin-X Tubes	--
Sterile Process ("Sterile")	24 hrs	Falcon	All solutions filtered to 0.2 μm before particle synthesis
Negative Control ("PLGA Only")	24 hrs	Falcon	No αCT1

Figure 6.7 compares loading, encapsulation efficiency, and yield of particles visually and Table 6.5 provides values for the graphs shown in Figure 6.7. Drug loading of particles was increased from 0.05% to 0.9%, or an order of magnitude, by using the New method. This increase is greater than the increase seen using RhB, which was slightly more than doubled when using the New method. The Sterile method had a large variation in loading, however the loading was not lower than the Baseline method, so sterilizing the particles does not decrease the loading compared with the Baseline method, and may in fact increase loading slightly, but additional experimentation should be completed in order to confirm results. A source of error could include interactions between the solutions and the filter used to sterilize the solution. Interactions could include some slight dissolution of the filter with the solvent (especially with DMSO), or some binding of the polymers to the filter that is not understood. An additional source of error is that by removing materials greater than 0.2 μm, potential nucleation sites for particle formation are also being removed, which would change how particles form compared with non-filtered solutions.

Particle yield was highest for the Baseline method at 58% while the New method and Sterile method had particle yields of 20% and 17%, respectively. While the Baseline method had almost triple the yield of the New method, the drug loading for the New method is about ten times as high. For practical purposes, then, the New method still encapsulates more drug in a smaller amount of particles compared with the Baseline method, so the New method is more economically efficient than the Baseline method.

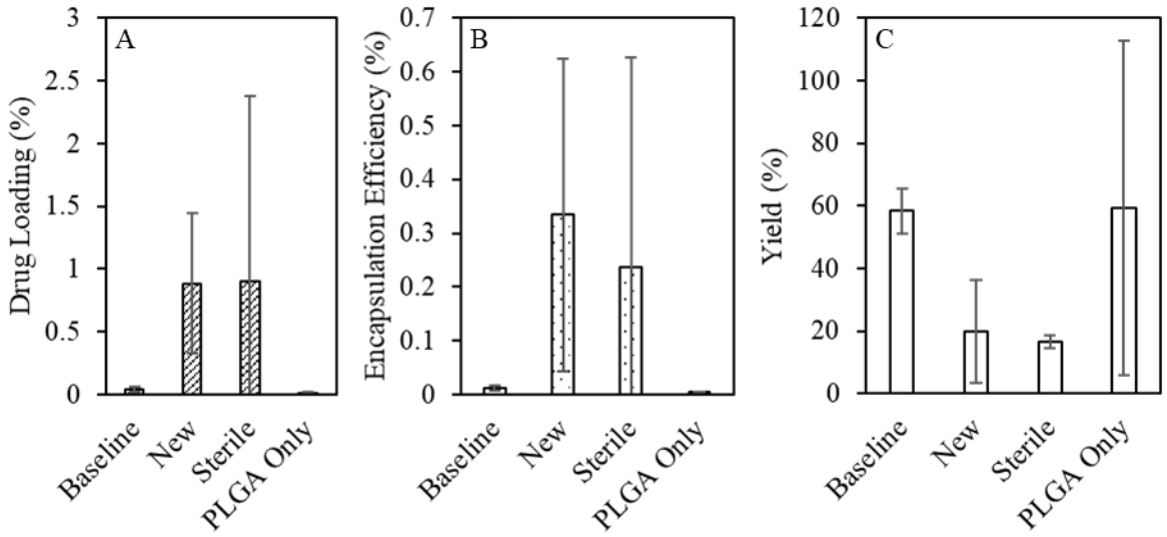

Figure 6.7. Loading, yield, and encapsulation efficiency of particles.

Table 6.5. Loading and encapsulation efficiency of confirmation study using αCT1-PLGA-NPs.

Sample	**Loading (%)**	**Encapsulation Efficiency (%)**	**Yield (%)**
Theoretical	10	100	100
Positive Control 1 ("Old" method)	0.05 ± 0.01	0.011 ± 0.005	58 ± 7
Spin-X Tubes ("New" method)	0.9 ± 0.6	0.33 ± 0.29	20 ± 16
Sterile Process ("Sterile")	0.9 ± 1.5	0.24 ± 0.39	17 ± 2
Negative Control ("PLGA Only" – no drug)	0.02 ± 0.01	0.004 ± 0.002	59 ± 53

All particle samples made using αCT1 showed a large amount of agglomeration when using the 2-jet mixer (Figure 6.8). Agglomerates are observed in the exit tubing before reaching the collection water. This is likely because αCT1 and PLGA are near the edge of solubility in the 10% water in DMSO solution, so particles readily precipitate in the mixer. Particles made using the New method appeared to be blanketed as previously observed, so most likely PVA remained in the solvent as in the RhB studies. The PLGA Only samples showed individual particles, similar to the RhB-PLGA-NPs.

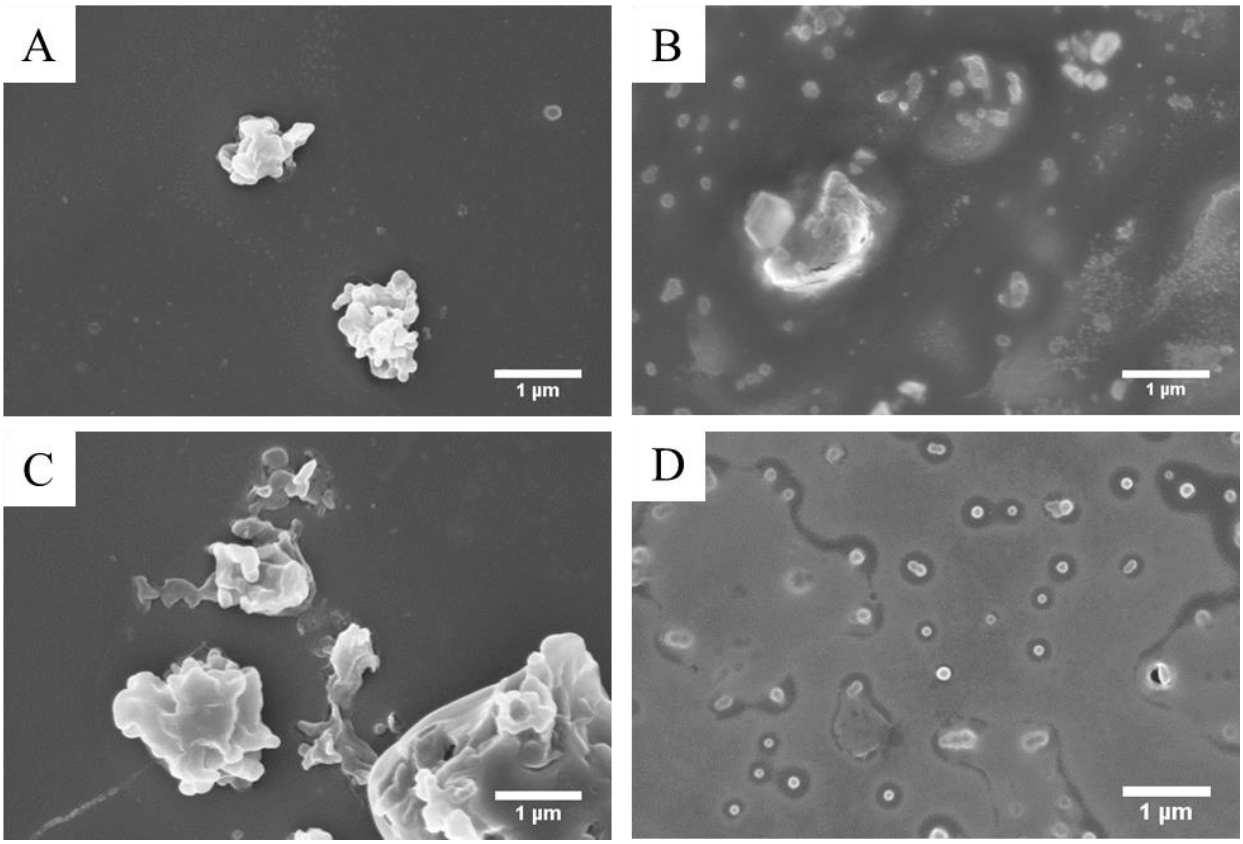

Figure 6.8. SEM of particles made from confirmation study.

6.4.6. Release of αCT1 from Confirmation Study Particles

Particles were allowed to release αCT1 for fourteen days in PBS at 37 °C. Baseline method surprisingly released almost all of the drug within 48 hours, which is different from the initial release study. It also appears that over six times the amount of drug encapsulated was released. The New method released about 11% of drug over two weeks and the sterile method release about 17% over two weeks, although the Sterile method could have released more or less based on the amount of variance in the loading. The New and Sterile methods released particles in a linear

manner after showing a burst release on the first day. It is expected that the remaining αCT1 would be released fully at 4-6 weeks as 50:50 PLGA degrades fully within about two months.

In future work involving *in vivo* studies, it is recommended that the New method be used based on the increase in loading and encapsulation efficiency. However, since particles also need to be sterile, it is recommended that additional experimentation is conducted to confirm and explore error in Sterile particle production. These experiments could begin by determining whether the concentration and molecular weight of solutions after filtration matches values before filtration.

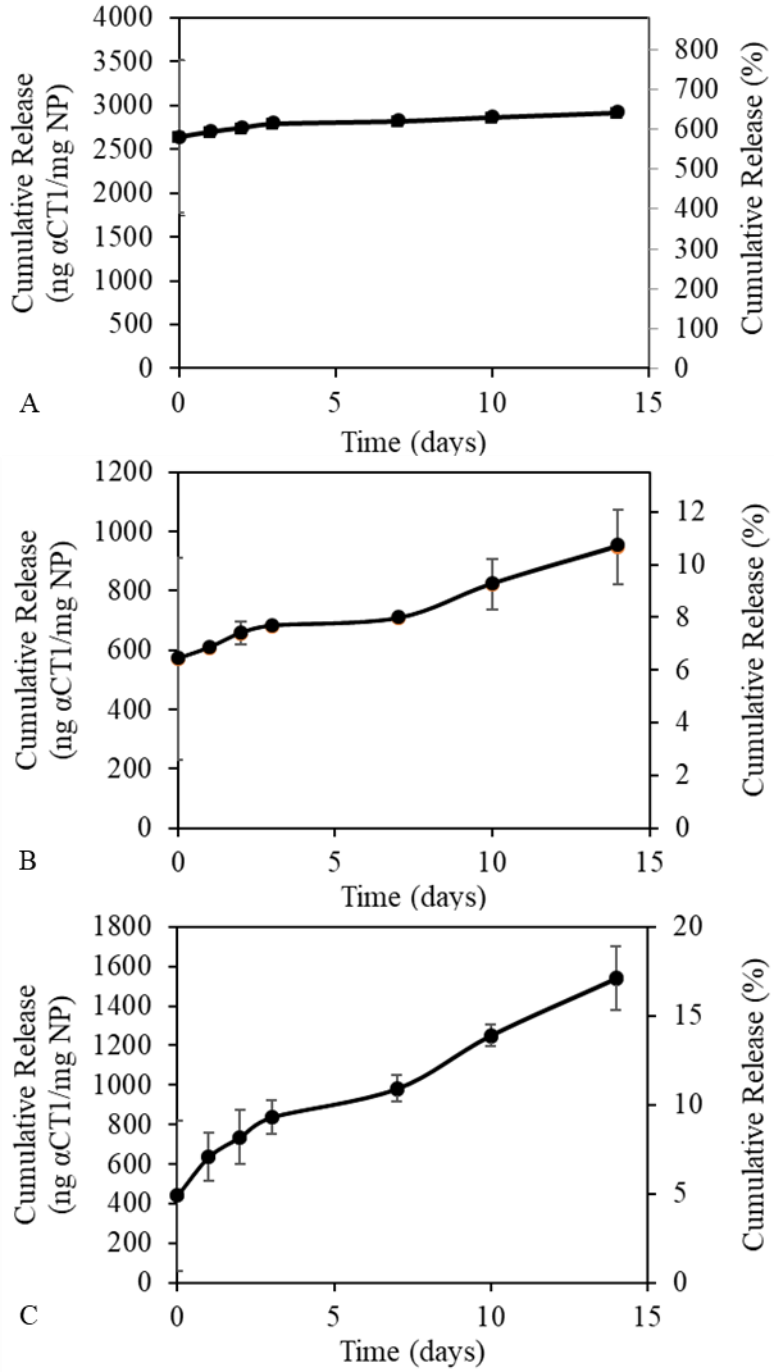

Figure 6.9. Release of αCT1 from PLGA-NPs during the confirmation study, including A) Baseline method, B) New method, and C) Sterile process.

6.4.7. Stability of αCT1 through drug release studies

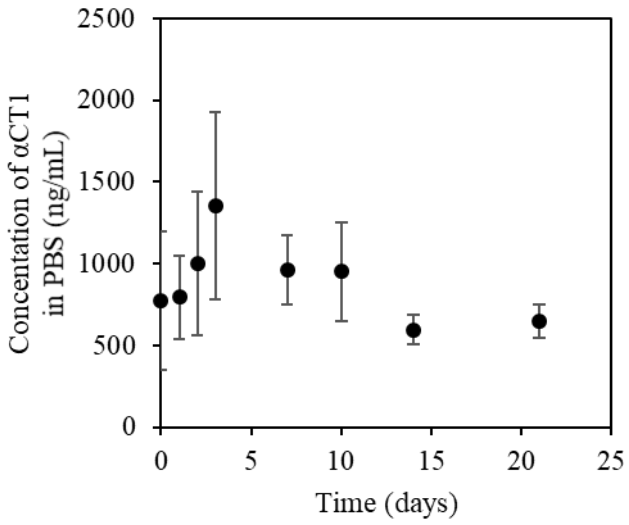

Figure 6.10. Stability of αCT1 during release studies.

In order to determine whether αCT1 was stable over the time course of the study, 1000 ng/mL of αCT1 in water was held at 37 °C for 21 days and cycled to room temperature at the same time points as the αCT1-PLGA-NPs. No definitive increase or decrease in αCT1 concentration was found. Thus, αCT1 does not significantly degrade over three weeks.

6.4.8. Drug Loading Differences between various αCT1-PLGA-NP Synthesis Methods

Particles were also synthesized using a 4-jet multi-inlet vortex mixer (MIVM) containing four inlets, in which one port was used for the solvent solution and the other three were used for the anti-solvent solution. Syringe pumps were used to input the solutions at the same time. Loading for the MIVM particles had loading even higher than when the 2-jet mixer was used, increasing loading to up to 6.7% and encapsulation efficiency up to 39% with 58% particle yield.

Table 6.6 compares the drug loading, encapsulation efficiency, and yield of particles between double emulsion method from the previous chapter, 2-jet mixer, and 4-jet mixer.

Table 6.6. Comparison of drug loading between different αCT1-PLGA-NP preparation methods. 2-jet mixer data replicated here for comparison and double emulsion method data taken from previous chapter.

Double Emulsion	**Drug Loading (%)**	**Encapsulation Efficiency (%)**	**Yield (%)**
Theoretical	1.4%	100%	100%
Filter 0.2 µm	0.1%	0.001%	~8%
Flash Nanoprecipitation			
Theoretical	10%	100%	100%
4-jet MIVM			
No filtering after washing, 0% PVA	6.70%	39.00%	58.30%
Filter 0.2 µm after washing, 1% PVA	5.80%	1.65%	2.80%
2-jet Mixer			
"Old" Method	0.05% ± 0.01%	0.011% ± 0.005%	58% ± 7%
"New" Method	0.9% ± 0.6%	0.33% ± 0.29%	20% ± 16%

Particles made using the MIVM also showed less agglomeration than using the 2-jet mixer, both visibly and under SEM (Figure 6.11). This is likely due to the increase in anti-solvent flowing through the mixer, forcing precipitates to be more separated during formation. However, due to the complex setup of the MIVM, it cannot be used in a sterile environment for synthesis of sterile particles for cell and animal studies, thus the 2-jet mixer was used for further cellular and animal studies.

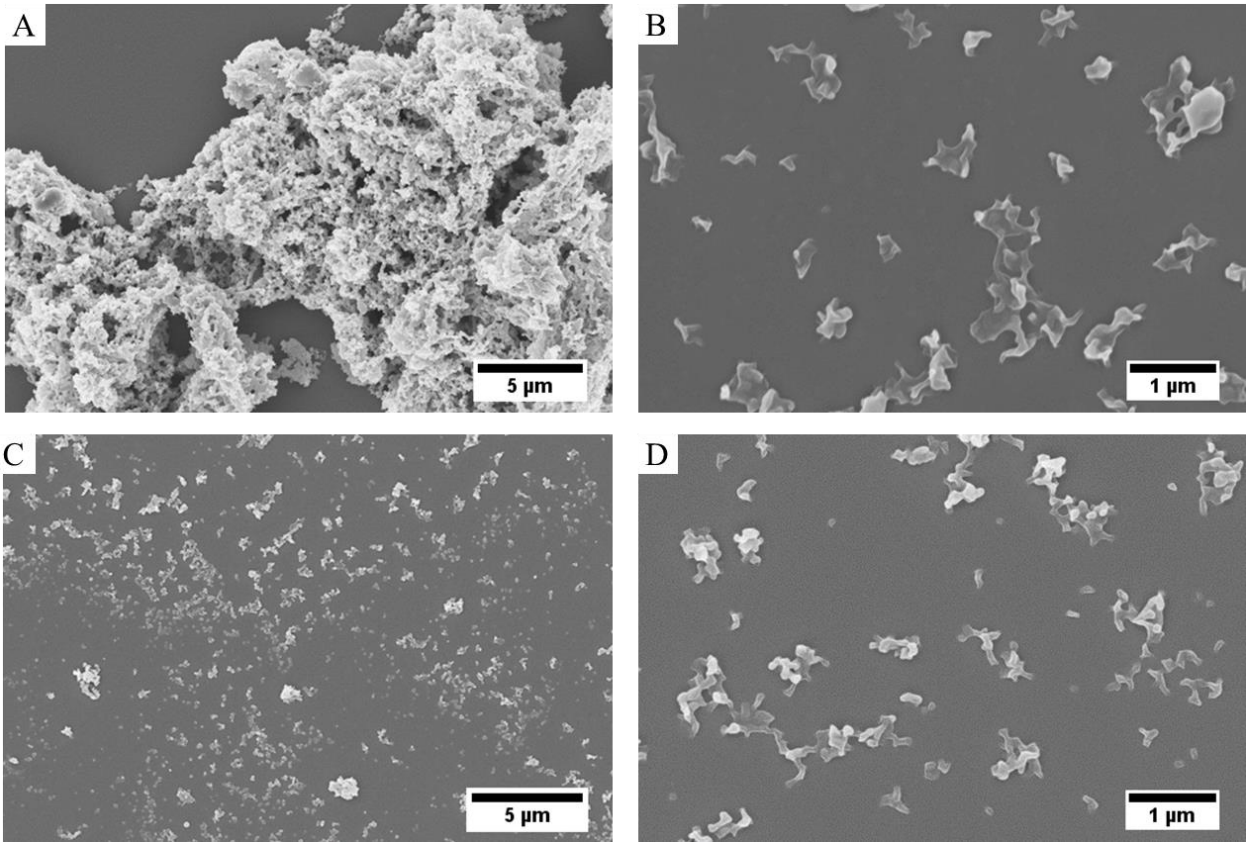

Figure 6.11. Comparison of αCT1-PLGA-NP morphology between A, B) 2-jet mixer and C, D) 4-jet mixer methods.

6.5. Conclusions

Nanoparticles containing αCT1 for controlled release were synthesized for glioblastoma applications. Drug loading of PLGA-NPs was maximized by exploring several aspects of the 2-jet mixer for the flash nanoprecipitation method. RhB was used as the model drug for increasing drug loading which was then confirmed using αCT1. Drug loading was increased by an order of magnitude in αCT1-PLGA-NPs. When a MIVM was used for particle synthesis, drug loading further increased to almost 7% drug loading and reduced agglomeration of particles. However, the complexity of the MIVM prevents its sterilization, thus the 2-jet mixer was used for further cellular and animal studies. In the future, creation of a less complex set up for the MIVM should be created to further increase loading for sterile nanoparticles.

References

1. Murphy, S. F.; Varghese, R. T.; Lamouille, S.; Guo, S.; Pridham, K. J.; Kanabur, P.; Osimani, A. M.; Sharma, S.; Jourdan, J.; Rodgers, C. M.; Simonds, G. R.; Gourdie, R. G.; Sheng, Z., Connexin 43 Inhibition Sensitizes Chemoresistant Glioblastoma Cells to Temozolomide. *Cancer Research* **2016,** *76* (1), 139-49.
2. Kanabur, P.; Guo, S.; Kelly, F.; Rodgers, C. M.; Simonds, G. R.; Gourdie, R. G.; Verbridge, S. S.; Sheng, Z., Patient-derived glioblastoma stem cells respond differentially to targeted therapies. *Oncotarget* **2016,** *7* (52), 86406-86419.
3. Grek, C. L.; Rhett, J. M.; Ghatnekar, G. S., Cardiac to cancer: connecting connexins to clinical opportunity. *FEBS Letters* **2014,** *588* (8), 1349-64.
4. Reisch, A.; Runser, A.; Arntz, Y.; Mely, Y.; Klymchenko, A. S., Charge-Controlled Nanoprecipitation as a Modular Approach to Ultrasmall Polymer Nanocarriers: Making Bright and Stable Nanoparticles. *ACS Nano* **2015,** *9* (5), 13.
5. Quintanar-Guerrero, D.; Allemann, E.; Doelker, E.; Fessi, H., A mechanistic study of the formation of polymer nanoparticles by the emulsification-diffusion technique. *Colloid and Polymer Science* **1997,** *275*, 640-647.
6. Pustulka, K. M.; Wohl, A. R.; Lee, H. S.; Michel, A. R.; Han, J.; Hoye, T. R.; McCormick, A. V.; Panyam, J.; Macosko, C. W., Flash nanoprecipitation: particle structure and stability. *Molecular Pharmacology* **2013,** *10* (11), 4367-77.
7. Bilati, U.; Allemann, E.; Doelker, E., Nanoprecipitation Versus Emulsion-based Techniques for the Encapsulation of Proteins Into Biodegradable Nanoparticles and Process-related Stability Issues. *AAPS PharmSciTech* **2005,** *6* (4), 11.
8. Govender, T.; Stolnik, S.; Garnett, M. C.; Illum, L.; Davis, S. S., PLGA nanoparticles prepared by nanoprecipitation: drug loading and release studies of a water soluble drug. *Journal of Controlled Release* **1999,** *57*, 171-185.
9. Bilati, U.; Allemann, E.; Doelker, E., Development of a nanoprecipitation method intended for the entrapment of hydrophilic drugs into nanoparticles. *European Journal of Pharmaceutical Science* **2005,** *24* (1), 67-75.
10. Zhu, Z., Flash nanoprecipitation: prediction and enhancement of particle stability via drug structure. *Molecular Pharmacology* **2014,** *11* (3), 776-86.
11. Budhian, A.; Siegel, S. J.; Winey, K. I., Haloperidol-loaded PLGA nanoparticles: systematic study of particle size and drug content. *International Journal of Pharmaceutics* **2007,** *336* (2), 367-75.
12. Miladi, K.; Sfar, S.; Fessi, H.; Elaissari, A., Nanoprecipitation Process: From Particle Preparation to In Vivo Applications. **2016**, 17-53.
13. Roberts, R.; Grek, C. L.; Ghatnekar, G. S.; Sheng, Z.; Gourdie, R. G.; Lamouille, S.; Foster, E. J., Development of PLGA nanoparticles for sustained release of a Connexin43 mimetic peptide to target glioblastoma cells. *Materials Science and Engineering: C* **2018 (submitted)**.
14. Dong, Y.; Feng, S. S., Methoxy poly(ethylene glycol)-poly(lactide) (MPEG-PLA) nanoparticles for controlled delivery of anticancer drugs. *Biomaterials* **2004,** *25* (14), 2843-9.
15. Chorny, M.; Fishbein, I.; Danenberg, H. D.; Golomb, G., Lipophilic drug loaded nanospheres prepared by nanoprecipitation: effect of formulation variables on size, drug recovery and release kinetics. *Journal of Controlled Release* **2002,** *83*, 389-400.
16. Bala, I.; Sarita Hariharan; Kumar, M. R., PLGA Nanoparticles in Drug Delivery: The State of the Art. *Critical Reviews™ in Therapeutic Drug Carrier Systems* **2004,** *21* (5), 387-422.

17. Miladi, K.; Sfar, S.; Fessi, H.; Elaissari, A., Nanoprecipitation Process: From Particle Preparation to In Vivo Applications. In *Polymer Nanoparticles for Nanomedicines*, 2016; pp 17-53.
18. Rawle, A., Basic Principles of Particle Size Analysis. Limited, M. I., Ed. Malvern Instruments: Vol. MRK034.

Chapter 7

Concluding Remarks

7.1. Conclusions

This dissertation describes efforts to develop methods of nanoparticle characterization that may be accessible to a broader audience, then use those techniques on synthesized nanoparticles that encapsulate a peptide for glioblastoma applications. CNCs were characterized with a variety of techniques and PLGA particles were synthesized in order to encapsulate the peptide drug αCT1. Specifically, goals presented in Chapter 1 were addressed as follows:

1. **Develop an electron microscopy sample preparation method**.

   Chapter 2 explored several methods to disperse and stain CNCs in order to avoid the use of a radioactive stain and a glow discharge device. A final protocol used bovine serum albumin in order to disperse particles during suspension droplet drying on a TEM sample grid and a vanadium-based commercial stain for increased contrast. Additionally, a dunk method during sample prep prevents application of too much stain or CNCs.

   This work will allow laboratories without the facilities to handle radioactive material or without the specialized equipment to be able to prepare TEM samples for characterization of CNCs. The ability to accurately characterize these nanoparticles will increase the reproducibility of any work involving CNCs.

2. **Develop a quantification method for monitoring concentration of CNCs in air**.

   In Chapter 3, aerosolized RhB-CNCs were collected using an impinger, which can be used in CNC production facilities. RhB-CNC concentrations were analyzed using UV-vis spectroscopy and scanning mobility particle sizer (SMPS). TEM and DLS were used for characterizing size and morphology changes. TEM sample preparation techniques from Chapter 2 were used for TEM sample prep in Chapter 3.

The methods developed here provide a first step for method development of aerosolized CNC concentration quantification. By using robust equipment and relatively simple protocol, these methods are more feasible for industry use. This will increase the ability to track CNC concentration in production facilities in order to ensure the safety of plant workers.

3. **Control the release of a peptide drug from PLGA nanoparticles**.

   In Chapter 4, the double emulsion-solvent evaporation method was used to encapsulate αCT1 and control its release over three weeks. Particle size was optimized for use in brain applications using BSA-PLGA-NPs and RhB-NPs were used for determining which emulsion method provided the highest drug loading. UV-vis techniques in Chapter 3 were used for Chapter 4. Cryoprotectant type and concentration was explored in order to reduce particle agglomeration upon freezing. Cellular studies showed αCT1 remaining in cells for at least four days, and cellular uptake was via endocytosis.

   While the drug loading in these particles was low, this work shows that αCT1 can be encapsulated in PLGA and remain in cells for at least four days. The extended release of drug over three weeks *in vitro* will facilitate long-term delivery for treatment of glioblastoma, which will be essential for the continual treatment of this type of brain cancer.

4. **Improve drug loading of αCT1 in PLGA nanoparticles**.

   Chapter 5 encapsulates αCT1 using flash nanoprecipitation to improve drug loading in the nanoparticles. After an initial improvement from Chapter 4, RhB-PLGA-NPs made using a 2-jet mixer were used to explore in depth various parameters that could affect drug loading in order to further increase loading. The parameters giving the highest loading in RhB-PLGA-NPs were tested using αCT1 and were confirmed to increase drug loading. A 4-jet mixer provides the highest loading overall, however the 4-jet mixer complex and cannot be moved for making sterile particles in a biosafety cabinet.

In this chapter, overall loading was increased by 1-2 orders of magnitude compared with the previous chapter. This increase in loading increases amount of αCT1 released from PLGA-NPs, which will likely improve efficacy in the body. In turn, improved efficacy of αCT1-PLGA-NPs will improve treatment of glioblastoma. Increased drug loading also increases the practicality of using these nanoparticles for drug delivery, and may lead to product realization.

Nanoparticles are becoming more prevalent in everyday products. In order to ensure quality and safety, characterization techniques must be in place that can be readily used by industry. Additionally, particle synthesis must be optimized as much as possible in order to maximize efficacy, such as for drug delivery applications. Characterization techniques can be used across different polymer types. Polymer synthesis technique can greatly influence the amount of drug loaded in particles.

7.2. Ongoing Research

This work presented in this dissertation is currently being continued in several projects. First, the protocol used to increase drug loading is being used for cell and animal studies in a Phase II grant in order to determine efficacy of the particles in glioblastoma treatment. This study involves validating the process for making sterile particles as well as production of a large number of particles for animal studies. Results of the study will advance the ability to treat glioblastoma and open additional studies to continue the project.

Another ongoing project seeks to combine CNCs with PLGA-NPs. Preliminary results show that CNCs may interact with PLGA during nanoparticle synthesis in a similar fashion as a surfactant. CNCs also seem to possibly moderate the particle size without covalent attachment. This could be due to steric or electrostatic hindrance interactions. Current studies are under way to determine the mechanism causing the observations.

7.3. Future work

While this work has contributed to the literature, there are more questions needing exploration. Concerning aerosolized CNCs, a more industrially relevant process needs to be defined that does not include requiring labeling of CNCs. SMPS, DLS, and TEM are methods that

do not require labeling. DLS requires a minimum concentration of particles in order to produce a histogram of particle sizes. This limitation can be used to the advantage of quantization by either concentrating or diluting the sample until the minimum concentration required for DLS is realized in the sample. X-ray diffraction (XRD) or TEM can then be used to confirm presence of CNCs.

In order to increase drug loading in PLGA-NPs, several routes can be explored. Ion pairing has been shown to increase drug loading by increasing solubility of drug in the polymer. A 2-step nanoprecipitation method has also been shown to improve drug loading by precipitating nanoparticles of drug into a polymer solution which is then precipitated. This would be nanoprecipitation's counterpart to double emulsion as compared with single emulsion. Either of these methods may also change the release profiles of αCT1 from the particles. This would in part be due to more drug being encapsulated deeper into the particle rather than being adsorbed to the surface or encapsulated near the surface of the particles.